DISSERTATION

FINITE ELEMENT ANALYSIS OF SKELETAL MUSCLE: A VALIDATED APPROACH TO MODELING MUSCLE FORCE AND INTRAMUSCULAR PRESSURE

Submitted by

Benjamin Brandt Wheatley

Department of Mechanical Engineering

In partial fulfillment of the requirements

For the Degree of Doctor of Philosophy

Colorado State University

Fort Collins, Colorado

Spring 2017

Doctoral Committee:

Advisor: Tammy L. Haut Donahue

Raymond C. Browning
Kenton R. Kaufman
Christian M. Puttlitz

ABSTRACT

FINITE ELEMENT ANALYSIS OF SKELETAL MUSCLE: A VALIDATED APPROACH TO MODELING MUSCLE FORCE AND INTRAMUSCULAR PRESSURE

Impaired muscle function can such as weakness is a reduction in muscle quality or quantity. Muscle weakness is debilitating conditions which can result from neuromuscular diseases and conditions such as multiple sclerosis, muscular dystrophy, stroke, injury, and aging. Impaired muscle function leads to disability, risk of injury, decreases in quality of life, and even death. Early disease detection, rehabilitation efforts, surgical techniques, and drug delivery can all be improved with the ability to identify muscle weakness by determining individual muscle force *in vivo*. Current clinical methods fail to measure individual muscle force as they are either inaccurate for individual muscle estimations (torque measurements) or are too invasive (buckle transducer insertion). Electromyography (EMG) is commonly used to diagnose improper muscle function, yet it is only a measurement of electrical activity. Thus, there is no minimally invasive clinical method which currently evaluates muscle force in vivo, which makes identifying and treating impaired muscle a challenge.

Pressure of interstitial fluid within muscle (i.e. Intramuscular Pressure, IMP) is the direct result of active muscle contraction or passive stretch. A low profile pressure microsensor can be used to measure IMP and thus evaluate force of individual muscles *in vivo*. Accurate microsensor use however, is reliant upon developing a relationship between IMP and force, which is currently incomplete. Specifically, while force and IMP are correlated, the variability of IMP *in* vivo

makes muscle force estimates from IMP measurements a challenge. Additionally, the distribution of IMP throughout muscle is variable and poorly understood. The goal of this work is to develop a computational model which can be used to better understand the behavior of intramuscular pressure. However, a lack of mechanical experimental analysis of skeletal muscle makes developing a robust model a challenge. Thus, two specific aims are proposed:

1) Experimentally investigate the passive properties of skeletal muscle and identify proper modeling assumptions to make in developing a constitutive approach.
2) Develop and implement a finite element approach for skeletal muscle which is capable of simulating muscle force and intramuscular pressure under passive stretch and active contraction conditions

Implementation of this model will provide insight into the potential causes of variability of intramuscular pressure measurements *in vivo* and future clinical approaches.

ACKNOWLEDGEMENTS

Over the course of this work, I have been lucky enough to gain invaluable training, insight, and lessons from my advisor Dr. Tammy Haut Donahue. Your wisdom and persistent belief in my ability to succeed have been vital to my growth as a researcher, educator, and person. You have built a supportive and diligent laboratory and because of that I can thank my lab mates for their encouragement and empathy during the long days and nights.

I would like to thank Dr. Kenton Kaufman and Dr. Gregory Odegard for their consistent investment in my work and professional development. Dr. Kaufman, you have taught me to not lose sight of clinical applications when I am deep in modeling. Muscle is, after all, constructed of fibers and cells, not nodes and elements. Dr. Odegard, you have showed me how continuum mechanics is as elegant as it is complex. I would like to acknowledge and thank our many collaborators at the Mayo Clinic and currently or formerly at the University of California, San Diego for gathering and sharing experimental data presented in Chapters 5, 6, and 7 and for their assistance throughout this process. I would also like to thank my committee members Dr. Ray Browning and Dr. Christian Puttlitz for their commitment to this project.

To my parents, my sister, my friends, mentors, colleagues, and collaborators who in some form or fashion had a hand in this adventure: I am forever thankful for your contributions.

This work was supported by the National Institutes of Health: National Institute of Child Health & Human Development [R01HD31476].

DEDICATION

To my wife Sarah, my partner in life and my best friend: your patience with this work and encouragement of my goals is truly amazing. My happiness and success begins and ends with your support.

TABLE OF CONTENTS

CHAPTER 1:

INTRODUCTION

1.1 Skeletal Muscle Anatomy and Physiology

Skeletal muscle is a soft tissue which comprises roughly 30% of body mass in females and 40% of body mass in males [1]. The primary role of skeletal muscle is to maintain posture and provide locomotion to the body. Skeletal muscle is unique as it has both a complex structure-function relationship as a passive material and exhibits contractile capabilities when voluntarily stimulated [2]. From the smallest repeating unit of the tissue – the force generating sarcomere – to whole muscle, the biological design and mechanical function allows skeletal muscle to grow, adapt, and perform its primary role: drive movement of the skeletal system.

1.1.1 Micro and Cellular Level

The signature quality of skeletal muscle, contractile force, is first generated by the sarcomere before eventually being transmitted through muscle to tendons, and finally the skeletal system. Thus, understanding active muscle function must first start at the sarcomere, which is between 1-4 μm in length [3]. The two primary constituents of the sarcomere are the myofilaments actin and myosin (Figure 1-1). The ability of skeletal muscle to generate force is traditionally attributed to these two proteins through the sliding filament theory (Figure 1-1B) [4,5]. In its natural state, myosin is bound to actin through cross bridges [2]. The addition of adenosine triphosphate (ATP) facilitates the unbinding and "charging" of myosin heads, moving from a low energy to a high energy state (Figure 1-1C). When the myosin head re-binds to the actin filament and pivots,

this shortens the overall length of the sarcomere. The action of one myosin head pivoting produces roughly 5 pN of force [6], while the maximum force from one sarcomere is roughly 150 mN [7]. The z disk separates sarcomeres in series, while the m line designates the middle of each sarcomere (Figure 1-1A). The final component of the sarcomere is the protein titin, which is largely responsible for the passive tension in elongated sarcomeres [8]. Titin, one of the largest molecules discovered at roughly 3 MDa, is a key contributor to passive muscle fiber stiffness and organization of the sarcomere [9], and recent studies have suggested it may play a role in force enhancement in eccentric (shortening) skeletal muscle contraction [10,11].

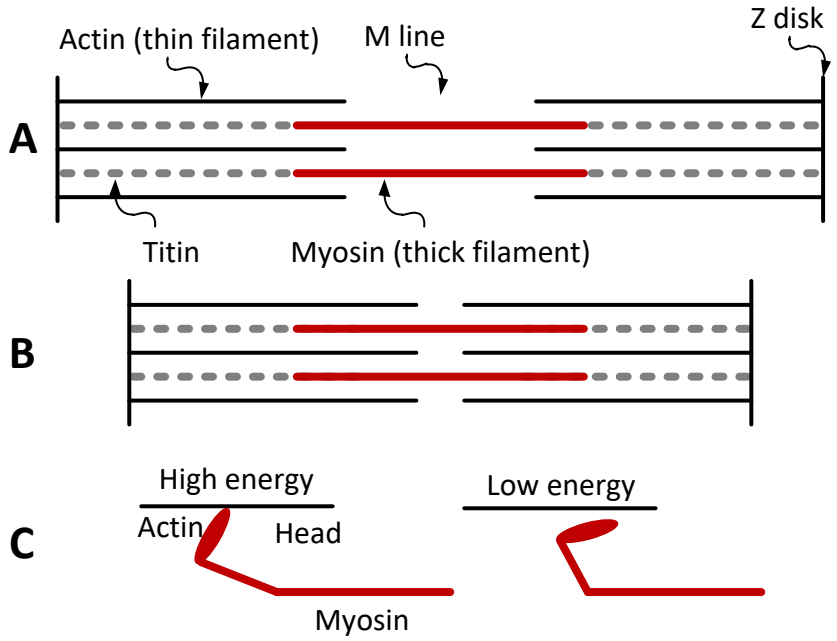

Figure 1-1. A) Schematic of the relaxed sarcomere, which is comprised of contractile myofilaments actin and myosin and the protein titin. The m line and z disk are architectural identifications of the sarcomere. B) Schematic of the contracted sarcomere, which is largely attributed to the interaction between actin and myosin. C) Schematic of the interaction between actin and myosin under high energy (left) and low energy (right) states.

The maximum isometric force (when the sarcomere is at a constant length while contracting) generated by a sarcomere is largely a function of the sarcomere length [2,3]. Additionally, titin is considered responsible for passive stiffness when the sarcomere is passive stretched [10,12,13].

Under isometric activation, the force-length relationship is thus broken into active and passive contributions (Figure 1-2). For the active contribution, this includes an ascending limb where actin overlap inhibits force production (Figure 1-2A), a plateau region where actin/myosin overlap is optimal (Figure 1-2B), and a descending limb where actin/myosin overlap decreases (Figure 1-2C). The sarcomere supports passive tension beginning at the plateau – also known as optimal length, which increases in nonlinear fashion as it is stretched.

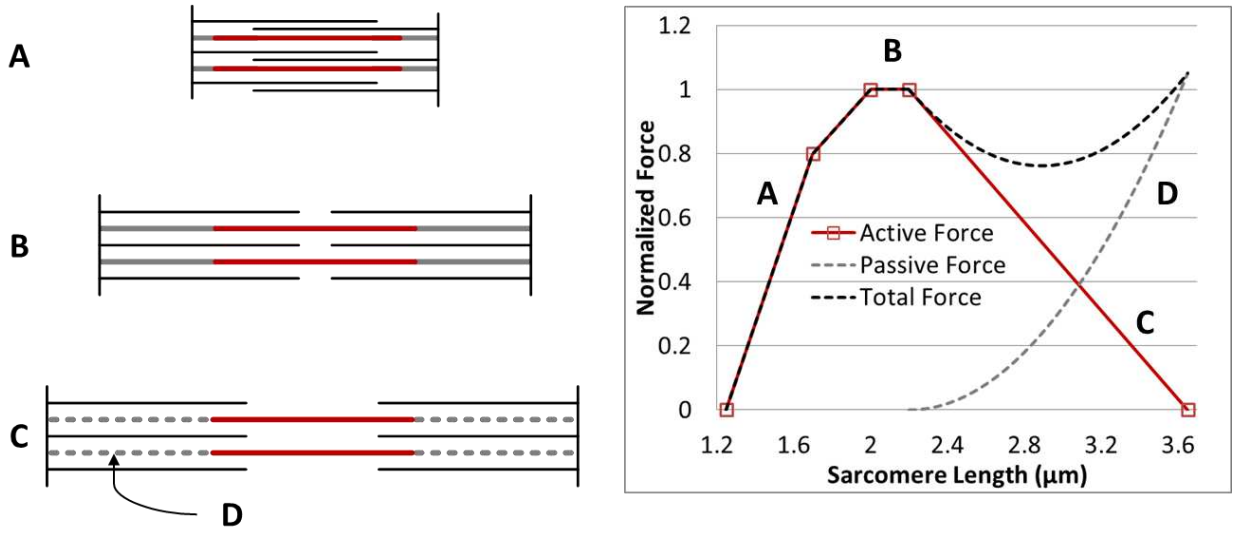

Figure 1-2. The force-length relationship of the sarcomere, beginning with active force for A) the ascending limb, where actin interference occurs, then B) the plateau or optimal length, where overlap between actin and myosin is maximized, and C) the descending limb, where actin-myosin overlap decreases. D) Passive tension is attributed to stretching of the protein titin.

Sarcomeres are organized in series and in parallel to form myofibrils, which are grouped in skeletal muscle cells (Figure 1-3A). Skeletal muscle cells, also known as muscle fibers, are long cylinder shaped structures, similar to other cells within the body in that they contain mitochondria, nuclei, fluid filled sarcoplasm, and a membrane (Figure 1-3A). The length and diameter of muscle fibers, however, are variable depending on the specific muscle task, as long fibers have high contraction velocities and produce a large range of motion, while fibers with a

larger diameter generate more force [2]. Surrounding the myofibrils is the transverse tubule system, which transmits contractile signals to the myofilaments. These signals originate as electrical potentials within the brain and spinal cord, travel to muscle through nerve cells known as motor neurons, and are transferred into chemical signals at the muscle fibers (Figure 1-3B). A motor unit is comprised of the motor neuron and the muscle fibers which it innervates.

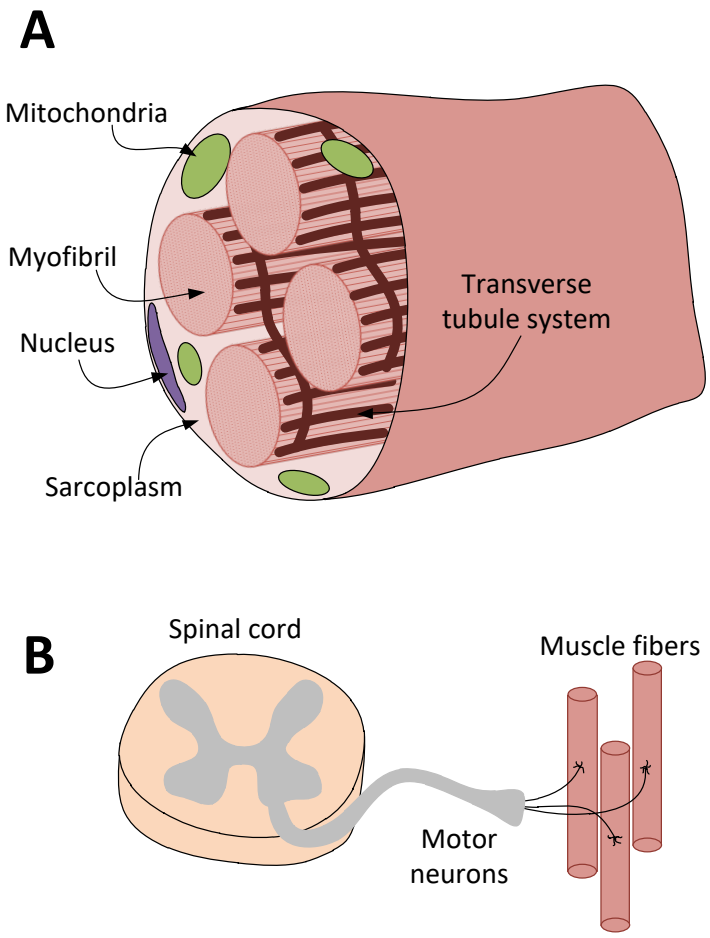

Figure 1-3. A) Muscle fibers or cells contain mitochondria and nuclei similar to other cells, along with contractile myofibrils and the transverse tubule system. B) A motor unit is comprised of a motor neuron or nerve cell and the muscle fibers it innervates.

When muscle fibers are stimulated through motor neurons with a single impulse, they generate a fiber twitch which occurs over 100 ms [2]. Increases in impulse frequency lead to summations of contraction waves, which when stimulated at high frequencies such as 100 Hz, fully fuse to

create a smooth force profile (Figure 1-4). The maximum contractile forces created by muscle fibers and motor units are highly variable, as they depend on fiber size, number of fibers, and the oxidation type of muscle fibers [2]. Fast muscle fibers generate more force and contract at a faster rate than slow muscle fibers, and each motor unit is comprised of fibers with similar fiber type. While physiologically there is a continuous distribution of fiber behavior ranging from "fastest" to "slowest", the creation of fiber types allows for general characterization of differences between fibers and muscles which have variations in physiology and function.

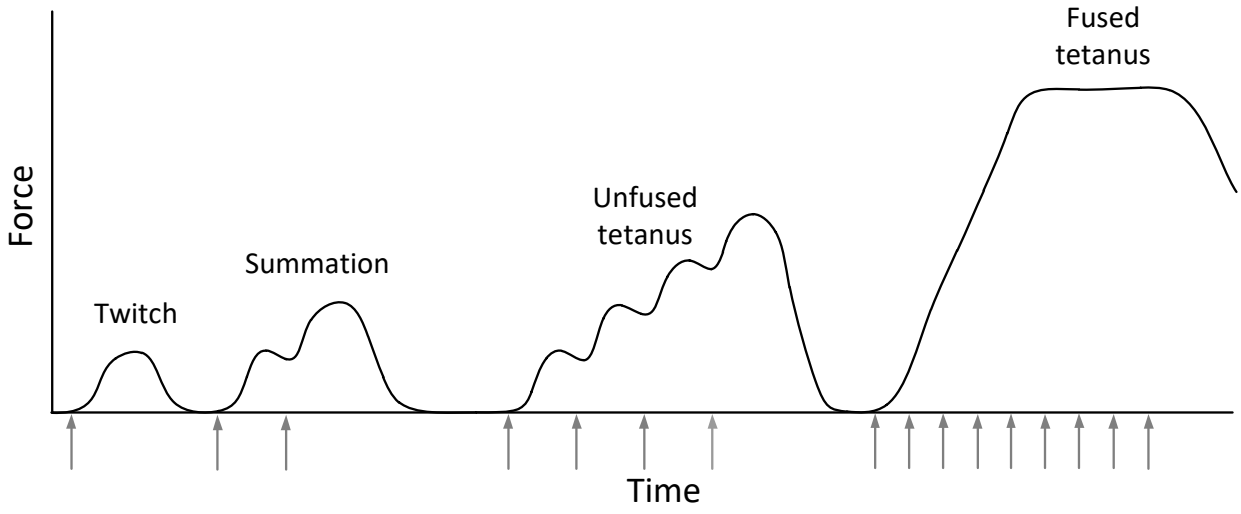

Figure 1-4. Representative graph of the force generated by a motor unit under various impulse frequencies. Gray arrows represent a single impulse at each time point.

The most common classification of muscle fibers and motor units is a division into three types: fast fatigable, fast fatigue resistant, and slow [14]. Variations in the function of these fibers are largely due to composition, including the type of myosin, the distribution of mitochondria, the size of the transverse tubule system, the size of the motor neurons, and the organization of the sarcomere [2,14,15]. In effect, fast fatigable fibers and motor units generate the highest amount of force but fatigue quickly, even within seconds. Fast fatigue resistant fibers generate less force

but are resistant to fatigue, and slow fibers generate the least amount of force but show very little fatigue even over multiple hours. These fatigue properties are largely due to the methods through which the fibers generate the molecule necessary for the actin-myosin complex to contract: adenosine triphosphate (ATP). Slow fibers use oxidative metabolism to create 32 ATP molecules per glucose molecule, while fast fatigable fibers use glycolysis to yield only two ATP molecules per glucose molecule [2]. Fast fatigue resistant fibers use both mechanisms. While oxidative metabolism is more efficient, oxygen is not readily available in large quantities, thus glycolysis can be used on stored glucose molecules. This phenomenon contributes to motor unit recruitment, where the small slow fibers are first recruited to prevent fatigue and excess use of stored glucose, then medium sized fast fatigue resistant, and finally large fast fatigable fibers, which is known as the Henneman size principle [16].

1.1.2 Tissue Level

Skeletal muscle is organized in a hierarchical structure by the extracellular matrix (ECM) [17]. The endomysium is the first layer of this matrix as it surrounds muscle fibers themselves (Figure 1-5A). The perimysium groups multiple fibers together into bundles or fascicles, and the epimysium surrounds whole muscle (Figure 1-5A). The ECM is largely comprised of collagen, including many different collagen types depending on the specific layer [18,19]. In total, skeletal muscle is comprised of roughly 80% intra and extracellular fluid by mass, with the remaining 20% being constituents such as extracellular matrix, contractile material, and solid cellular components [2,17,18,20]. Additionally, the extracellular matrix plays a key role in transmission of contractile force, as is connects muscle fibers in parallel, thus transmitting force laterally throughout the tissue (Figure 1-5B) [21]. Finally, much of the passive tensile stiffness of skeletal

muscle can be attributed to the ECM, in addition to stretching of titin at the sarcomere level [22]. Muscle is attached to the skeletal system through aponeurosis, which is a tendinous-like sheath where fibers terminate, and tendon.

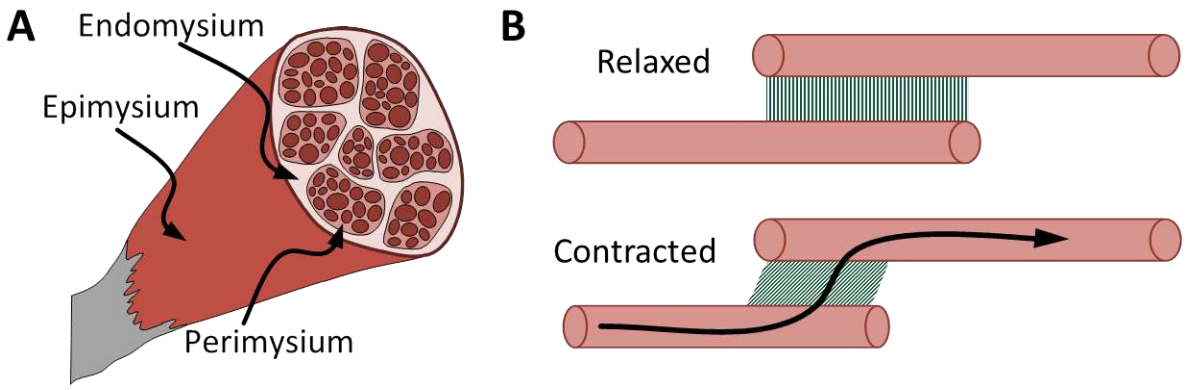

Figure 1-5. A) Muscle extracellular matrix provides a hierarchical structure starting with endomysium, which surrounds muscle fibers, then perimysium, which groups multiple fibers into a bundle or fascicle, and finally epimysium, which surrounds whole muscle. B) Schematic of transmission of contractile force (black arrow) in skeletal muscle, as the ECM connected muscle fibers laterally (top), such that when fibers contract the force is transmitted laterally through shearing of the ECM (bottom).

The isometric force-length relationship observed at the sarcomere level is similarly observed at the whole muscle level, and while muscle lengths range significantly *in vivo*, a general estimate of ± 20% of optimal length is usually appropriate (Figure 1-6A) [3]. Additionally, just as the sarcomere generates force as a function of length, muscle force also varies depending on contraction velocity. However, the difficulties in experimentally observing this phenomenon at the sarcomere level make it much easier to study at the fiber or tissue level [23,24]. Muscle contraction velocity is designated into two scenarios: muscle shortening or concentric activation, and muscle lengthening or eccentric activation. Under concentric activation, muscle force decreases in nonlinear fashion as contraction velocity increases (Figure 1-6B) [25]. Under eccentric activation, however, muscle force rapidly increases and plateaus as the rate of

lengthening increases (Figure 1-6B). Whole muscle specific tension (total force divided by area) is 25 N/cm^2 or 250 kPa for fast fibers, and 10 N/cm^2 or 100 kPa for slow fibers [2].

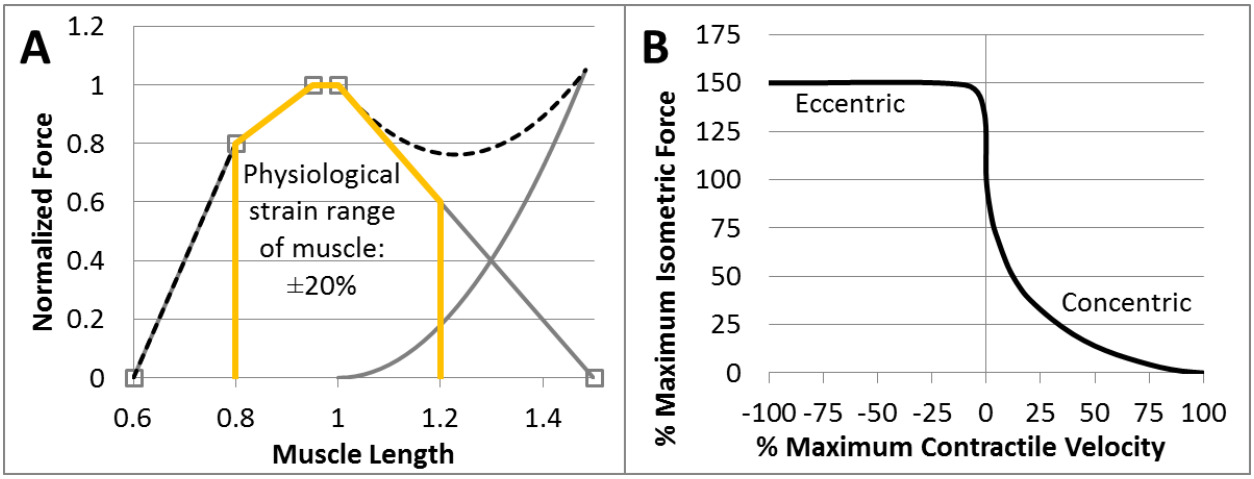

Figure 1-6. A) Isometric force-length relationship of whole muscle is similar to that of the sarcomere. A general estimate of muscle strain *in vivo* is ± 20% of optimal length, although this varies. B) Force-velocity relationship of whole muscle is divided into two conditions: concentric (shortening) and eccentric (lengthening) contractions.

Organization of muscle fibers *in vivo* also contributes to the function of force generation. Perhaps the two most important characteristics of whole muscle structure are fiber length and physiological cross sectional area (PCSA, Equation 1, where m is mass, θ_p is pennation angle, ρ is density, and L_f is fiber length). Muscles with longer fibers have a larger operating range, which provides more range of motion for the skeletal system, and have faster contraction velocities. Muscles with larger PCSA are able to generate more force due to increases in fiber area. Longer fiber lengths are the result of more sarcomeres in series, which contract at the same rate and change in length, while larger PCSA is the result of more sarcomeres in parallel, which all contract with the same force. Increases in PCSA are partially the result of fiber packing, or fiber pennation. The pennation angle θ_p is the angle between the force generation of muscle and

the orientation of muscle fibers (Figure 1-7A). Fiber packing through pennation allows for more fibers in series and thus greater force production (Figure 1-7B).

$$PCSA = \frac{m*cos\theta_p}{\rho*L_f} \quad (1)$$

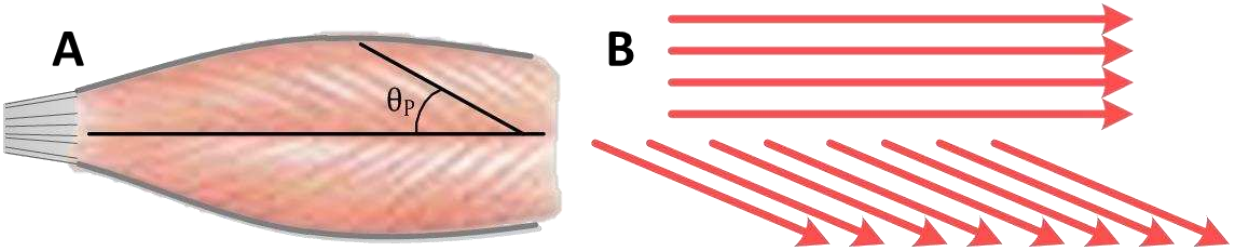

Figure 1-7. A) Skeletal muscle pennation angle θ_p is the angle between the direction of whole muscle and muscle fibers. B) In comparison to a pennation angle of zero (top), pennate fiber packing (bottom) allows for more fibers in parallel for the same volume, and thus more muscle force.

The structure and composition of skeletal muscle manifests in unique function as a passive constituent as well. Specifically, muscle exhibits transversely isotropic and nonlinear stiffness behavior under both tensile [26,27] and compressive [28,29] loading. However, there are conflicting studies in terms of tensile anisotropy, as some report the muscle fiber or longitudinal direction exhibits a stiffer response than the cross fiber or transverse orientation [30], while others report the opposite [26,27]. While it's unclear exactly why these studies are conflicting, the disparities may be the result of post mortem handling and rigor mortis effects [28,31,32], variations in muscle architecture across species, or differences in testing protocol.

Time dependent relaxation also occurs under both tension [33–35] and compression [36–38], and while this is largely attributed to inherent viscoelasticity of muscle, poroelasticity (fluid flow) may play a role as well [39]. Additionally, while passive tensile viscoelasticity at the muscle fiber level is nonlinear [35], this does not appear to be the case at the whole muscle level [34]. This complex passive behavior is the result of contributions from and interactions between

muscle fibers, the extracellular matrix, and the fluid content of skeletal muscle. While the extracellular matrix largely contributes to tensile stiffness as stated above [22], the complete structure-function relationship for skeletal muscle is still not clear. Thus, to better understand passive muscle function, the nonlinear viscoelastic behavior at the tissue level and the role of poroelasticity must be elucidated.

1.2 Impaired Skeletal Muscle Function

Muscle weakness is a major clinical concerns surrounding skeletal muscle function. Weakness can be the result of a wide range of clinical conditions, including neuromuscular diseases such as multiple sclerosis [40], and muscular dystrophy [41], sarcopenia [42], injury to orthopaedic tissue [43] and neurological tissue [44], and stroke [45]. Characterized as a decrease in the force generated by skeletal muscle, weakness can cause increased risk of injury or fall [46], is associated with osteoarthritis [47], and in the case of muscular dystrophy eventually causes death [41]. The causes for neuromuscular diseases include motor neuron degradation for multiple sclerosis and a breakdown of the force transmission within muscle through the dystrophin molecule for muscular dystrophy. Thus, there is a wide range of causes for impaired skeletal muscle function, and a long list of symptoms and increased risks for those with force impairment.

Muscle weakness result from and can lead to a number of physiological changes in skeletal muscle function [2]. For example, chronic disuse leads to decreases in muscle volume (and thus cross sectional area), increases in passive muscle stiffness through fibrosis, and a transition to predominantly fast twitch fiber types [48]. Sarcopenia leads to muscle weakness as a result of

decreases in muscle quality (specific tension or force per area) and muscle quantity [49,50]. Thus, diagnosing and treating skeletal muscle impairment requires a knowledge of both improper physiological function and structural or biological changes.

Current methods to evaluate skeletal muscle function *in vivo* include electromyography (EMG) buckle transducer insertion, and torque measurements. However, EMG is a measurement of electrical activity only [51–53], buckle transducer insertion is a highly invasive procedure [54,55], and torque measurements are from multiple muscles crossing a joint and thus do not directly measure individual muscle force [56–59]. Thus, there is no current clinical approach to directly evaluate individual muscle force. While the above approaches all provide valuable insight into skeletal muscle function and impairment *in vivo*, these drawbacks severely limit the clinical capabilities of surgeons, physicians, and physical therapists. An approach to directly identify individual muscle force would benefit diagnostic techniques for neuromuscular diseases, treatments of muscle weakness and spasticity, and targeted delivery for drug therapies.

1.3 Intramuscular Pressure

Intramuscular pressure (IMP) is the pressurization of saturating fluid within skeletal muscle which occurs as a result of active contraction or passive deformation [60–65]. The correlation between muscle force and IMP is evident under isometric contraction [64,66,67], and promising under dynamic contractions [68]. Early studies of intramuscular pressure identified a linear relationship between pressure and muscle contraction force under submaximal isometric conditions [69], which were followed by studies at maximum voluntary contraction [62], and

under dynamic conditions [70], which were possible through advancements in pressure measurement technique.

IMP measurements have traditionally been obtained through insertion of a either needles [56,71], wick catheters [66], or pressure transducers [62] which can be invasive, particularly for isotonic (lengthening or shortening) contractions. More recently, the implementation of a minimally invasive pressure microsensor has shown success at measuring IMP [64,68,72]. These fiber optic microsensors measure fluid pressure through fluctuations of a diaphragm, which alters a fiber optic signal (Figure 1-8). Recent sensor advancement has shed further light into proper microsensor use, specifically sensor housing and anchoring within the tissue play a key role in accuracy of IMP readings, particularly under dynamic conditions [73]. These new sensor advancements have thus improved the functionality of this minimally invasive IMP measurement approach.

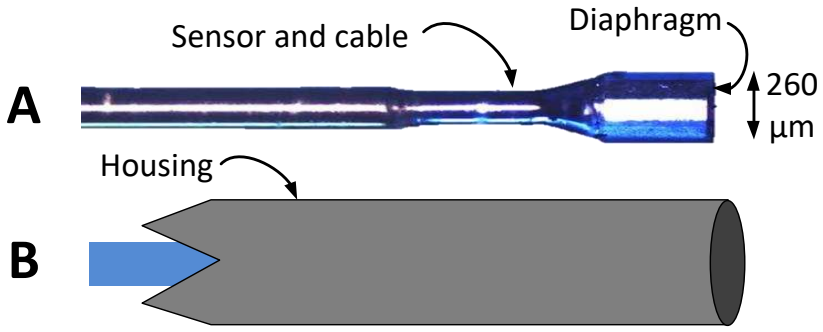

Figure 1-8. A) Pressure microsensor image, highlighting the sensor diaphragm which deforms due to environmental pressure, altering the fiber optic signal which is converted into pressure readings. B) Microsensor schematic with nitinol housing and anchoring barbs (left).

However, the correlation between muscle force and IMP is not currently strong enough for use of IMP as a clinical approach to estimate muscle force. This may be due to previous measurement techniques [73], variations in IMP spatially throughout the tissue [71], and difficulties with

patient to patient and muscle to muscle reproducibility [62,74]. Additionally, even some repeatability experiments have shown difficulties in developing a consistent relationship between muscle force and intramuscular pressure [75]. Intramuscular pressure is also a function of fatigue [76], and from an impairment standpoint it remains unclear how IMP varies with musculoskeletal diseases such as cerebral palsy, muscular dystrophy, and sarcopenia. In summary, there are major concerns in utilizing IMP measurements to predict skeletal muscle force, as the IMP distribution throughout skeletal muscle is currently unknown and there is little information on the force-IMP relationship in conditions other than healthy, rested skeletal muscle. Thus, there is a need to develop a tool which can accurately characterize both muscle force as well as intramuscular pressure, and provide both global and local insight into skeletal muscle function.

1.4 Finite Element Analysis of Skeletal Muscle

Finite element analysis is the use of discretization to solve complex geometrical problems with simplified approximate solutions (Figure 1-9). Finite element models have been developed simulating wide range of orthopaedic tissues, including bone [77,78], cartilage [79,80], meniscus [81,82], ligament and tendon [83], and intervertebral disk [84,85]. Additionally, finite element models incorporating multiple tissues have also been developed and implemented, such as those simulating the behavior of the human knee [86] and spine [87].

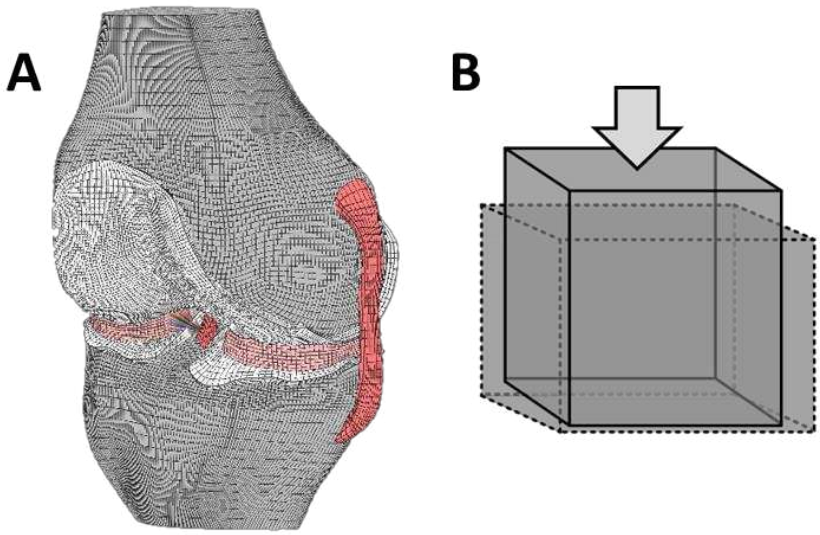

Figure 1-9. A) A finite element model of the human knee with a hexahedral mesh discretizes the complex geometry into elements. B) The solution for deformation of a hexahedron element is simpler than that of a more complex geometry.

Finite element modeling of skeletal muscle requires a unique approach due to the contractile nature of the tissue. Various finite element modeling studies have been conducted on skeletal muscle, with a wide range of assumptions. Early muscle finite element modeling incorporated muscle activation into a constitutive approach utilizing anisotropic hyperelasticity [88,89]. Blemker et al developed a three-dimensional idealized geometry of the biceps brachii which also included a hyperelastic and anisotropic formulation to study various geometrical assumptions [90]. Since then, similar models have been developed and implemented with improvements, including whole muscle geometry [91], studies of the role of fiber orientation [92,93], passive properties [94], simulations of shortening and lengthening muscle [95], and *in vivo* simulation [96]. Inhomogeneous assumptions have also been applied at various tissue scales, separating contractile and passive constituents of skeletal muscle [97–101].

While each of these approaches have provided valuable insight into muscle function or increased accuracy over previous methods, there still exists major advancements to be made in the muscle modeling field. Specifically, passive time dependent behavior of skeletal muscle is often neglected despite clear evidence of this behavior at the fiber [35], tissue [36], and whole muscle [34,102] level. There are limited finite element studies that treat skeletal muscle as viscoelastic [34], and despite the conflicting data on the tensile nonlinearity of muscle viscoelasticity, this has not been evaluated from a modeling perspective. Additionally, no finite element study of skeletal muscle had previously been developed incorporating poroelastic effects although they may contribute to muscle mechanics [39]. Finally, while some studies utilize a transversely isotropic, hyperleastic constitutive formulation which models muscle fibers as reinforcing constituents [88,101], some experimental studies have reported that muscle is actually stiffer in the cross fiber or transverse direction [26,27]. Thus, recommendations must be made in terms of proper modeling assumptions for skeletal muscle composition and function.

One of the earliest finite element studies of skeletal muscle was conducted to study the relationship between skeletal muscle force and intramuscular pressure [103]. While this approach was effective at modeling both passive and active muscle stress and intramuscular pressure, there were several drawbacks which inhibit broad use of this model. Firstly, time dependent properties were ignored, which severely limits the use of this model to study dynamic conditions. Additionally, the idealized geometry and lack of fluid content inherently limit the physiological accuracy, as intramuscular pressure is the pressurization of muscular interstitial fluid. Lastly, it remains to be seen if this approach is valid outside of the single condition which was modeled, the New Zealand White Rabbit tibialis anterior. Thus, while this model displayed efficacy of

finite element analysis in accurately characterizing both muscle force as well as intramuscular pressure, a more comprehensive approach is needed to achieve clinical impact.

1.5 Specific Aims

To improve clinical treatment of impaired skeletal muscle, the following specific aims have been identified to facilitate the development and employment of a computational tool which is capable of modeling both muscle force as well as intramuscular pressure. This tool can then be used to further study the relationship between muscle force and intramuscular pressure and potentially identify the cause of variability of intramuscular pressure measurements.

Specific Aim 1: Experimentally investigate the passive properties of skeletal muscle and identify proper modeling assumptions to make in developing a constitutive approach.

Sub Aim 1A: Evaluate the viscoelastic nonlinearity of skeletal muscle in tension. While the assumption of linear viscoelasticity is common in biological studies and has been applied to skeletal muscle at the whole tissue level, muscle fibers have shown nonlinear viscoelastic behavior. Thus, it remains unclear as to how skeletal muscle viscoelasticity should be modeled from a tensile standpoint. Experimental data of skeletal muscle under stress relaxation conditions will be completed and analyzed using various viscoelastic models to determine the appropriate assumptions for future models.

Sub Aim 1B: Elucidate the true tensile transverse isotropy of skeletal muscle.

Conflicting reports in literature of skeletal muscle transverse isotropy make proper modeling assumptions difficult to determine. Specifically, the question of whether or not the longitudinal or fiber direction is stiffer than the transverse or cross fiber direction must be answered. Experimental work is proposed to compare the transversely isotropic tensile behavior of skeletal muscle when tested under fresh conditions (pre-rigor) versus tissue subject to a freeze-thaw cycle. The findings will dictate the transversely isotropic constitutive approach for *in vivo* skeletal muscle.

Sub Aim 1C: Evaluate the hydraulic permeability of skeletal muscle.

The hydraulic permeability of skeletal muscle is unknown, despite the fact that it plays a major role in fluid pressurization (such as IMP) in biological tissues. Some biological tissues also utilize fluid content and retention to disperse loads under compression, which is largely dictated by the hydraulic permeability of the material. While this is not the primary role of skeletal muscle, fluid content of muscle may still contribute to compressive stiffness. Thus, there is a need to determine skeletal muscle permeability for implementation of physiologically accurate computational models and to better understand the distribution of loads within the tissue. In this study, direct permeation experiments will be performed along with simulations of experimental findings with various assumptions to determine how to properly model skeletal muscle permeability.

Specific Aim 2: Develop and implement a finite element approach for skeletal muscle which is capable of simulating muscle force and intramuscular pressure under passive stretch and active contraction conditions.

Sub Aim 2A: Develop a passive constitutive approach and validate against stretched skeletal muscle using finite element analysis.

Based on the findings from Specific Aim 1, a novel constitutive approach will be developed and implemented to simulate the passive stretch response for skeletal muscle. Specifically, this model will incorporate the tensile time dependent behavior determined in Aim 1B through viscoelasticity, nonlinear and transversely isotropic behavior from Aim 1B through transversely isotropic hyperelasticity, and the role of fluid flow and pressurization studied in Aim 1C through poroelasticity. The combination of these elastic theories will yield a transversely isotropic, hyper-visco-poroelastic constitutive approach. This constitutive model will be incorporated into a finite element geometry of the rabbit tibialis anterior for validation against experimental data of passively stretched muscle. The model will be validated against experimental data of both muscle stress as well as intramuscular pressure.

Sub Aim 2B: Develop an active constitutive and geometric approach and validate against contracting skeletal muscle using finite element analysis.

As a continuation of Specific Aim 2A, muscle activation will be simulated utilizing an addition of active stress to the constitutive model developed in Aim 2A. Additionally, inhomogeneity will be incorporated to account for muscle constituents which can (fibers) and cannot (fluid, ECM) generate contractile force. This approach will similarly be validated against experimental data of

rabbit muscle behavior under isometric maximally stimulated contractile conditions. This aim will also further investigate how passive model properties contribute to fluid pressurization. Based on experimental data and model output, clinical recommendations will be made about sensor insertion technique.

Sub Aim 2C: Implement the developed approach from 2A and 2B in a model of human skeletal muscle to strengthen validation and investigate variability of intramuscular pressure. Following model validation under passive stretch (Aim 2A) and maximal isometric contraction (Aim 2B) in a rabbit model, modeling of human muscle will be completed. Model agreement with human muscle data will greatly strengthen the confidence in employing this constitutive approach due to major differences in muscle architecture and scale. This model will also identify possible contributions to the variability in intramuscular pressure measurements *in vivo*. Modeling results can also provide insight into possible sensor insertion locations and help guide future experimental work to validate computational findings.

REFERENCES

[1] Janssen, I., Heymsfield, S. B., Wang, Z. M., and Ross, R., 2000, "Skeletal muscle mass and distribution in 468 men and women aged 18-88 yr.," J. Appl. Physiol., **89**(1), pp. 81–8.

[2] Lieber, R. L., 2010, Skeletal Muscle Structure, Function, and Plasticity, Lippincott Williams and Wilkins, Philadelphia, PA.

[3] Burkholder, T. J., and Lieber, R. L., 2001, "Sarcomere length operating range of vertebrate muscles during movement.," J. Exp. Biol., **204**(Pt 9), pp. 1529–36.

[4] Huxley, H., and Hanson, J., 1954, "Changes in the cross-striations of muscle during contraction and stretch and their structural interpretation.," Nature, **173**(4412), pp. 973–6.

[5] Huxley, H., and Niedergerke, R., 1954, "Structural changes in muscle during contraction; interference microscopy of living muscle fibres.," Nature, **173**(4412), pp. 971–3.

[6] Clemen, A. E.-M., Vilfan, M., Jaud, J., Zhang, J., Bärmann, M., and Rief, M., 2005, "Force-dependent stepping kinetics of myosin-V.," Biophys. J., **88**(6), pp. 4402–10.

[7] Wang, K., McCarter, R., Wright, J., Beverly, J., and Ramirez-Mitchell, R., 1993, "Viscoelasticity of the sarcomere matrix of skeletal muscles. The titin-myosin composite filament is a dual-stage molecular spring.," Biophys. J., **64**(4), pp. 1161–77.

[8] Magid, A., and Law, D. J., 1985, "Myofibrils bear most of the resting tension in frog skeletal muscle.," Science, **230**(4731), pp. 1280–2.

[9] Horowits, R., 1992, "Passive force generation and titin isoforms in mammalian skeletal muscle," Biophys. J., **61**(2), pp. 392–398.

[10] Tskhovrebova, L., and Trinick, J., 2002, "Role of titin in vertebrate striated muscle.," Philos. Trans. R. Soc. Lond. B. Biol. Sci., **357**(1418), pp. 199–206.

[11] Herzog, W., 2014, "The role of titin in eccentric muscle contraction.," J. Exp. Biol., **217**(Pt 16), pp. 2825–33.

[12] Anderson, J., Joumaa, V., Stevens, L., Neagoe, C., Li, Z., Mounier, Y., Linke, W. a, and Goubel, F., 2002, "Passive stiffness changes in soleus muscles from desmin knockout mice are not due to titin modifications.," Pflugers Arch., **444**(6), pp. 771–6.

[13] Gindre, J., Takaza, M., Moerman, K. M., and Simms, C. K., 2013, "A structural model of passive skeletal muscle shows two reinforcement processes in resisting deformation.," J. Mech. Behav. Biomed. Mater., **22**, pp. 84–94.

[14] Herbison, G. J., Jaweed, M. M., and Ditunno, J. F., 1982, "Muscle fiber types.," Arch. Phys. Med. Rehabil., **63**(5), pp. 227–30.

[15] Schiaffino, S., and Reggiani, C., 2011, "Fiber types in mammalian skeletal muscles.," Physiol. Rev., **91**(4), pp. 1447–531.

[16] Henneman, E., 1985, "The size-principle: a deterministic output emerges from a set of probabilistic connections.," J. Exp. Biol., **115**, pp. 105–12.

[17] Gillies, A. R., and Lieber, R. L., 2011, "Structure and function of the skeletal muscle extracellular matrix.," Muscle Nerve, **44**(3), pp. 318–31.

[18] Light, N., and Champion, A. E., 1984, "Characterization of muscle epimysium, perimysium and endomysium collagens.," Biochem. J., **219**(3), pp. 1017–1026.

[19] Passerieux, E., Rossignol, R., Chopard, A., Carnino, A., Marini, J. F., Letellier, T., and Delage, J. P., 2006, "Structural organization of the perimysium in bovine skeletal muscle: Junctional plates and associated intracellular subdomains," J. Struct. Biol., **154**(2), pp. 206–216.
[20] Sjøgaard, G., and Saltin, B., 1982, "Extra- and intracellular water spaces in muscles of man at rest and with dynamic exercise.," Am. J. Physiol., **243**(3), pp. R271-80.
[21] Huijing, P. A., 1999, "Muscle as a collagen fiber reinforced composite: A review of force transmission in muscle and whole limb," J. Biomech., **32**(4), pp. 329–345.
[22] Meyer, G. A., and Lieber, R. L., 2011, "Elucidation of extracellular matrix mechanics from muscle fibers and fiber bundles," J. Biomech., **44**(4), pp. 771–773.
[23] Harry, J. D., Ward, A. W., Heglund, N. C., Morgan, D. L., and McMahon, T. A., 1990, "Cross-bridge cycling theories cannot explain high-speed lengthening behavior in frog muscle," Biophys. J., **57**(2), pp. 201–208.
[24] Morgan, D. L., 1990, "New insights into the behavior of muscle during active lengthening," Biophys. J., **57**(2), pp. 209–221.
[25] Hill, A. V., 1938, "The Heat of Shortening and the Dynamic Constants of Muscle," Proc. R. Soc. B Biol. Sci., **126**(843), pp. 136–195.
[26] Takaza, M., Moerman, K. M., Gindre, J., Lyons, G., and Simms, C. K., 2012, "The anisotropic mechanical behaviour of passive skeletal muscle tissue subjected to large tensile strain," J. Mech. Behav. Biomed. Mater., **17**, pp. 209–220.
[27] Mohammadkhah, M., Murphy, P., and Simms, C. K., 2016, "The in vitro passive elastic response of chicken pectoralis muscle to applied tensile and compressive deformation," J. Mech. Behav. Biomed. Mater., **62**, pp. 468–480.
[28] Van Loocke, M., Lyons, C. G., and Simms, C. K., 2006, "A validated model of passive muscle in compression," J. Biomech., **39**(16), pp. 2999–3009.
[29] Pietsch, R., Wheatley, B. B., Haut Donahue, T. L., Gilbrech, R., Prabhu, R., Liao, J., and Williams, L. N., 2014, "Anisotropic compressive properties of passive porcine muscle tissue.," J. Biomech. Eng., **136**(11), p. 111003.
[30] Morrow, D. A., Haut Donahue, T. L., Odegard, G. M., and Kaufman, K. R., 2010, "Transversely isotropic tensile material properties of skeletal muscle tissue," J. Mech. Behav. Biomed. Mater., **3**(1), pp. 124–129.
[31] Van Ee, C. A., Chasse, A. L., and Myers, B. S., 2000, "Quantifying skeletal muscle properties in cadaveric test specimens: effects of mechanical loading, postmortem time, and freezer storage.," J. Biomech. Eng., **122**(1), pp. 9–14.
[32] Böl, M., Leichsenring, K., Ernst, M., and Ehret, A. E., 2016, "Long-term mechanical behaviour of skeletal muscle tissue in semi-confined compression experiments," J. Mech. Behav. Biomed. Mater., **63**, pp. 115–124.
[33] Rehorn, M. R., Schroer, A. K., and Blemker, S. S., 2014, "The passive properties of muscle fibers are velocity dependent," J. Biomech., **47**(3), pp. 687–693.
[34] Gras, L. L., Mitton, D., Viot, P., and Laporte, S., 2013, "Viscoelastic properties of the human sternocleidomastoideus muscle of aged women in relaxation," J. Mech. Behav. Biomed. Mater., **27**, pp. 77–83.
[35] Meyer, G. A., McCulloch, A. D., and Lieber, R. L., 2011, "A Nonlinear Model of Passive Muscle Viscosity," J. Biomech. Eng., **133**(9), p. 91007.
[36] Wheatley, B. B., Pietsch, R. B., Haut Donahue, T. L., and Williams, L. N., 2016, "Fully non-linear hyper-viscoelastic modeling of skeletal muscle in compression.," Comput.

Methods Biomech. Biomed. Engin., **19**(11), pp. 1181–9.
[37] Van Loocke, M., Lyons, C. G., and Simms, C. K., 2008, "Viscoelastic properties of passive skeletal muscle in compression: Stress-relaxation behaviour and constitutive modelling," J. Biomech., **41**(7), pp. 1555–1566.
[38] Van Loocke, M., Simms, C. K., and Lyons, C. G., 2009, "Viscoelastic properties of passive skeletal muscle in compression-Cyclic behaviour," J. Biomech., **42**(8), pp. 1038–1048.
[39] Yang, M., and Taber, L. A., 1991, "The possible role of poroelasticity in the apparent viscoelastic behavior of passive cardiac muscle.," J. Biomech., **24**(7), pp. 587–97.
[40] White, L. J., and Dressendorfer, R. H., 2004, "Exercise and Multiple Sclerosis," Sport. Med., **34**(15), pp. 1077–1100.
[41] Emery, A. E. H., 2002, "The muscular dystrophies.," Lancet, **359**(9307), pp. 687–695.
[42] Baumgartner, R. N., Koehler, K. M., Gallagher, D., Romero, L., Heymsfield, S. B., Ross, R. R., Garry, P. J., and Lindeman, R. D., 1998, "Epidemiology of Sarcopenia among the Elderly in New Mexico," Am. J. Epidemiol., **147**(8), pp. 755–763.
[43] Nicholas, J. A., Strizak, A. M., and Veras, G., 1976, "A study of thigh muscle weakness in different pathological states of the lower extremity.," Am. J. Sports Med., **4**(6), pp. 241–8.
[44] Thomas, C. K., Zaidner, E. Y., Calancie, B., Broton, J. G., and Bigland-Ritchie, B. R., 1997, "Muscle Weakness, Paralysis, and Atrophy after Human Cervical Spinal Cord Injury," Exp. Neurol., **148**(2), pp. 414–423.
[45] Bohannon, R. W., 2007, "Muscle strength and muscle training after stroke," J. Rehabil. Med., **39**(1), pp. 14–20.
[46] Moreland, J. D., Richardson, J. A., Goldsmith, C. H., and Clase, C. M., 2004, "Muscle Weakness and Falls in Older Adults: A Systematic Review and Meta-Analysis," J. Am. Geriatr. Soc., **52**(7), pp. 1121–1129.
[47] Loureiro, A., Mills, P. M., and Barrett, R. S., 2013, "Muscle weakness in hip osteoarthritis: A systematic review.," Arthritis Care Res. (Hoboken)., **65**(3), pp. 340–52.
[48] Wisdom, K. M., Delp, S. L., and Kuhl, E., 2014, "Use it or lose it: multiscale skeletal muscle adaptation to mechanical stimuli.," Biomech. Model. Mechanobiol.
[49] Pistilli, E. E., Alway, S. E., Hollander, J. M., and Wimsatt, J. H., 2014, "Aging alters contractile properties and fiber morphology in pigeon skeletal muscle.," J. Comp. Physiol. B.
[50] Morley, J. E., Abbatecola, A. M., Argiles, J. M., Baracos, V., Bauer, J., Bhasin, S., Cederholm, T., Stewart Coats, A. J., Cummings, S. R., Evans, W. J., Fearon, K., Ferrucci, L., Fielding, R. A., Guralnik, J. M., Harris, T. B., Inui, A., Kalantar-Zadeh, K., Kirwan, B. A., Mantovani, G., Muscaritoli, M., Newman, A. B., Rossi-Fanelli, F., Rosano, G. M. C., Roubenoff, R., Schambelan, M., Sokol, G. H., Storer, T. W., Vellas, B., von Haehling, S., Yeh, S. S., and Anker, S. D., 2011, "Sarcopenia With Limited Mobility: An International Consensus," J. Am. Med. Dir. Assoc., **12**(6), pp. 403–409.
[51] Drost, G., Stegeman, D. F., van Engelen, B. G. M., and Zwarts, M. J., 2006, "Clinical applications of high-density surface EMG: A systematic review," J. Electromyogr. Kinesiol., **16**(6), pp. 586–602.
[52] Perry, J., and Bekey, G. A., 1981, "EMG-force relationships in skeletal muscle.," Crit. Rev. Biomed. Eng., **7**(1), pp. 1–22.
[53] Farkas, C., Hamilton-Wright, A., Parsaei, H., and Stashuk, D. W., 2010, "A review of clinical quantitative electromyography.," Crit. Rev. Biomed. Eng., **38**(5), pp. 467–85.

[54] Lewis, J. L., Lew, W. D., and Schmidt, J., 1982, “A note on the application and evaluation of the buckle transducer for the knee ligament force measurement.,” J. Biomech. Eng., **104**(2), pp. 125–8.
[55] Hahs, D. W., and Stiles, R. N., 1989, “Buckle muscle tension transducer: What does it measure?,” J. Biomech., **22**(2), pp. 165–166.
[56] Sadamoto, T., Bonde-Petersen, F., and Suzuki, Y., 1983, “Skeletal muscle tension, flow, pressure, and EMG during sustained isometric contractions in humans.,” Eur. J. Appl. Physiol. Occup. Physiol., **51**(3), pp. 395–408.
[57] Borges, O., 1989, “Isometric and isokinetic knee extension and flexion torque in men and women aged 20-70.,” Scand. J. Rehabil. Med., **21**(1), pp. 45–53.
[58] Herbert, R. D., and Gandevia, S. C., 1995, “Changes in pennation with joint angle and muscle torque: in vivo measurements in human brachialis muscle.,” J. Physiol., **484**(2), pp. 523–532.
[59] Pandy, M. G., and Andriacchi, T. P., 2010, Muscle and joint function in human locomotion.
[60] Hargens, A. R., Akeson, W. H., Mubarak, S. J., Owen, C. A., Gershuni, D. H., Garfin, S. R., Lieber, R. L., Danzig, L. A., Botte, M. J., and Gelberman, R. H., 1989, “Kappa Delta Award paper. Tissue fluid pressures: from basic research tools to clinical applications.,” J. Orthop. Res., **7**(6), pp. 902–9.
[61] Mubarak, S. J., Hargens, A. R., Owen, C. A., Garetto, L. P., and Akeson, W. H., 1976, “The wick catheter technique for measurement of intramuscular pressure. A new research and clinical tool.,” J. Bone Joint Surg. Am., **58**(7), pp. 1016–20.
[62] Sejersted, O. M., Hargens, A. R., Kardel, K. R., Blom, P., Jensen, O., and Hermansen, L., 1984, “Intramuscular fluid pressure during isometric contraction of human skeletal muscle.,” J. Appl. Physiol., **56**(2), pp. 287–95.
[63] Parker, P. A., Körner, L., and Kadefors, R., 1984, “Estimation of muscle force from intramuscular total pressure,” Med. Biol. Eng. Comput., **22**(5), pp. 453–457.
[64] Davis, J., Kaufman, K. R., and Lieber, R. L., 2003, “Correlation between active and passive isometric force and intramuscular pressure in the isolated rabbit tibialis anterior muscle,” J. Biomech., **36**(4), pp. 505–512.
[65] Guyton, A. C., Granger, H. J., and Taylor, A. E., 1971, “Interstitial fluid pressure.,” Physiol. Rev., **51**(3), pp. 527–563.
[66] Körner, L., Parker, P., Almström, C., Andersson, G. B., Herberts, P., Kadefors, R., Palmerud, G., and Zetterberg, C., 1984, “Relation of intramuscular pressure to the force output and myoelectric signal of skeletal muscle.,” J. Orthop. Res., **2**(3), pp. 289–96.
[67] Winters, T. M., Sepulveda, G. S., Cottler, P. S., Kaufman, K. R., Lieber, R. L., and Ward, S. R., 2009, “Correlation between isometric force and intramuscular pressure in rabbit tibialis anterior muscle with an intact anterior compartment,” Muscle and Nerve, **40**(1), pp. 79–85.
[68] Ward, S. R., Davis, J., Kaufman, K. R., and Lieber, R. L., 2007, “Relationship between muscle stress and intramuscular pressure during dynamic muscle contractions,” Muscle and Nerve, **36**(3), pp. 313–319.
[69] Mazzella, H., 1954, “On the pressure developed by the contraction of striated muscle and its influence on muscular circulation.,” Arch. Int. Physiol. Biochim., **62**(3), pp. 334–47.
[70] Aratow, M., Ballard, R. E., Crenshaw, A. G., Styf, J., Watenpaugh, D. E., Kahan, N. J., and Hargens, A. R., 1993, “Intramuscular pressure and electromyography as indexes of

force during isokinetic exercise," J Appl Physiol, **74**(6), pp. 2634–2640.
[71] Nakhostine, M., Styf, J. R., van Leuven, S., Hargens, A. R., and Gershuni, D. H., 1993, "Intramuscular pressure varies with depth. The tibialis anterior muscle studied in 12 volunteers.," Acta Orthop. Scand., **64**(3), pp. 377–81.
[72] Kaufman, K. R., Wavering, T., Morrow, D., Davis, J., and Lieber, R. L., 2003, "Performance characteristics of a pressure microsensor," J. Biomech., **36**(2), pp. 283–287.
[73] Go, S. A., Jensen, E. R., O'Connor, S. M., Evertz, L. Q., Morrow, D. A., Ward, S. R., Lieber, R. L., and Kaufman, K. R., 2017, "Design Considerations of a Fiber Optic Pressure Sensor Protective Housing for Intramuscular Pressure Measurements," Ann. Biomed. Eng., **45**(3), pp. 739–746.
[74] Sejersted, O. M., and Hargens, A. R., 1995, "Intramuscular pressures for monitoring different tasks and muscle conditions.," Adv. Exp. Med. Biol., **384**, pp. 339–350.
[75] Saltin, B., Sjøgaard, G., Gaffney, F. A., and Rowell, L. B., 1981, "Potassium, lactate, and water fluxes in human quadriceps muscle during static contractions.," Circ. Res., **48**(6 Pt 2), pp. I18-24.
[76] Ameredes, B. T., and Provenzano, M. A., 1997, "Regional intramuscular pressure development and fatigue in the canine gastrocnemius muscle in situ.," J. Appl. Physiol., **83**(6), pp. 1867–76.
[77] Sandino, C., McErlain, D. D., Schipilow, J., and Boyd, S. K., 2015, "The poro-viscoelastic properties of trabecular bone: a micro computed tomography-based finite element study.," J. Mech. Behav. Biomed. Mater., **44**, pp. 1–9.
[78] Müller, R., and Rüegsegger, P., 1995, "Three-dimensional finite element modelling of non-invasively assessed trabecular bone structures," Med. Eng. Phys., **17**(2), pp. 126–133.
[79] Warner, M. D., Taylor, W. R., and Clift, S. E., 2001, "Finite element biphasic indentation of cartilage: A comparison of experimental indenter and physiological contact geometries," Proc. Inst. Mech. Eng. Part H J. Eng. Med., **215**(5), pp. 487–496.
[80] Spilker, R. L., Suh, J. K., and Mow, V. C., 1992, "A finite element analysis of the indentation stress-relaxation response of linear biphasic articular cartilage.," J. Biomech. Eng., **114**(2), pp. 191–201.
[81] Wheatley, B. B., Fischenich, K. M., Button, K. D., Haut, R. C., and Haut Donahue, T. L., 2015, "An optimized transversely isotropic, hyper-poro-viscoelastic finite element model of the meniscus to evaluate mechanical degradation following traumatic loading.," J. Biomech., **48**(8), pp. 1454–60.
[82] Spilker, R. L., Donzelli, P. S., and Mow, V. C., 1992, "A transversely isotropic biphasic finite element model of the meniscus," J. Biomech., **25**(9), pp. 1027–1045.
[83] Swedberg, A. M., Reese, S. P., Maas, S. a, Ellis, B. J., and Weiss, J. a, 2014, "Continuum description of the Poisson′s ratio of ligament and tendon under finite deformation.," J. Biomech., pp. 1–9.
[84] Qasim, M., Natarajan, R. N., An, H. S., and Andersson, G. B. J., 2012, "Initiation and progression of mechanical damage in the intervertebral disc under cyclic loading using continuum damage mechanics methodology: A finite element study.," J. Biomech., **45**(11), pp. 1934–40.
[85] Jacobs, N. T., Cortes, D. H., Peloquin, J. M., Vresilovic, E. J., and Elliott, D. M., 2014, "Validation and application of an intervertebral disc finite element model utilizing independently constructed tissue-level constitutive formulations that are nonlinear, anisotropic, and time-dependent," J. Biomech., **47**(11), pp. 2540–2546.

[86] Haut Donahue, T. L., Hull, M. L., Rashid, M. M., and Jacobs, C. R., 2002, "A finite element model of the human knee joint for the study of tibio-femoral contact.," J. Biomech. Eng., **124**(3), p. 273.
[87] Ayturk, U. M., and Puttlitz, C. M., 2011, "Parametric convergence sensitivity and validation of a finite element model of the human lumbar spine," Comput. Methods Biomech. Biomed. Engin., **14**(8), pp. 695–705.
[88] Oomens, C. W. J., Maenhout, M., van Oijen, C. H., Drost, M. R., and Baaijens, F. P., 2003, "Finite element modelling of contracting skeletal muscle.," Philos. Trans. R. Soc. Lond. B. Biol. Sci., **358**(1437), pp. 1453–60.
[89] Johansson, T., Meier, P., and Blickhan, R., 2000, "A finite-element model for the mechanical analysis of skeletal muscles.," J. Theor. Biol., **206**(1), pp. 131–49.
[90] Blemker, S. S., Pinsky, P. M., and Delp, S. L., 2005, "A 3D model of muscle reveals the causes of nonuniform strains in the biceps brachii.," J. Biomech., **38**(4), pp. 657–65.
[91] Gras, L. L., Mitton, D., Viot, P., and Laporte, S., 2012, "Hyper-elastic properties of the human sternocleidomastoideus muscle in tension," J. Mech. Behav. Biomed. Mater., **15**, pp. 131–140.
[92] Rehorn, M. R., and Blemker, S. S., 2010, "The effects of aponeurosis geometry on strain injury susceptibility explored with a 3D muscle model.," J. Biomech., **43**(13), pp. 2574–81.
[93] Chi, S., Hodgson, J., Chen, J., Reggie Edgerton, V., Shin, D. D., Roiz, R. A., and Sinha, S., 2010, "Finite element modeling reveals complex strain mechanics in the aponeuroses of contracting skeletal muscle.," J. Biomech., **43**(7), pp. 1243–50.
[94] Hodgson, J. a, Chi, S.-W., Yang, J. P., Chen, J.-S., Edgerton, V. R., and Sinha, S., 2012, "Finite element modeling of passive material influence on the deformation and force output of skeletal muscle.," J. Mech. Behav. Biomed. Mater., **9**, pp. 163–83.
[95] Khodaei, H., Mostofizadeh, S., Brolin, K., Johansson, H., and Osth, J., 2013, "Simulation of active skeletal muscle tissue with a transversely isotropic viscohyperelastic continuum material model.," Proc. Inst. Mech. Eng. H., **227**(5), pp. 571–80.
[96] Clemen, C. B., Benderoth, G. E. K., Schmidt, A., Hübner, F., Vogl, T. J., and Silber, G., 2017, "Human skeletal muscle behavior in vivo: Finite element implementation, experiment, and passive mechanical characterization," J. Mech. Behav. Biomed. Mater., **65**, pp. 679–687.
[97] Yucesoy, C. A., Koopman, B. H. F. J. M., Huijing, P. A., and Grootenboer, H. J., 2002, "Three-dimensional finite element modeling of skeletal muscle using a two-domain approach: linked fiber-matrix mesh model," J. Biomech., **35**(9), pp. 1253–1262.
[98] Lemos, R. R., Epstein, M., and Herzog, W., 2008, "Modeling of skeletal muscle: the influence of tendon and aponeuroses compliance on the force-length relationship.," Med. Biol. Eng. Comput., **46**(1), pp. 23–32.
[99] Böl, M., and Reese, S., 2008, "Micromechanical modelling of skeletal muscles based on the finite element method.," Comput. Methods Biomech. Biomed. Engin., **11**(5), pp. 489–504.
[100] Tang, C. Y., Zhang, G., and Tsui, C. P., 2009, "A 3D skeletal muscle model coupled with active contraction of muscle fibres and hyperelastic behaviour.," J. Biomech., **42**(7), pp. 865–72.
[101] Grasa, J., Ramírez, a, Osta, R., Muñoz, M. J., Soteras, F., and Calvo, B., 2011, "A 3D active-passive numerical skeletal muscle model incorporating initial tissue strains.

Validation with experimental results on rat tibialis anterior muscle.," Biomech. Model. Mechanobiol., **10**(5), pp. 779–87.
[102] Palevski, A., Glaich, I., Portnoy, S., Linder-Ganz, E., and Gefen, A., 2006, "Stress relaxation of porcine gluteus muscle subjected to sudden transverse deformation as related to pressure sore modeling.," J. Biomech. Eng., **128**(5), pp. 782–7.
[103] Jenkyn, T., Koopman, B., Huijing, P. a, Lieber, R. L., and Kaufman, K. R., 2002, "Finite element model of intramuscular pressure during isometric contraction of skeletal muscle.," Phys. Med. Biol., **47**, pp. 4043–4061.

CHAPTER 2:

SKELETAL MUSCLE TENSILE STRAIN DEPENDENCE: HYPERVISCOELASTIC NONLINEARITY

2.1 Introduction

The passive properties of skeletal muscle play a key role in force transmission throughout the tissue under active generation and passive stretch [1–4]. In tendon transfer procedures, the detachment and re-attachment of a muscle requires the estimation of resting length with manual tensioning, which can lead to deficiencies in contractile function [5,6]. As skeletal muscle is non-linear [7,8] and time dependent [9,10], this makes manually detecting proper resting length via passive muscle tension a challenge. To improve simulations such as finite element analyses, which can aid in surgical procedures by identifying proper muscle tension, we must first develop a complete understanding of the time and strain dependent properties of skeletal muscle.

As the modeling approaches for soft biological tissues such as skeletal muscle continue to advance, the formulation of constitutive relationships for these materials become more complex. This is derived from a need for a more complete understanding of the material behavior of these tissues, enabling simulations to accurately predict both local and global tissue function. While computational models of skeletal muscle have been developing since the introduction of the Hill model in 1938 [11], there have been relatively few studies of muscle tensile material properties

This chapter has been published as a Research Paper in the Journal of the Mechanical Behavior of Biomedical Materials (53, 2016). All content has been adapted with permission from Elsevier.

at the tissue level [8,12,13], with the majority of studies evaluating skeletal muscle compressive properties [14–18].

Studies of the structural response of individual muscle fibers [9] and intact muscles [7,10,19] are more prevalent. Since skeletal muscle is a highly organized collection of fibers and a collagenous connective matrix, which plays a key role in force transmission [20], it may be difficult to extrapolate whole muscle behavior from results of studies of individual fibers. Likewise, variations in anatomical structure between muscles from different locations in the body makes inference of the response of one muscle from the study of another a dubious proposition at best.

Many recent investigations into skeletal muscle properties have focused on hyperelastic material properties [7,8,13,17–19]. However, the number of studies examining the time dependency are limited to compressive conditions [14–16,18,21], single fiber [9,22] or whole muscle investigations [23–25], or utilize a linear or quasi-linear viscoelastic response [10,26,27]. Thus, to the author's knowledge, there have been no previous modeling efforts which have included nonlinear tissue level strain dependent viscoelastic behavior for skeletal muscle in tension. However, when developing such a model, one must take care to ensure that any efforts can be implemented into future computational analyses. This is typically done through the development of an energy based formulation instead of a stress based formulation, which prevents stress integration in a finite element simulation [28].

Thus, the goals of this study were to (1) examine the time and strain dependent material properties of skeletal muscle tissue subjected to consecutive stress relaxation cycles and to (2)

implement a fully nonlinear hyperviscoelastic model to capture muscle nonlinearity in both time independent modulus and viscoelastic relaxation behavior under passive tensile conditions.

2.2 Methods

2.2.1 Specimen Preparation

Longitudinal (along the fiber direction) load-relaxation tests were performed on nine tibialis anterior (TA) muscle samples harvested from nine New Zealand White rabbits (one sample per animal). The handling of all study animals was performed with approval from the Mayo Clinic Institutional Animal Care and Use Committee. Specimens were cut from the muscle midbelly away from surrounding fascia and aponeurosis to a thickness of 3.6 mm using a razor tissue punch with the long axis coinciding with muscle fiber direction (Figure 2-1). Specimens were 22.0 ± 4.1 mm long and 5.4 ± 1.0 mm wide as measured with digital calipers. All testing was completed within two hours of sacrifice to mitigate the effects of post-mortem rigor [16,29]. Testing was performed at room temperature, and specimens were kept moist continually using a saline mist spray.

2.2.2 Stress Relaxation Tests

Load-relaxation tests were performed on an MTS 858 material test device (MTS, Eden Prairie, MN) with specimens mounted in thin film clamps (Imada, Northbrook, IL) (Figure 2-1). A pre-stress condition corresponding to 0.1% of the ultimate stress of the muscle by direction [13] was applied. Specimen length was calculated as grip to grip length and strain was calculated from crosshead displacement per previous work on rabbit skeletal muscle [13]. Samples were subject to five load-relaxation cycles of 0.7 mm (mean strain of 0.031 ± 0.002 standard error of mean)

followed by a 300-second relaxation period [12]. Operating in this range ensured that tissue remained below the ultimate strain [13] and would not be strained to the point of creating damage or plastic deformation [9]. Force measurements were sampled at 20 Hz using a 1-kgf load cell (Transducer Techniques, Temecula, CA). As the relaxation behavior of muscles under stress relaxation has been shown to be strain-rate insensitive [30], all material tests were performed at a uniform rate of displacement. Tissues were elongated at a rate of 3.8 mm/sec, corresponding to 0.1 fiber-lengths/sec [31].

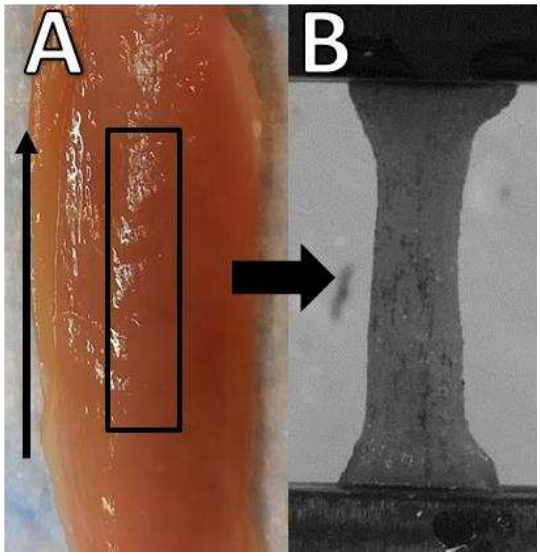

Figure 2-1: Midbelly specimens were excised from the tibialis anterior (A) along the fiber direction (vertical arrow), loaded, and tested in a material testing system with thin film grips (B). Samples were cut into rectangular strips and the apparent dog bone shape (B) is a result of tissue compression at the grips and not changes in cross sectional area with sample length.

2.2.3 Raw Data Analysis

First Piola-Kirchoff stress ($\boldsymbol{P}$) was calculated as the reaction force divided by the initial cross-sectional area and converted into Second Piola-Kirchoff by $\boldsymbol{S} = \frac{\boldsymbol{P}}{\boldsymbol{F}}$ where $\boldsymbol{F}$ is the deformation gradient. The relaxation ratio of each individual zeroed stress relaxation step was calculated as the mean stress over the final one second of relaxation divided by the peak stress from that step. Material elongation was determined using crosshead displacement. Green strain was calculated

as the mechanical correlate to $\boldsymbol{S}$ (Equation 1, where e_G is one dimensional Green strain and e is engineering strain). All relaxation data was processed in Matlab (The Mathworks, Inc., Natick, MA) using a first order Savitsky-Golay filter (*sgolayfilt*) as it is highly effective in reducing high frequency noise.

$$e_G = \frac{1}{2}[(1+e)^2 - 1] \tag{1}$$

2.2.4 Linear Viscoelastic Prony Series

Calculated stress relaxation data for each strain increment (five steps each and nine specimens for a total of 45 stress relaxation steps) were fitted to a constitutive formulation for viscoelastic materials [14,32] (Equation 2, where $S(e_G, t)$ is the stress at time t and strain level e_G, $E(t)$ is the time dependent elastic modulus, and τ is an integration variable). A three-term linear Prony series [14,32–35] was utilized to describe the time dependent elastic modulus (Equation 3, where E_0 is the instantaneous modulus, E_n are relaxation coefficients, and τ_n are time constants). A nonlinear optimization (*lsqnonlin*) in Matlab applied the Levenberg-Marquardt unbounded local optimizing algorithm to fit experimental and model data. This approach varied all seven of the material properties from Equation 3 to minimize the residuals between the model output and experimental data at each time point [7,32,36–38]. Additional weight was given to the peak response to ensure a good fit throughout loading and initial relaxation by mutiplying the peak error by the total number of data points in each step [36]. The E_0 initial parameter value was set to 10 kPa, the E_n terms were initially set to values of 0.5, 0.25, and 0.15, respectively, while the τ_n terms were set to 0.1s, 10s, and 100s, respectively. These values were determined by performing the optimization under a range of initial values and comparing the results to locate the optimal fits. The E_n terms were set to decreasing values as a large portion of tissue relaxation

typically occurs over very short time periods in studies of biological tissues [14,15,35,36]. Each parameter was then scaled within the optimization such that all initial values remain on the same order of magnitude, which improves the fitting procedure [36,38].

$$S(e_G(\tau), t) = \int_0^t E(t-\tau)\frac{de_G(\tau)}{d\tau}d\tau \quad (2)$$

$$E(t) = E_0\left\{1 - \sum_{n=1}^{3} E_n\left[1 - \exp\left(-\frac{t}{\tau_n}\right)\right]\right\} \quad (3)$$

2.2.5 Fully Nonlinear Hyperviscoelastic Modeling

Experimental data was then averaged together to generate a single set of mean stress relaxation data in addition to the nine individual specimens. These data were fit to a fully nonlinear hyperviscoelastic model. Here the hyperelasticity was characterized by an isotropic polynomial strain energy density (SED) function [36,39] (Equation 4, where $\lambda = \frac{l}{l_0}$, $\Psi(\lambda)$ is the stretch dependent strain energy density, λ_i are the stretches in the longitudinal (λ_1) and transverse (λ_2, λ_3) directions, respectively, and a_{2i} are material constants). The Poisson's ratio (ν) of unbathed skeletal muscle was assumed to be 0.47, per a previous study of fresh skeletal muscle under uniaxial tension [8]. The resulting transverse strain was driven by the Poisson effect ($\nu = \frac{-e_{trans}}{e_{long}}$), resulting in a simplification of the three stretches to only a longitudinal stretch and strain dependence shown in Equation 5.

$$\Psi(\lambda) = \sum_{i=1}^{2} a_{2i}\,(\lambda_1^2 + \lambda_2^2 + \lambda_3^2 - 3)^{2i} \quad (4)$$

$$\lambda_1^2 + \lambda_2^2 + \lambda_3^2 = \lambda_{long}^2 + 2\lambda_{trans}^2 = \lambda_{long}^2 + 2(1+e_{trans})^2 = \lambda_{long}^2 + 2\left(1 - \nu e_{long}\right)^2 \quad (5)$$

The instantaneous modulus E_0 was then calculated as a function of stretch from the SED equation (Equation 6) [39]. Previous studies have applied a polynomial expression to identify the dependence of Prony series parameters on stretch level for compressed muscle [15] and spinal

cord [32]. However, we chose to employ a simple exponential function for the purpose of minimizing the number of optimized parameters while still maintaining a robust, non-linear function. Thus, the relaxation coefficients and time constants were given exponential dependence on longitudinal stretch (Equations 7 and 8, where α_n, β_n, μ_n, and ω_n are material properties). A stretch and time dependent hyperviscoelastic tangent modulus ($E(\lambda(\tau), t)$, which directly incorporates the strain energy density function through E_0 and the viscoelastic nonlinearity through E_n and $\tau_n(\lambda)$, can then be defined (Equation 9). The complete nonlinear constitutive relationship for second Piola-Kirchoff stress is then developed (Equation 10), highlighting the coupling between stretch and time dependence of the tangent modulus. It should be noted that this tangent modulus characterizes the stiffness behavior at a particular deformation and is highly nonlinear, thus it should not be confused a linear elastic Young's modulus.

$$E_0(\lambda) = 4\frac{\partial^2\Psi(\lambda)}{\partial\lambda^2\partial\lambda^2} = 4\left[2a_2 + 12a_4\left(\lambda_{long}^2 + 2\lambda_{trans}^2 - 3\right)^2\right] \tag{6}$$

$$E_n(\lambda) = \alpha_n exp\left(-\beta_n(\lambda_{long}^2 - 1)^2\right) \tag{7}$$

$$\tau_n(\lambda) = \mu_n exp\left(-\omega_n(\lambda_{long}^2 - 1)^2\right) \tag{8}$$

$$E(\lambda, t) = E_0(\lambda)\left\{1 - \sum_{n=1}^{3} E_n(\lambda)\left[1 - \exp\left(-\frac{t}{\tau_n(\lambda)}\right)\right]\right\} \tag{9}$$

$$S(\lambda(\tau), t) = \int_0^t E(\lambda(\tau), t-\tau)\frac{d\lambda(\tau)}{d\tau}d\tau \tag{10}$$

The fitting procedure was similar to the optimization performed for single step data, but it included all five consecutive relaxation steps and the expanded constitutive relation outlined above. Ten separate optimizations were performed, each of the nine individual specimens in addition to an averaged set of mean experimental data. The nine individual specimens provided statistical measurement of variability, while the set of mean experimental data was used to develop a single set of constitutive parameters as averaging parameters from multiple specimens

is an ineffective approach in constitutive mode ling [40,41]. The initial parameter values were structured similarly to the linear Prony series fitting, where initial E_n values of 0.5, 0.25, and 0.15 were used along with initial τ_n values of 0.1s, 10s, and 100s. This was achieved by setting all β_n and ω_n initially to a value of zero, which results in no initial strain dependence. All initial parameter values can be found in Table 2-1. To verify uniqueness and global minima, the optimization was repeated with each parameter either reduced by 50% or increased by 100%.

Table 2-1: Initial parameter values for the fully hyperviscoelastic model fitting. Each parameter was scaled such that the initial values all shared the same order of magnitude. All α_n, β_n, and ω_n parameters are unitless.

Parameter	**a_2 [kPa]**	**a_4 [kPa]**	**$\alpha_{1,2,3}$**	**$\beta_{1,2,3}$**	**$\mu_{1,2,3}$ [s]**	**$\omega_{1,2,3}$**
Initial Value	10	1000	0.5, 0.25, 0.15	0	0.1, 10, 100	0

While the fully nonlinear hyperviscoelastic model provides a highly robust approach, justification for employing such a complex constitutive formulation is needed. Specifically, it was unclear if both the hyperelasticity and nonlinear viscoelasticity were both necessary. Thus, the outlined optimization procedure to fit mean experimental data was employed with four separate models combining linear and nonlinear components from Equations 2 through 7. These models included the fully nonlinear model (FNM), a model including a linear instantaneous modulus and nonlinear viscoelasticity (LINV, Equations 2, 3, 7, and 8), a nonlinear instantaneous modulus and linear viscoelasticity approach (NILV or often referred to quasilinear viscoelasticity or QLV, Equations 2-6), and a fully linear model (FLM, Equations 4-10) (Equation 2).

2.2.6 Statistics

The goodness of fit for each load-relaxation cycle was evaluated with the *goodnessOfFit* function in Matlab [36]. In brief, the "fit" value was determined from the normalized mean square (Equation 11), where y_i^m and y_i^e are the model and experimental stress values, respectively, at the i^{th} data point and n is the total number of data points. Fits range from -∞ (worst) to 1 (perfect). Additionally, the overall percent error and peak percent error (percent difference between peak response at the end of loading) were calculated.

$$fit = 1 - \sum_{i=1}^{n} \left[\frac{y_i^m - y_i^e}{y_i^m - mean(y_i^e)} \right]^2 \quad (11)$$

Muscle behavior was assessed by comparing the dependence on strain of all Prony series terms (Equation 3) and the relaxation ratio with a general linear model, with significance set at $p<0.05$ for all tests. This was performed in Minitab Statistical Software (Minitab Inc., State College, PA). The coefficients of variation (CV) was determined for all statistical measures in the linear Prony series model to identify the accuracy of all fits. The CV was also calculated for all statistical measures and parameter values for the fully nonlinear model for five consecutive steps for all nine individual specimens.

2.3 Results

The peak and equilibrium stresses for all specimens show a nonlinear stress-strain relationship (Figure 2-2). As each specimen was displaced 0.7 mm, variations in gauge length provide a more continuous stress-strain graph than if each specimen was strained at identically discrete intervals. Using a nonlinear optimization algorithm in MATLAB proved to be an excellent approach to fit experimental data both visually (Figure 2-3) and by numerical analysis (Table 2-2), with both low percent error values and fit values close to the optimal value of 1. The optimizing process

also showed an excellent ability to fit both the peak response as well as the shape of the relaxation behavior. The optimization procedure was successful for both the linear model fit to individual zeroed stress relaxation steps (Figure 2-3A and Table 2-2) as well as the nonlinear model fit to five consecutive steps (Figure 2-3B and Table 2-2).

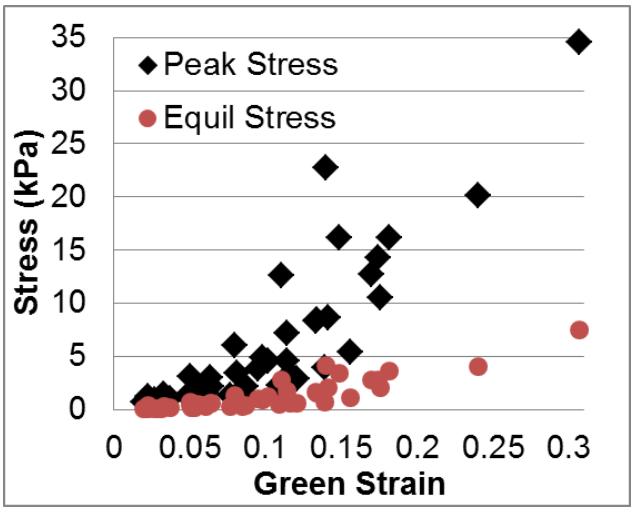

Figure 2-2: Stress-strain data for all peak (black diamonds) and equilibrium (red circles) data from all nine samples. Note the nonlinear behavior for both peak and equilibrium responses in addition to the dispersed strain values.

Table 2-2: Numerical optimization results for the linear Prony series fit to each normalized individual step and the fully hyperviscoelastic model optimized to all nine specimens.

Statistical Measurement	Mean or Coefficient of Variation	Linear Model (Equations 2-3) Isolated Steps (45 individual steps)	Nonlinear Model (Equations 4-10) Full Steps (9 specimens with 5 steps each)
Complete Response Error	Mean (%)	2.73	4.93
	CV	0.45	0.28
Peak Response Error Only	Mean (%)	2.53E-5	6.65
	CV	1.28	0.25
Fit Value	Mean	0.967	0.999
	CV	0.022	7.6E-4

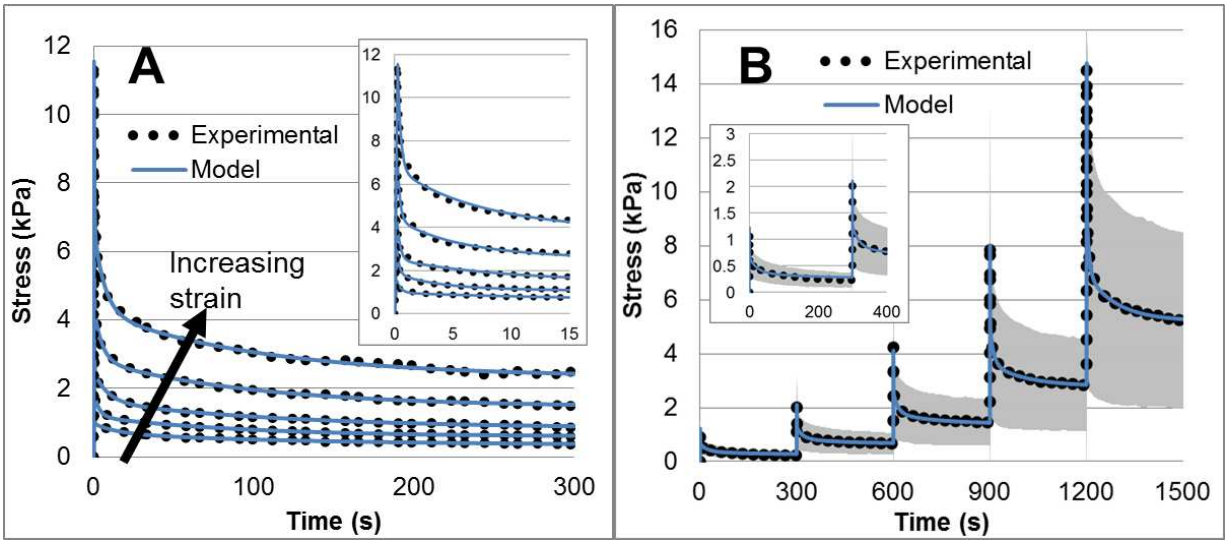

Figure 2-3: Viscoelastic Prony fitting to five isolated stress relaxation steps of a single specimen (A), with loading and initial relaxation shown inset. Arrow indicates curves go from lowest strain level on bottom to highest on top. Nonlinear hyperviscoelastic fitting to mean experimental data (B) with initial steps shown inset for clarity.

Prony series relaxation coefficients and the instantaneous modulus for all five steps of all nine specimens were plotted (45 total) were plotted against Green strain to provide visual inspection of the dependence of modulus and relaxation behavior on strain level (Figure 2-4). Here a positive slope corresponds to increases with increasing strain, while a negative slope conversely suggests a decrease. The general linear model analysis of all Prony series coefficients showed that muscle relaxation behavior exhibited strain dependence (Figure 2-4), as changes in relaxation parameters were observed (E_2 positive slope, p<0.0005 and E_3 negative slope, p<0.0005) with increasing strain level. The instantaneous modulus E_0 also had a positive slope (p<0.0005). Alternatively, the analysis showed no changes in the E_1relaxation parameter (p=0.157) rate parameters (p=0.184, p=0.205, and p=0.157 for τ_1, τ_2, and τ_3, respectively). The mean values (and coefficients of variation in percent) for the rate parameters were found to be 0.109 (0.060) seconds, 5.29 (0.44) seconds, and 108 (0.54) seconds. The relaxation ratio showed

no dependence on strain (p=0.777) and had a mean value of 0.211 with a coefficient of variation of 0.18.

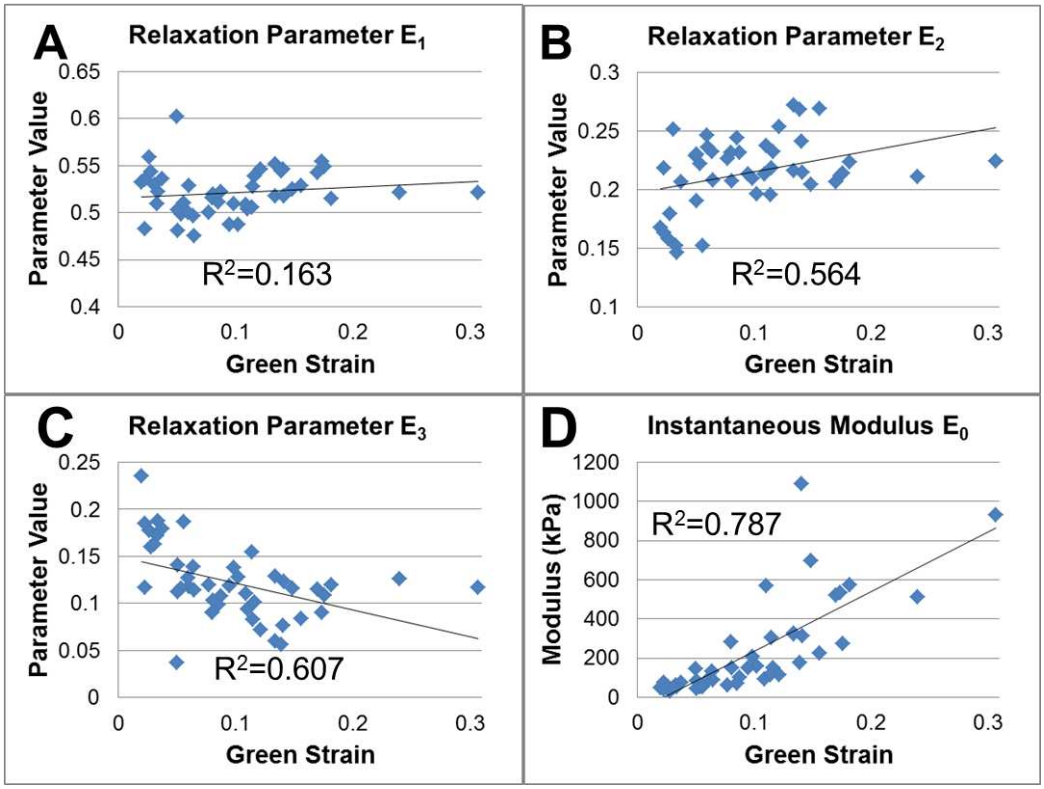

Figure 2-4: Viscoelastic Prony series coefficients which were found to have a significant dependence on deformation level. The second relaxation parameter E_2 (B) had a positive slope ($p<0.0005$), while the third relaxation parameter E_3 (C) had a negative slope ($p<0.0005$). The instantaneous modulus E_0 (D) also increased with strain ($p<0.0005$).

The mean data fit yielded a single set of constitutive parameters (Table 2-3), which can be utilized in computational modeling efforts. This single optimization resulted in a 2.97% error between the mean data and model, with a fit value of 0.999 and mean peak errors of 2.40% (Table 2-4). Multiplying initial parameters by 50% and 200% did not significantly affect either the model fit or optimized parameters. A visual representation of the model tangent stiffness provides a useful method to highlight the dependence of material behavior on both strain level and relaxation time (Figure 2-5).

Table 2-3: Optimized hyperviscoelastic constitutive parameters fitted to mean experimental data with coefficient of variation percent in parentheses.

SED Ψ		**Relaxation Coefficients E_n**				**Rate Coefficients τ_n**			
a_2 [kPa]	6.62 (0.52)	$\alpha_{1,2,3}$ [s]	0.641 (0.089)	0.124 (0.53)	0.114 (0.47)	$\mu_{1,2,3}$ [s]	0.202 (0.25)	12.2 (1.2)	262 (2.1)
a_4 [kPa]	3820 (0.85)	$\beta_{1,2,3}$	-2.27 (2.6)	3.67 (2.7)	1.46 (8.6)	$\omega_{1,2,3}$	-9.78 (1.1)	11.6 (2.8)	-5.25 (3.3)

Table 2-4: Fitting comparisons between linear and nonlinear models, showing overall mean error, mean error of the five peak values, and the normalized mean square error goodness of fit.

Statistical Measurement	**Fully Nonlinear Model**	**Linear Instantaneous, Nonlinear Viscoelastic**	**Nonlinear Instantaneous, Linear Viscoelastic**	**Fully Linear Model**
Complete Response Error (%)	3.20	15.1	4.08	33.0
Peak Response Error Only (%)	3.39	18.3	5.58	106
NMSE Fit Value	1.00	0.984	0.999	0.937

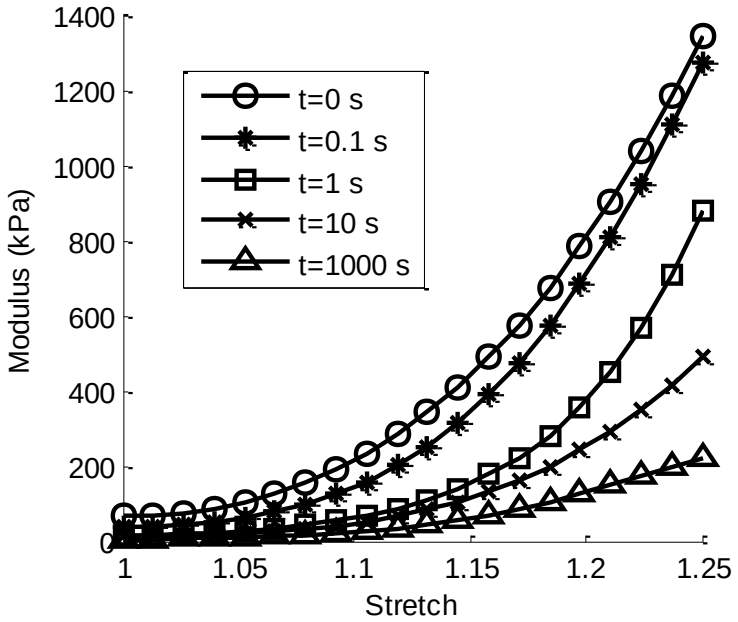

Figure 2-5: Tangent modulus behavior for the implemented fully nonlinear hyperviscoelastic constitutive model. This model exhibits dependence on both stretch level (x-axis) as well as relaxation time (various curves). The instantaneous response (circle markers, t=0 s) and equilibrium behavior (triangle markers, t=1,000 s) along with intermediate times are shown, highlighting the evolution of modulus behavior over time.

The model justification results (Figure 2-6 and Table 2-4) show that the fully nonlinear model (FNM) far outperformed others using a linear instantaneous response. The fully linear model (FLM) failed to capture any sufficient material behavior with an error of over 30% (Table 2-4). The two models combining linearity and nonlinearity (linear instantaneous nonlinear viscoelastic - LINV and nonlinear instantaneous linear viscoelastic – NILV) did an improved job predicting experimental behavior overall, particularly the NILV model (Table 2-4, ~4% overall error). The discrepancies between the FNM model and the LINV model can be observed within the first stress relaxation step (Figure 2-6).

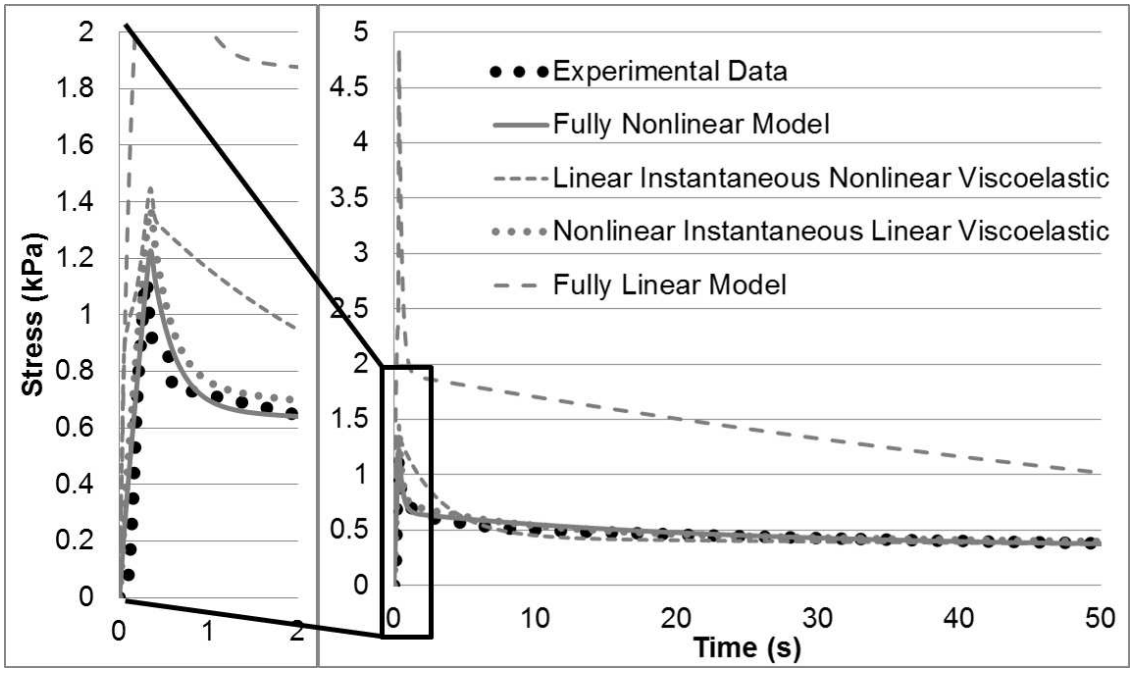

Figure 2-6. Comparison of various linear and nonlinear models fitted to averaged experimental data with only the first fifty seconds of the first step shown. Initial loading and relaxation (from 0-2 seconds) is further highlighted on the left.

2.4. Discussion

2.4.1 Experimental Data Analysis

The experimental data shown in this work provides a more continual stress-strain relationship (Figure) when compared to studies for which each specimen is strained to identical discrete values. This allows for a more detailed investigation of the effect of strain level on passive skeletal muscle mechanics. The analyzed experimental data from this work can be compared to previously published works which studied the time dependent behavior of skeletal muscle in tension [9,12,24]. These investigations similarly showed a large portion of the relaxation occurs over a short time period, after which the tissue slowly transitions into an equilibrium state. Abraham et al., (2013) comparably investigated stress relaxation of excised New Zealand White Rabbit tibialis anterior, albeit it at a single 10% strain step and observed a steady state modulus of roughly 70 kPa for excised tissue compared to an equilibrium modulus value of around 20 kPa at 10% strain from our raw data. The fully nonlinear hyperviscoelastic model similarly predicts an equilibrium tangent modulus of 24 kPa at 10% strain from our data.

Data from Takaza et al., (2013) and Morrow et al., (2010) suggest a stress level of between 5 and 40 kPa at 10% strain in constant rate testing loaded at 0.05%/s. Best et al., (1994) show a stress level of ~350 kPa at 10% strain, at a much higher strain rate (667%/s), which certainly contributed to higher stress values. Our data shows stress values of roughly 5-10 kPa for peak and 2-3 kPa for equilibrium stress at 10% strain. However, as Meyer et al., (2011) showed with a single muscle fiber that superposition does not hold and consecutive stress relaxation cycles result in stresses lower than a single cycle, this may account for the discrepancies between our data and other literature. Specifically, the increased stiffness observed by Abraham et al would

be a result of a single stress relaxation step at 10% strain, compared to 3-4 smaller steps of roughly 3% strain, while the constant rate elongation tests would see a compounding effect, resulting in increased stresses.

2.4.2 Linear Prony Series Viscoelasticity

Analyzing the optimized linear Prony series coefficients as well as the relaxation ratio provides insight into the transient performance of skeletal muscle as a function of strain (Figure 2-4). Outside of a study by Meyer et al., (2011) who investigated viscoelasticity of single fibers, there is limited published data to compare with our data. The first result to note is that the relaxation ratio exhibited no dependence on strain level, which appears to agree with the findings of Meyer et al., (2011) under consecutive stress relaxation steps on single fibers. The strong increase in instantaneous modulus with strain further supports the well-documented tensile hyperelasticity of skeletal muscle in the fiber direction [7,8,42].

The changes observed in Prony series coefficients with strain shows the course under which this relaxation occurs differs as a function of material strain. Specifically, the increases in the second relaxation coefficient coupled with a decrease in the third relaxation coefficient implies that with increasing strain the total rate of relaxation is increasing. This is simplified by the fact that the rate parameters did not change with strain level. These findings differ from Meyer et al., (2011) who found increasing stress relaxation steps resulted in a slower relaxation rate. However, the highly collagenous extracellular matrix [2,43,44] supports a large portion of muscular force transmission [3,20,45] and as such could certainly affect the relaxation behavior of the tissue. Previous studies have suggested that collagen fibers play a role in the time dependent response of

the meniscus [46] and cartilage [47], thus it is no surprise that the viscoelastic behavior of muscle differs between the fiber and tissue level.

2.4.3 Fully Nonlinear Viscoelastic Model

To the author's best knowledge, this work presents the first fully nonlinear hyperviscoelastic model of tissue level skeletal muscle under tensile strain. Previous works have evaluated the viscoelastic nonlinearity of a single muscle fiber [9,22], have utilized a linear or quasi-linear viscoelastic response [10,26,27], or investigated other biological tissues such as spinal ligaments [48], the spinal cord [32], and skeletal muscle in compression [15]. Meyer et al., (2011)'s investigation of single fiber viscoelasticity was very effective in capturing the strain dependent viscosity of the mouse single fiber. We chose to employ a hyperelastic model as fiber bundle behavior exhibits nonlinear stiffness when compared to individual fibers or groups of fibers [20]. This SED based hyperelastic relationship (Equation 3) is also advantageous over stress based functions [9,15,32] which must be integrated to calculate strain energy within an analysis [28]. Thus, this constitutive formulation provides a simpler model to incorporate in finite element analyses. The fully hyperviscoelastic model exhibited not only the robustness to match various strain levels, but the accuracy to capture both the peak responses (average error of 3.29% for the five peaks) and the relaxation shape (3.20% overall error and a 0.999 total fit value). This novel formulation is capable of combining a technically sound continuum mechanics based hyperelastic SED function (Equation 3, which is polyconvex and positive definite) and a flexible exponential viscoelastic definition (Equations 6 and 7). The optimized coefficients (Table 2-3) can be directly incorporated into analyses in which the fully nonlinear behavior of the tissue is of

importance, such as repeated loading simulations or analyses involving inhomogeneous deformation.

As this hyperviscoelastic model was applied numerically, there remains the mathematical possibility for a negative modulus based on the constitutive parameter values, which is clearly not physically reasonable. This can be investigated by identifying the role of each parameter within the constitutive model. The a_2 and a_4 parameters describe the nonlinear behavior of the strain energy density function, and as such can be related to a stiffness or modulus term. The α_n terms behave similarly to the E_n terms from Equation 3, where they reduce a certain amount of the modulus over time, corresponding to each time constant, which are largely described with the μ_n terms. The remaining β_n and ω_n terms characterize the strain dependence of the α_n and μ_n terms, respectively, through an exponential function (Equations 7 and 8). We can see that positive β_n and ω_n values result in increases in relaxation with increases in stretch level, while negative β_n and ω_n values conversely result in decreases in relaxation with increases in stretch level. Figure 2-5 highlights the tangent moduli values for this model as a function of relaxation time and strain level, showing that the model does not implement a negative modulus, which would not satisfy thermodynamic equilibrium.

A three term Prony series was selected for this work as it provides an excellent fit to experimental data while minimizing the total number of parameters. While increasing the number of Prony series terms increases the fitting potential, this is offset with computational capabilities, as minimizing the total number of parameters improves the accuracy of the optimization procedure [36]. However, some studies have employed higher order series

[14,15,32,49] with good success. Conversely, lower order Prony series have also been utilized effectively in studies of biological tissues [50,51]. However, the third order series allows for rate parameters dispersed at decade values (roughly 0.1s, 1s, and 100s for μ_n, Table 2-3), which are able to capture the short term, intermediate, and long term relaxation behavior of the tissue. It is uncertain exactly how increasing or decreasing the Prony series order would affect the model, but the effectiveness of the utilized approach remains clear.

This highly nonlinear tangent modulus (Figure 2-5) further supports the well documented nonlinear response of skeletal muscle in longitudinal tension [7,8,13,52]. The nonlinear shape also continues throughout relaxation, as highlighted by the various curves at increasing relaxation times, suggesting that skeletal muscle tensile non-linearity exists both in the instantaneous and equilibrium state. Figure 2-5 also provides further evidence of a short and steep initial relaxation phase, as from zero relaxation (circle) to 0.1 seconds (asterisk) a significant portion of the tangent modulus is reduced. This is then followed by a more drastic decrease from 0.1 to 1 second (square), particularly at lower stretch values. Conversely, the changes in material behavior occurring between 10 (x) and 1000 seconds (triangle, when the material has reached equilibrium) represent a similar reduction in modulus, yet this occurs over a much longer time period. Furthermore, the fact that this modulus remains positive throughout complete relaxation and over a range of stretch values confirms the notion that the numerical application of this model obeys natural physical conditions.

The model justification study (Figure 2-6 and Table 2-4) highlighted the improved fitting of the fully nonlinear model over the fully linear and LINV approaches. Specifically, the models

incorporating linear instantaneous behavior had inferior agreement, while the NILV (also known as quasi-linear viscoelasticity or QLV) model was able to produce a very strong overall fit to the data as well (~4% error, Table 2-4). Discrepancies between quasilinear and fully nonlinear modeling were observed at lower strains as the first step saw over 15% total error and over 20% peak error (Figure 2-6). However, the use of a quasilinear formulation or fully nonlinear formulation will likely depend on utilization as the ~1% difference between these two approaches is functionally quite small. Current utilization of fully nonlinear viscoelasticity requires a generous amount of computational power or time, thus the use of QLV is likely appropriate. As finite element analyses naturally develop more complex constitutive formulations and discrete physiological components to improve clinical significance, the inclusion of a fully nonlinear response may one day be a standard approach.

2.4.4 Study Limitations and Improvements

While this study effectively explores the strain-dependent changes in the temporal response of muscle tissue, further studies will be needed to establish a full understanding of tissue behavior. Specifically, single cycle load-relaxation studies over a range of strain levels and rates are needed to completely assess the extent to which muscle tissue does not adhere to the principle of superposition and to identify strain rate dependence. These data could also be used to validate the proposed hyperviscoelastic model. It should also be noted that this work represents the response of a single muscle (in this case the New Zealand White Rabbit tibialis anterior with a sample size N=9) and that further experiments to identify nonlinear viscoelastic muscle behavior for different muscles would greatly aid in the confirmation of the proposed model. It remains unclear how

muscle curvature, pennation angle, possible changes in fiber type among other physiological characteristics may affect the viscoelastic response.

As this work only proposed an isotropic model, future studies should be performed to identify the viscoelastic behavior in the transverse direction as muscle is anisotropic [8,13]. However, from a computational standpoint, a simplified isotropic model allows for good global accuracy while minimizing computational cost [53]. Muscle studies in compression have identified transverse anisotropy under carefully controlled conditions [17] in addition to differences between the time dependent behavior as a function of loading orientation [14,15,18], yet it is unclear how these properties translate, if at all, to tension. Development of data sets including shear and volumetric loading conditions would provide a full picture of passive muscle behavior in tension. These data could then be incorporated by expanding the SED function from Equation 3 and subsequently applying independent viscoelastic behavior for each term. This would broaden the current implementation to include transverse isotropy in addition to shear and volumetric behavior for use in a more complex three dimensional finite element model.

Additionally, the ability of the utilized hyperviscoelastic constitutive model to predict any strain rate dependence remains unclear. The inclusion of any plastic strain, such as non-recoverable changes in length under *in vitro* tensile conditions, could also be added to improve finite element implementation. While there may be some concern over the use of second Piola-Kirchoff stress over Cauchy stress, all data analysis was performed in the reference configuration and a push-forward operation could be performed to more closely reflect the local material behavior if desired [39]. Finally, while the employed stretch level viscoelastic dependence (Equations 6 and

7) proved very effective at matching experimental data, a different formulation could possibly improve this model.

2.5 Conclusion

This study shows that the viscoelastic response of skeletal muscle has a statistically significant dependence upon strain level as evaluated by comparison of the relaxation response of five consecutive load-relaxation cycles. Furthermore, a novel fully nonlinear model including both an explicit hyperelastic strain energy density function and a strain dependent viscoelastic formulation provided an excellent fit to experimental data. However, the use of quasilinear viscoelasticity (QLV) was also able to capture material behavior to a high degree. Thus, for most models of skeletal muscle a QLV approach is appropriate although future work to reduce computation time would make fully nonlinear modeling an attractive approach.

REFERENCES

[1] Brown, S. H. M., Carr, J. A., Ward, S. R., and Lieber, R. L., 2012, "Passive mechanical properties of rat abdominal wall muscles suggest an important role of the extracellular connective tissue matrix," J. Orthop. Res., **30**(8), pp. 1321–1326.

[2] Gillies, A. R., and Lieber, R. L., 2011, "Structure and function of the skeletal muscle extracellular matrix.," Muscle Nerve, **44**(3), pp. 318–31.

[3] Huijing, P. A., 1999, "Muscle as a collagen fiber reinforced composite: A review of force transmission in muscle and whole limb," J. Biomech., **32**(4), pp. 329–345.

[4] Smith, L. R., Gerace-Fowler, L., and Lieber, R. L., 2011, "Muscle extracellular matrix applies a transverse stress on fibers with axial strain," J. Biomech., **44**(8), pp. 1618–1620.

[5] Fridén, J., and Lieber, R. L., 1998, "Evidence for muscle attachment at relatively long lengths in tendon transfer surgery.," J. Hand Surg. Am., **23**(1), pp. 105–110.

[6] Fridén, J., and Lieber, R. L., 2002, "Tendon transfer surgery: clinical implications of experimental studies.," Clin. Orthop. Relat. Res., (403 Suppl), pp. S163-70.

[7] Calvo, B., Ramírez, A., Alonso, A., Grasa, J., Soteras, F., Osta, R., and Muñoz, M. J., 2010, "Passive nonlinear elastic behaviour of skeletal muscle: Experimental results and model formulation," J. Biomech., **43**(2), pp. 318–325.

[8] Takaza, M., Moerman, K. M., Gindre, J., Lyons, G., and Simms, C. K., 2012, "The anisotropic mechanical behaviour of passive skeletal muscle tissue subjected to large tensile strain," J. Mech. Behav. Biomed. Mater., **17**, pp. 209–220.

[9] Meyer, G. A., McCulloch, A. D., and Lieber, R. L., 2011, "A Nonlinear Model of Passive Muscle Viscosity," J. Biomech. Eng., **133**(9), p. 91007.

[10] Myers, B. S., Woolley, C. T., Slotter, T. L., Garrett, W. E., and Best, T. M., 1998, "The influence of strain rate on the passive and stimulated engineering stress--large strain behavior of the rabbit tibialis anterior muscle.," J. Biomech. Eng., **120**(1), pp. 126–132.

[11] Hill, A. V., 1938, "The Heat of Shortening and the Dynamic Constants of Muscle," Proc. R. Soc. B Biol. Sci., **126**(843), pp. 136–195.

[12] Abraham, A. C., Kaufman, K. R., and Haut Donahue, T. L., 2012, "Phenomenological consequences of sectioning and bathing on passive muscle mechanics of the New Zealand white rabbit tibialis anterior," J. Mech. Behav. Biomed. Mater., **17**, pp. 290–295.

[13] Morrow, D. A., Haut Donahue, T. L., Odegard, G. M., and Kaufman, K. R., 2010, "Transversely isotropic tensile material properties of skeletal muscle tissue," J. Mech. Behav. Biomed. Mater., **3**(1), pp. 124–129.

[14] Van Loocke, M., Lyons, C. G., and Simms, C. K., 2008, "Viscoelastic properties of passive skeletal muscle in compression: Stress-relaxation behaviour and constitutive modelling," J. Biomech., **41**(7), pp. 1555–1566.

[15] Van Loocke, M., Simms, C. K., and Lyons, C. G., 2009, "Viscoelastic properties of passive skeletal muscle in compression-Cyclic behaviour," J. Biomech., **42**(8), pp. 1038–1048.

[16] Van Loocke, M., Lyons, C. G., and Simms, C. K., 2006, "A validated model of passive muscle in compression," J. Biomech., **39**(16), pp. 2999–3009.

[17] Böl, M., Ehret, A. E., Leichsenring, K., Weichert, C., and Kruse, R., 2014, "On the anisotropy of skeletal muscle tissue under compression.," Acta Biomater., **10**(7), pp. 3225–34.
[18] Pietsch, R., Wheatley, B. B., Haut Donahue, T. L., Gilbrech, R., Prabhu, R., Liao, J., and Williams, L. N., 2014, "Anisotropic compressive properties of passive porcine muscle tissue.," J. Biomech. Eng., **136**(11), p. 111003.
[19] Gras, L. L., Mitton, D., Viot, P., and Laporte, S., 2012, "Hyper-elastic properties of the human sternocleidomastoideus muscle in tension," J. Mech. Behav. Biomed. Mater., **15**, pp. 131–140.
[20] Meyer, G. A., and Lieber, R. L., 2011, "Elucidation of extracellular matrix mechanics from muscle fibers and fiber bundles," J. Biomech., **44**(4), pp. 771–773.
[21] Bosboom, E. M. H., Hesselink, M. K. C., Oomens, C. W. J., Bouten, C. V. C., Drost, M. R., and Baaijens, F. P. T., 2001, "Passive transverse mechanical properties of skeletal muscle under in vivo compression," J. Biomech., **34**(10), pp. 1365–1368.
[22] Bensamoun, S., Stevens, L., Fleury, M. J., Bellon, G., Goubel, F., and Ho Ba Tho, M. C., 2006, "Macroscopic-microscopic characterization of the passive mechanical properties in rat soleus muscle," J. Biomech., **39**(3), pp. 568–578.
[23] Grover, J. P., Corr, D. T., Toumi, H., Manthei, D. M., Oza, A. L., Vanderby, R., and Best, T. M., 2007, "The effect of stretch rate and activation state on skeletal muscle force in the anatomical range," Clin. Biomech., **22**(3), pp. 360–368.
[24] Best, T. M., McElhaney, J., Garrett, W. E., and Myers, B. S., 1994, "Characterization of the passive responses of live skeletal muscle using the quasi-linear theory of viscoelasticity," J. Biomech., **27**(4), pp. 413–419.
[25] Anderson, J., Li, Z., and Goubel, F., 2002, "Models of skeletal muscle to explain the increase in passive stiffness in desmin knockout muscle," J. Biomech., **35**(10), pp. 1315–1324.
[26] Gras, L. L., Mitton, D., Viot, P., and Laporte, S., 2013, "Viscoelastic properties of the human sternocleidomastoideus muscle of aged women in relaxation," J. Mech. Behav. Biomed. Mater., **27**, pp. 77–83.
[27] Gras, L.-L., Laporte, S., Viot, P., and Mitton, D., 2014, "Experimental characterization of post rigor mortis human muscle subjected to small tensile strains and application of a simple hyper-viscoelastic model.," Proc. Inst. Mech. Eng. H., **228**(10), pp. 1059–68.
[28] Odegard, G. M., Haut Donahue, T. L., Morrow, D. A., and Kaufman, K. R., 2008, "Constitutive modeling of skeletal muscle tissue with an explicit strain-energy function.," J. Biomech. Eng., **130**(6), p. 61017.
[29] Van Ee, C. A., Chasse, A. L., and Myers, B. S., 2000, "Quantifying skeletal muscle properties in cadaveric test specimens: effects of mechanical loading, postmortem time, and freezer storage.," J. Biomech. Eng., **122**(1), pp. 9–14.
[30] Abbott, B. C., and Lowy, J., 1956, "Stress relaxation in muscle.," Proc. R. Soc. Lond. B. Biol. Sci., **146**(923), pp. 281–288.
[31] Lieber, R. L., and Blevins, F. T., 1989, "Skeletal muscle architecture of the rabbit hindlimb: functional implications of muscle design.," J. Morphol., **199**(1), pp. 93–101.
[32] Shetye, S. S., Troyer, K. L., Streijger, F., Lee, J. H. T., Kwon, B. K., Cripton, P. A., and Puttlitz, C. M., 2014, "Nonlinear viscoelastic characterization of the porcine spinal cord," Acta Biomater., **10**(2), pp. 792–797.
[33] Maikos, J. T., Elias, R. A. I., and Shreiber, D. I., 2008, "Mechanical properties of dura

mater from the rat brain and spinal cord.," J. Neurotrauma, **25**(1), pp. 38–51.
[34] Ghoreishy, M. H. R., 2012, "Determination of the parameters of the Prony series in hyper-viscoelastic material models using the finite element method," Mater. Des., **35**, pp. 791–797.
[35] Troyer, K. L., Shetye, S. S., and Puttlitz, C. M., 2012, "Experimental Characterization and Finite Element Implementation of Soft Tissue Nonlinear Viscoelasticity," J. Biomech. Eng., **134**(11), p. 114501.
[36] Wheatley, B. B., Fischenich, K. M., Button, K. D., Haut, R. C., and Haut Donahue, T. L., 2015, "An optimized transversely isotropic, hyper-poro-viscoelastic finite element model of the meniscus to evaluate mechanical degradation following traumatic loading.," J. Biomech., **48**(8), pp. 1454–60.
[37] Kauer, M., Vuskovic, V., Dual, J., Szekely, G., and Bajka, M., 2002, "Inverse finite element characterization of soft tissues," Med. Image Anal., **6**(3), pp. 275–287.
[38] Lei, F., and Szeri, A. Z., 2007, "Inverse analysis of constitutive models: Biological soft tissues," J. Biomech., **40**(4), pp. 936–940.
[39] Holzapfel, G. A., 2000, Nonlinear Solid Mechanics, Wiley, Chichester, West Sussex, England.
[40] Morrow, D., Donahue, T., Odegard, G., and Kaufman, K., 2010, "A method for assessing the fit of a constitutive material model to experimental stress–strain data," Comput. Methods Biomech. Biomed. Engin., **13**(2), pp. 247–56.
[41] Robertson, D., and Cook, D., 2014, "Unrealistic statistics: How average constitutive coefficients can produce non-physical results.," J. Mech. Behav. Biomed. Mater., **40C**, pp. 234–239.
[42] Lu, Y. T., Zhu, H. X., Richmond, S., and Middleton, J., 2010, "A visco-hyperelastic model for skeletal muscle tissue under high strain rates," J. Biomech., **43**(13), pp. 2629–2632.
[43] Light, N., and Champion, A. E., 1984, "Characterization of muscle epimysium, perimysium and endomysium collagens.," Biochem. J., **219**(3), pp. 1017–1026.
[44] Listrat, A., Lethias, C., Hocquette, J. F., Renand, G., Menissier, F., Geay, Y., and Picard, B., 2000, "Age-related changes and location of types I, III, XII and XIV collagen during development of skeletal muscles from genetically different animals," Histochem. J., **32**(6), pp. 349–356.
[45] Lieber, R. L., Runesson, E., Einarsson, F., and Fridén, J., 2003, "Inferior mechanical properties of spastic muscle bundles due to hypertrophic but compromised extracellular matrix material," Muscle and Nerve, **28**(4), pp. 464–471.
[46] Zhu, W., Chern, K. Y., and Mow, V. C., 1994, "Anisotropic viscoelastic shear properties of bovine meniscus.," Clin. Orthop. Relat. Res., (306), pp. 34–45.
[47] Li, L. P., Herzog, W., Korhonen, R. K., and Jurvelin, J. S., 2005, "The role of viscoelasticity of collagen fibers in articular cartilage: Axial tension versus compression," Med. Eng. Phys., **27**(1), pp. 51–57.
[48] Troyer, K. L., and Puttlitz, C. M., 2011, "Human cervical spine ligaments exhibit fully nonlinear viscoelastic behavior," Acta Biomater., **7**(2), pp. 700–709.
[49] Salisbury, C., Cronin, D., and Lien, F.-S., 2015, "Deformation Mechanics of a Non-linear Hyper-viscoelastic Porous Material, Part I: Testing and Constitutive Modeling of Non-porous Polychloroprene," J. Dyn. Behav. Mater., **1**(3), pp. 237–248.
[50] Sandino, C., McErlain, D. D., Schipilow, J., and Boyd, S. K., 2015, "The poro-viscoelastic

properties of trabecular bone: a micro computed tomography-based finite element study.," J. Mech. Behav. Biomed. Mater., **44**, pp. 1–9.
[51] Chang, C.-T., Chen, Y.-H., Lin, C.-C. K., and Ju, M.-S., 2015, "Finite element modeling of Hyper-viscoelasticity of peripheral nerve Ultrastructures," J. Biomech.
[52] Lieber, R. L., 2010, Skeletal Muscle Structure, Function, and Plasticity, Lippincott Williams and Wilkins, Philadelphia, PA.
[53] Ahamed, T., Rubin, M. B., Trimmer, B. A., and Dorfmann, L., 2015, "Time-dependent behavior of passive skeletal muscle," Contin. Mech. Thermodyn., **27**.

CHAPTER 3:

HOW DOES TISSUE PREPARATION AFFECT SKELETAL MUSCLE TRANSVERSE ISOTROPY?

3.1 Introduction

The human body relies on skeletal muscle, supported by other orthopaedic tissues, for locomotion and posture. Passive properties of muscle are governed by two components of the tissue: the protein titin at the sarcomere level which gives muscle fibers passive stiffness [1,2], and the collagen rich extracellular matrix which organizes muscle fibers in a hierarchical structure and dominates passive stiffness at the tissue level [3,4]. In the case of skeletal muscle these passive properties have a multifaceted purpose: allowing for the transmission of internal force generated at muscle fibers to tendons [5,6], storing energy during locomotion [7,8], and maintaining proper resting length for maximum force generation [9]. Muscle fiber alignment results in tissue transverse isotropy [10–13] as the material properties of the aligned fibers differ from those of the organized extracellular matrix [3].

Finite element analyses of biological soft tissues provide important insight into tissue behavior for clinical recommendations and observations. However, inaccurate constitutive models could present erroneous data, thus hampering clinical relevance. Some modeling studies of passive skeletal muscle assume the longitudinal direction is stiffer than the transverse direction [14–17]. While this is supported by some experimental work [11], there is also data which identifies a

This chapter has been published as a Short Communication in the Journal of Biomechanics (49, 12, 2016). All content has been adapted with permission from Elsevier.

stiffer transverse response as compared to the longitudinal direction [10,18]. These differences may be the result of disparities in experimental protocol and anatomical or species variations, although they are more likely the result of rigor mortis, which results in a stiffening of the tissue [13,19]. As rigor mortis is a complex phenomenon related to the actin-myosin complex [20,21], it most likely influences the longitudinal mechanics to a greater extent than in the transverse direction. Thus, it is hypothesized that the large observed differences in passive transversely isotropic skeletal muscle behavior is a function of non-fresh testing conditions and/or experimental protocol. Data supporting this hypothesis would provide two important recommendations for future studies of skeletal muscle: 1) all mechanical testing should be conducted on fresh, never frozen tissue, and 2) computational models of passively stretched muscle should reflect the true transverse isotropy in that the longitudinal direction is less stiff than the transverse direction.

The goals of this work were thus to evaluate the effects of orientation and post mortem handling on the material properties of skeletal muscle. Specifically, we aim to answer the question: "How does tissue preparation affect the transversely isotropic stiffness and time dependence of skeletal muscle?"

3.2 Methods

Six Giant Flemish Rabbits were obtained with Colorado State University Institutional Animal Care and Use Committee approval. Following euthanasia, whole tibialis anterior muscles were isolated from each hind limb and stored in a refrigerator for either fresh testing (left or right limb randomly) or to allow for the onset of rigor mortis (contralateral limb). As rigor mortis begins 6-

8 hours post mortem [13,19] fresh muscles were tested within four hours to reduce these effects, while the contralateral muscle was subject to non-fresh testing following a freeze-thaw cycle (Figure 3-1A). Each tibialis anterior yielded two samples, one longitudinal, and one transverse (Figure 3-1B). As the pennation angle of the New Zealand White Rabbit is very low (Lieber and Blevins, 1989), the longitudinal direction was assumed to be parallel with the axis of force transmission.

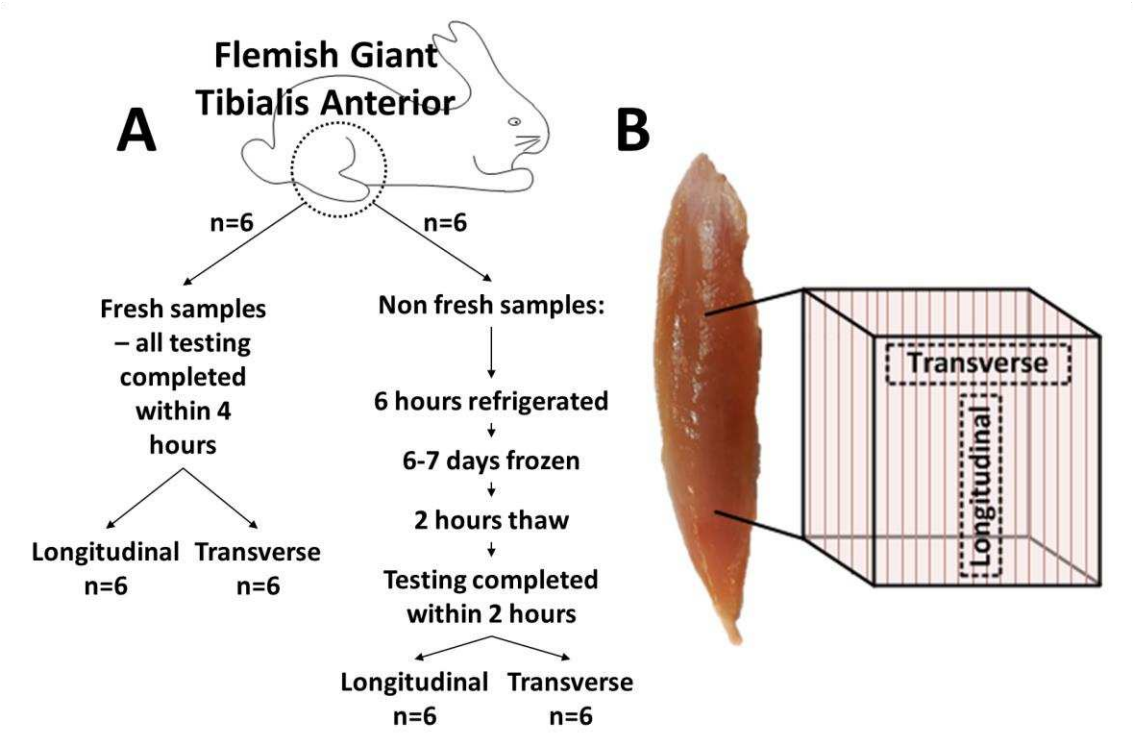

Figure 3-1: (A) Specimen groupings and testing timeline, showing the fresh testing group and the group subject to non-fresh conditions and a freeze/thaw cycle. Each of these groups yielded longitudinal and transverse samples for a total of four groups. (B) Dissection orientations show that each muscle yielded two samples, one in the longitudinal direction and one in the transverse direction.

Tensile tests were conducted on a servo hydraulic material test system (MTS, Eden Prairie, MN). Cross sectional area and gauge length were measured optically with a 1.4 megapixel monochrome camera and ImageJ software (National Institutes of Health, Bethesda, MD). Graphite powder was used to track strain with digital image correlation (DIC) software (Matlab,

Mathworks, Natick, MA) on a region of interest (ROI) (Figure 3-2A). Samples were obtained from the muscle midbelly such that they were free of aponeurosis, tendon, and epimysium. A custom fabricated drop cutter with high profile histology blades spaced 4mm apart was used to slice samples into ~16 mm^2 cross section (Table 3-1). To ensure no dimensional differences occurred between longitudinal and transverse samples which could potentially influence sample behavior, paired equivalence tests were performed. These tests evaluated whether or not the mean cross sectional area or mean gauge length was superior for either longitudinal or transverse samples compared to the other group ($p<0.05$). The results showed that superiority was not established for either group (longitudinal nor transverse) for both cross sectional area and gauge length ($p>0.05$ for all tests).

Table 3-1: Specimen dimensions (mean and standard deviation in parenthesis) for longitudinal and transverse samples.

Sample Direction	Cross Sectional Area (mm^2)	Gauge Length (mm)
Longitudinal	17.25 (2.75)	18.14 (3.24)
Transverse	15.93 (1.71)	17.70 (1.51)

Tensile tests were conducted with a 9 N load cell (Futek, Irvine, CA). A pair of thin film grips was utilized to clamp all specimens to reduce grip slippage (Figure 3-2A). Specimen width and thickness were measured with image analysis at three locations along the length of each sample, while gauge length was measured as the grip to grip distance following a 0.1 N pre-load (Figure 3-2A). Specimens were kept moist during testing with phosphate buffered saline (PBS) spray [10,11]. All specimens underwent an initial ramp phase of 10% strain at 10% $second^{-1}$ followed by 300 seconds of relaxation and finally a constant ramp pull at 1% $second^{-1}$ until specimen failure (Figure 3-2B). Cauchy (true) stress and Euler strain were converted from force-

displacement data and used to calculate tangent moduli. Data were smoothed with a third order Savitsky-Golay filter to reduce noise [22]. The Cauchy (true) axial stress component associated with loading direction (σ) was calculated using Equation 1 [23], where P is first corresponding Piola-Kirchoff (engineering) stress component and l and l_o are the deformed and initial specimen lengths, respectively. The mechanical correlate to the Cauchy stress is Euler strain. The axial component of the Euler strain associated with the loading direction (e) is given in Equation 2. Tangent moduli (E) were calculated according to Equation 3.

$$\sigma = P\frac{l}{l_o} \tag{1}$$

$$e = \frac{1}{2}\left[1 - \left(\frac{l_o}{l}\right)^2\right] \tag{2}$$

$$E = \frac{\sigma}{e} \tag{3}$$

Tangent moduli were calculated at the initial peak, end of the relaxation phase, and at 20% strain, which is the higher end of the physiological range for the rabbit tibialis anterior [24,25]. Relaxation ratio was calculated as the fraction of stress relaxation over three separate time periods following the initial ramp: 0-5 seconds, 5-50 seconds, and 50-300 seconds. The raw relaxation data were fitted to a power law equation (Equation 1, where σ is Cauchy stress, t is relaxation time, and a and b are constants which characterize the relative stress level and rate of relaxation, respectively) for identification of relaxation rate.

$$\sigma = at^b \tag{4}$$

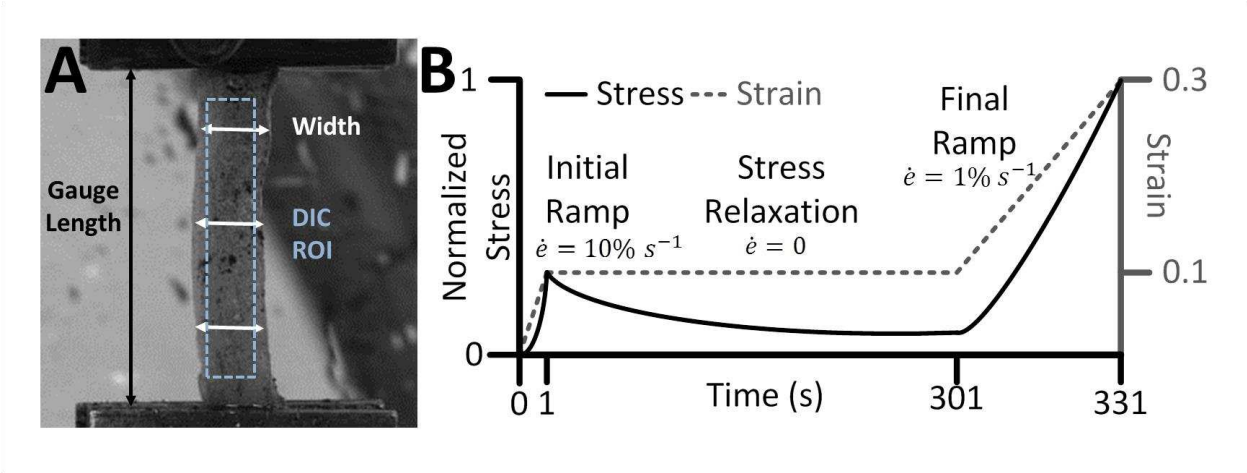

Figure 3-2: Specimen testing procedures. A: Experimental setup showing speckled sample with gauge length (black arrow), three width measurement locations (white arrows), and digital image correlation region of interest (DIC ROI – light blue dotted box). B: Testing outline (not to scale) highlighting initial ramp phase, relaxation phase, and final ramp phase to failure (strain of 0.3 given as an example), with representative stress shown as solid black line and strain in dotted gray line.

Mean and standard deviations for all data were calculated, including raw stress-strain and stress-time data as well as moduli, relaxation ratios, and power law b terms (Equation 1). A one-way ANOVA was performed with a Tukey's post-hoc analysis ($p<0.05$) to identify differences in moduli, relaxation ratios, and power law b parameter across all four groups.To identify the ability of the power law equation (Equation 1) to fit the relaxation data, the normalized root mean square error (NRMSE) was calculated for each specimen (Equation 5, where N is the total number of data points, x are the experimental data and y are the model data from Equation 1).

$$NRMSE = \frac{\sqrt{\sum_{i=1}^{N}(x_i - y_i)^2}}{N\bar{x}} \tag{5}$$

3.3 Results

All data passed the Anderson-Darling normality test ($p>0.05$), suggesting the data were normally distributed. This supported the use of an ANOVA to identify statistical differences between groups. Visual inspection of raw data and calculated moduli values show the peak modulus for longitudinal fresh samples is lower than all other groups ($p=0.044$, $p<0.0005$, and $p=0.014$ for transverse fresh, longitudinal rigor, and transverse rigor, respectively), while longitudinal rigor is higher than both transverse groups ($p=0.008$, $p=0.027$ for transverse fresh and rigor, respectively) (Figure 3-3A and 3C). Equilibrium moduli for longitudinal fresh was lower than all other groups ($p=0.006$, $p=0.004$, and $p=0.001$ for transverse fresh, longitudinal rigor, and transverse rigor, respectively), while values calculated at 20% strain during the constant rate phase again showed the longitudinal fresh group was lower than all other groups ($p=0.001$, $p=0.004$, $p=0.015$ for transverse fresh, longitudinal rigor, and transverse rigor, respectively) (Figure 3-3). The longitudinal fresh samples showed a highly nonlinear shape compared to the other groups (Figure 3-3B).

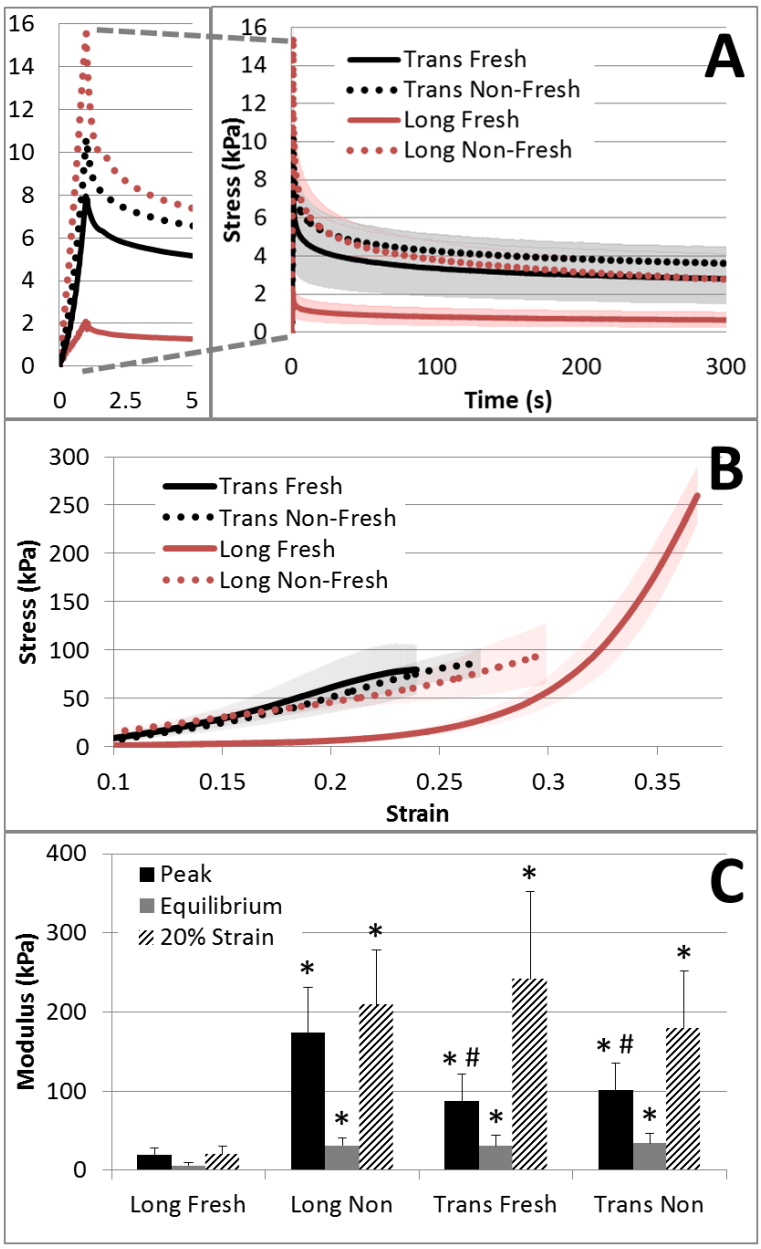

Figure 3-3. (A) Raw data results showing stress relaxation step stress-time data with standard deviation. The loading phase and initial relaxation are highlighted for clarity on left with no standard deviation. (B) Quasi-static testing stress-strain data with standard deviation. (C) Moduli values with standard deviation for all four groups at the peak of the stress relaxation step, at equilibrium of the stress relaxation step, and at 20% strain of the quasi-static testing phase (* denotes statistically different from longitudinal fresh samples and # denotes different from longitudinal non-fresh samples, $p<0.05$).

Longitudinal rigor samples showed faster initial relaxation rate visually, as characterized by the power law *b* coefficient ($p=0.017$, $p<0.0005$, and $p<0.0005$ for transverse fresh, longitudinal

rigor, and transverse rigor, respectively), and when comparing the initial relaxation phase (0-5 seconds, $p=0.029$, $p<0.0005$, and $p<0.0005$ for transverse fresh, longitudinal rigor, and transverse rigor, respectively) (Figure 3-4). The power law equation was able to fit the relaxation data very well, with a mean NRMSE value of 1.16E-2% and a standard deviation of 6.0E-3% for all samples.

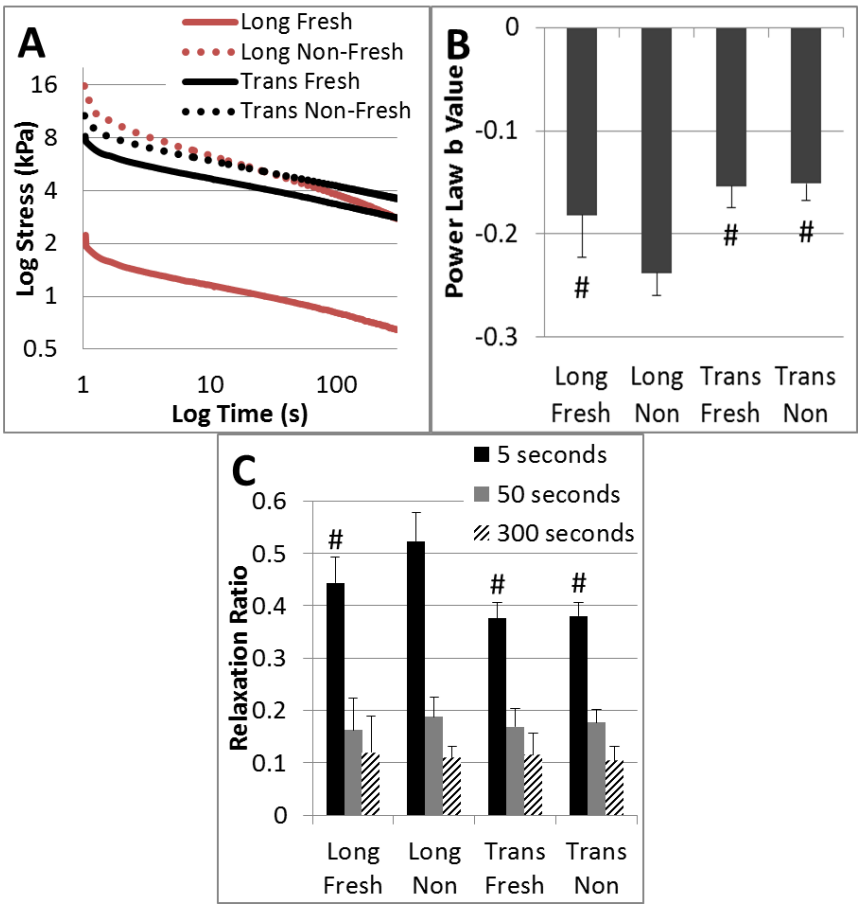

Figure 3-4. (A) Logarithmic plot of the mean relaxation behavior for the four experimental groups. (B) Mean and standard deviation power law *b* values for all four groups (# denotes significantly different than longitudinal non-fresh samples, $p<0.05$). (C) Mean and standard deviation relaxation ratio for all four groups between 0-5 seconds, 5-50 seconds, and 50-300 seconds (# denotes significantly different than longitudinal non-fresh samples, $p<0.05$).

3.4 Discussion

The increased tangent moduli values and increase in relaxation rate of longitudinal non-fresh samples show that post mortem handling plays a key role in the alteration of muscle mechanical

properties, which agrees well with previous experimental data on muscle properties as a function of rigor mortis [19]. However, it remains unclear how the mechanical properties of skeletal muscle are affected separately by rigor mortis and a freeze/thaw cycle. To the authors knowledge this work represents the first investigation of both transverse isotropy and time dependence of skeletal muscle as a function of post mortem handling. As rigor mortis is a complex biochemical phenomenon [20,21], it remains unclear exactly which mechanisms are contributing to these particular results. While this study employed a relatively small sample size (n=6), the statistical significance and observable differences were quite clear despite the sample number.

While skeletal muscle tensile studies are common [10,11,15,22,26,27], separate investigations have determined the tissue to be stiffer in the longitudinal direction [11] or the transverse direction [10]. Our data for fresh samples agree well with Takaza et al for both transverse isotropy (transverse stiffer than longitudinal) and in terms of general stress-strain shape (longitudinal is nonlinear, transverse appears linear). Takaza et al show higher stress values at similar strain levels when compared to our data, as they reported ~100 kPa versus ~50 kPa reported here at 30% strain for longitudinal fresh samples and ~110 kPa versus ~25 kPa for transverse samples at 15% strain. However, this may be due to variations in species, anatomy, or experimental protocol, as stress values at the end of the relaxation phase from the data presented here were very low (<4 kPa) and Takaza et al did not incorporate a relaxation phase. Data from Morrow et al appears more linear in the longitudinal direction, which agrees fairly well with our longitudinal rigor samples, but is again stiffer than our samples. Unfortunately there is poor agreement between transverse samples, as Morrow et al found the transverse direction to be less stiff and more extensible (~60 kPa at 25% strain here vs ~25 kPa at 100% strain).

The observed differences between the data presented here and Morrow et al may be due to four main disparities in experimental protocol. The first is the freeze/thaw timing post mortem, which was done quickly by Morrow et al and after six hours of refrigeration as presented above. Despite the best efforts of Morrow et al to minimize the effects of rigor mortis, the true extent of post mortem stiffening to those samples remains unknown. The delayed freezing for our samples was done to ensure the onset of rigor mortis affected muscle samples [13,19]. Secondly, Morrow et al utilized whole muscle samples with the epimysium and aponeurosis removed, which may have led to a smaller aspect ratio for transverse samples compared to the aspect ratio of our samples at roughly 4:1 (Table 3-1). Additionally, our tests utilized a relaxation period during which longitudinal samples decreased from a higher stress level than all other samples at a faster rate, while Morrow et al performed a single ramp test. Finally, Morrow et al studied the extensor digitorum longus, which has a higher pennation angle and a shorter fiber length than the tibialis anterior [28], which may influence the apparent transverse isotropy of the tissue. To identify possible causes for these discrepancies, further experimental work should be performed under carefully controlled conditions. Specifically, these tests should identify transversely isotropic modulus values of skeletal muscle under various freeze/thaw times post mortem and as a function of different specimen aspect ratios. Also, performing these tests on a single tissue would greatly reduce variability which may result from anatomical differences.

The data presented here can be utilized to improve constitutive modeling efforts of skeletal muscle, as some studies in the past have assumed muscle is stiffer in the longitudinal direction [14–17]. Future studies should model muscle as stiffer in the transverse direction similar to other works [29–32].

3.5 Conclusions

The transversely isotropic mechanical properties of skeletal muscle were evaluated with a specific focus on post mortem handling. While it remains unclear exactly how a non-fresh conditions and a freeze/thaw cycle independently affect the tensile transverse isotropy of skeletal muscle, to prevent any alterations in mechanical properties muscle tissue should be tested prior to the onset of rigor mortis without a freeze/thaw cycle. These data should be utilized to improve future modeling efforts for skeletal muscle with a specific focus on the anisotropic constitutive formulation.

REFERENCES

[1] Tskhovrebova, L., and Trinick, J., 2002, "Role of titin in vertebrate striated muscle.," Philos. Trans. R. Soc. Lond. B. Biol. Sci., **357**(1418), pp. 199–206.

[2] Magid, A., and Law, D. J., 1985, "Myofibrils bear most of the resting tension in frog skeletal muscle.," Science, **230**(4731), pp. 1280–2.

[3] Meyer, G. A., and Lieber, R. L., 2011, "Elucidation of extracellular matrix mechanics from muscle fibers and fiber bundles," J. Biomech., **44**(4), pp. 771–773.

[4] Brown, S. H. M., Carr, J. A., Ward, S. R., and Lieber, R. L., 2012, "Passive mechanical properties of rat abdominal wall muscles suggest an important role of the extracellular connective tissue matrix," J. Orthop. Res., **30**(8), pp. 1321–1326.

[5] Gindre, J., Takaza, M., Moerman, K. M., and Simms, C. K., 2013, "A structural model of passive skeletal muscle shows two reinforcement processes in resisting deformation.," J. Mech. Behav. Biomed. Mater., **22**, pp. 84–94.

[6] Huijing, P. A., 1999, "Muscle as a collagen fiber reinforced composite: A review of force transmission in muscle and whole limb," J. Biomech., **32**(4), pp. 329–345.

[7] Ettema, G. J., 1996, "Mechanical efficiency and efficiency of storage and release of series elastic energy in skeletal muscle during stretch-shorten cycles.," J. Exp. Biol., **199**(Pt 9), pp. 1983–97.

[8] Cavanagh, P. R., and Komi, P. V., 1979, "Electromechanical delay in human skeletal muscle under concentric and eccentric contractions," Eur. J. Appl. Physiol. Occup. Physiol., **42**(3), pp. 159–163.

[9] Fridén, J., and Lieber, R. L., 1998, "Evidence for muscle attachment at relatively long lengths in tendon transfer surgery.," J. Hand Surg. Am., **23**(1), pp. 105–110.

[10] Takaza, M., Moerman, K. M., Gindre, J., Lyons, G., and Simms, C. K., 2012, "The anisotropic mechanical behaviour of passive skeletal muscle tissue subjected to large tensile strain," J. Mech. Behav. Biomed. Mater., **17**, pp. 209–220.

[11] Morrow, D. A., Haut Donahue, T. L., Odegard, G. M., and Kaufman, K. R., 2010, "Transversely isotropic tensile material properties of skeletal muscle tissue," J. Mech. Behav. Biomed. Mater., **3**(1), pp. 124–129.

[12] Pietsch, R., Wheatley, B. B., Haut Donahue, T. L., Gilbrech, R., Prabhu, R., Liao, J., and Williams, L. N., 2014, "Anisotropic compressive properties of passive porcine muscle tissue.," J. Biomech. Eng., **136**(11), p. 111003.

[13] Van Loocke, M., Lyons, C. G., and Simms, C. K., 2006, "A validated model of passive muscle in compression," J. Biomech., **39**(16), pp. 2999–3009.

[14] Lu, Y. T., Zhu, H. X., Richmond, S., and Middleton, J., 2010, "A visco-hyperelastic model for skeletal muscle tissue under high strain rates," J. Biomech., **43**(13), pp. 2629–2632.

[15] Calvo, B., Ramírez, A., Alonso, A., Grasa, J., Soteras, F., Osta, R., and Muñoz, M. J., 2010, "Passive nonlinear elastic behaviour of skeletal muscle: Experimental results and model formulation," J. Biomech., **43**(2), pp. 318–325.

[16] Grasa, J., Ramírez, a, Osta, R., Muñoz, M. J., Soteras, F., and Calvo, B., 2011, "A 3D active-passive numerical skeletal muscle model incorporating initial tissue strains.

Validation with experimental results on rat tibialis anterior muscle.," Biomech. Model. Mechanobiol., **10**(5), pp. 779–87.
[17] Hernández-Gascón, B., Grasa, J., Calvo, B., and Rodríguez, J. F., 2013, "A 3D electro-mechanical continuum model for simulating skeletal muscle contraction.," J. Theor. Biol., **335**, pp. 108–18.
[18] Nie, X., Cheng, J.-I., Chen, W. W., and Weerasooriya, T., 2011, "Dynamic Tensile Response of Porcine Muscle," J. Appl. Mech., **78**(2), p. 21009.
[19] Van Ee, C. A., Chasse, A. L., and Myers, B. S., 2000, "Quantifying skeletal muscle properties in cadaveric test specimens: effects of mechanical loading, postmortem time, and freezer storage.," J. Biomech. Eng., **122**(1), pp. 9–14.
[20] Huff Lonergan, E., Zhang, W., and Lonergan, S. M., 2010, "Biochemistry of postmortem muscle - lessons on mechanisms of meat tenderization.," Meat Sci., **86**(1), pp. 184–95.
[21] Roth, B., Slinde, E., and Arildsen, J., 2006, "Pre or post mortem muscle activity in Atlantic salmon (Salmo salar). The effect on rigor mortis and the physical properties of flesh," Aquaculture, **257**(1–4), pp. 504–510.
[22] Wheatley, B. B., Morrow, D. A., Odegard, G. M., Kaufman, K. R., and Haut Donahue, T. L., 2016, "Skeletal muscle tensile strain dependence: Hyperviscoelastic nonlinearity.," J. Mech. Behav. Biomed. Mater., **53**, pp. 445–54.
[23] Holzapfel, G. A., 2000, Nonlinear Solid Mechanics, Wiley, Chichester, West Sussex, England.
[24] Winters, T. M., Sepulveda, G. S., Cottler, P. S., Kaufman, K. R., Lieber, R. L., and Ward, S. R., 2009, "Correlation between isometric force and intramuscular pressure in rabbit tibialis anterior muscle with an intact anterior compartment," Muscle and Nerve, **40**(1), pp. 79–85.
[25] Davis, J., Kaufman, K. R., and Lieber, R. L., 2003, "Correlation between active and passive isometric force and intramuscular pressure in the isolated rabbit tibialis anterior muscle," J. Biomech., **36**(4), pp. 505–512.
[26] Abraham, A. C., Kaufman, K. R., and Haut Donahue, T. L., 2012, "Phenomenological consequences of sectioning and bathing on passive muscle mechanics of the New Zealand white rabbit tibialis anterior," J. Mech. Behav. Biomed. Mater., **17**, pp. 290–295.
[27] Gras, L. L., Mitton, D., Viot, P., and Laporte, S., 2012, "Hyper-elastic properties of the human sternocleidomastoideus muscle in tension," J. Mech. Behav. Biomed. Mater., **15**, pp. 131–140.
[28] Lieber, R. L., and Blevins, F. T., 1989, "Skeletal muscle architecture of the rabbit hindlimb: functional implications of muscle design.," J. Morphol., **199**(1), pp. 93–101.
[29] Blemker, S. S., Pinsky, P. M., and Delp, S. L., 2005, "A 3D model of muscle reveals the causes of nonuniform strains in the biceps brachii.," J. Biomech., **38**(4), pp. 657–65.
[30] Odegard, G. M., Haut Donahue, T. L., Morrow, D. A., and Kaufman, K. R., 2008, "Constitutive modeling of skeletal muscle tissue with an explicit strain-energy function.," J. Biomech. Eng., **130**(6), p. 61017.
[31] Jenkyn, T., Koopman, B., Huijing, P. a, Lieber, R. L., and Kaufman, K. R., 2002, "Finite element model of intramuscular pressure during isometric contraction of skeletal muscle.," Phys. Med. Biol., **47**, pp. 4043–4061.
[32] Yucesoy, C. A., Koopman, B. H. F. J. M., Huijing, P. A., and Grootenboer, H. J., 2002, "Three-dimensional finite element modeling of skeletal muscle using a two-domain approach: linked fiber-matrix mesh model.," J. Biomech., **35**(9), pp. 1253–62.

CHAPTER 4:

A CASE FOR POROELASTICITY IN SKELETAL MUSCLE FINITE ELEMENT ANALYSIS: EXPERIMENT AND MODELING

4.1 Introduction

In addition to muscle fibers and extracellular matrix, skeletal muscle consists of approximately 75% fluid [1]. Thus, it can be characterized as a biphasic material, consisting of both a solid and a fluid phase. Other biphasic biological tissues such as cartilage [2] and meniscus [3] utilize fluid content to distribute under loads compression. However, the biphasic properties of muscle, specifically permeability, are not known. The role which permeability plays in skeletal muscle mechanics, known as poroelasticity, is unclear [4]. In computational models of skeletal muscle, time dependence is often neglected [5] or approximated using viscoelastic modeling [6,7]. The goals of this work were to 1) characterize skeletal muscle permeability by direct experimental measurement, and 2) identify how various permeability implementations affect skeletal muscle models in compression.

4.2 Methods

Four New Zealand White Rabbits ~2.5 kg in weight, were euthanized with Colorado State University Institutional Animal Care and Use Committee approval. One biceps femoris muscle from each animal was harvested from the left or right hind limb. All procedures were completed

This chapter has been published as a Rapid Innovative Communication in Computer Methods in Biomechanics and Biomedical Engineering (2016). All content has been adapted with permission from Taylor & Francis.

within 6 hours post mortem to reduce the effects of rigor mortis [5]. Cylindrical samples (4 mm height and 8 mm diameter) were removed from the muscle mid-belly using a drop cutter and a biopsy punch. As skeletal muscle exhibits transversely isotropic passive behavior [8,9], samples were obtained in the longitudinal and the transverse directions.

The permeability of each sample was directly evaluated using a permeation test device similar to previously published work [10]. In short, this device applied a known flow rate (0.5 mL/min) with a syringe pump to phosphate buffered saline across a tissue sample while measuring the pressure difference across the sample (Figure 4-1A). Additionally, since permeability is typically a function of tissue strain [10], samples were compressed axially (12.5% and 25%) to replicate transverse or longitudinal compression or compressed laterally (25% and 50%) to simulate longitudinal stretch (Figure 4-1B-D). Pressure (P), flow rate (Q), specimen dimensions (L_0 and A), and strain (ε) were measured to calculate the permeability of the tissue [10] (Equation 1). A paired t-test was utilized to compare permeability values between longitudinal and transverse samples and a general linear model was utilized to determine if permeability varied with strain level ($p<0.05$ for both analyses).

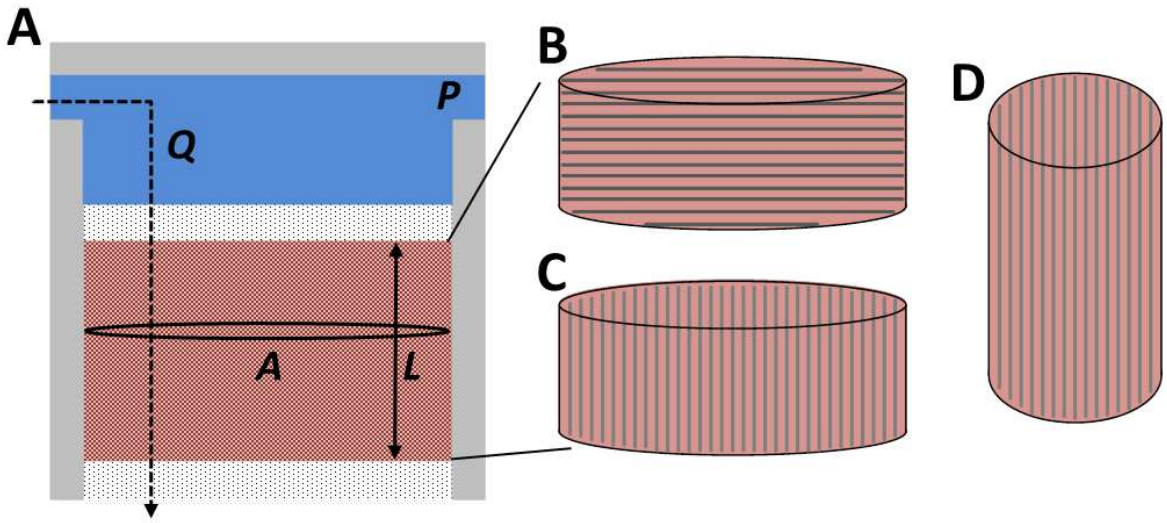

Figure 4-1. A) Permeability testing apparatus, where fluid (blue) at a pressurized level P passes through the specimen (red) at a flow rate Q, across an area A, and along a length $L = L_0(1 + \varepsilon)$. B-D) Specimens were compressed axially to simulate B) transverse and C) longitudinal compression or laterally to simulate D) longitudinal tension.

$$k = \frac{QL_0(1+\varepsilon)}{AP} \tag{1}$$

A 3D finite element (FE) model representing midbelly muscle tissue was developed using FEBio (febio.org) with 270 hexahedron elements. This model simulated a 4x4x20 mm cuboid using two planes of symmetry and had muscle fibers aligned parallel to the length of the cuboid. The cuboid was compressed in the transverse direction under stress relaxation (20% strain at 10% second^{-1} followed by a 300 second relaxation) before compression to 50% strain at 1% second^{-1}. A poroelastic ellipsoidal fiber reinforced coupled (compressible) Mooney-Rivlin constitutive model was implemented. Strain-dependent permeability was implemented as a function of the volume ratio J, the undeformed void ratio φ_0 (0.19 for skeletal muscle [1]), and material properties k_0, M, and α (Equation 2) [10].

$$k(J) = k_0 \left(\frac{J-\varphi_0}{1-\varphi_0}\right)^{\alpha} \exp\left[\frac{M}{2}(J^2 - 1)\right] \tag{2}$$

To study how various permeability assumptions affects model behavior, four separate formulations were utilized in separate simulations: a solid analysis only as a baseline ("Solid"), a constant, isotropic permeability for a simple biphasic model ("Constant"), and two separate fits of Equation 2 to experimental data to generate anisotropic and strain dependent responses ("Fit I" and "Fit II") (Table 4-1). Fit I was a conservative strain dependent formulation while Fit II was a case of highly nonlinear strain dependence similar to other tissues [10]. Additionally, the "Constant" model was compared against two models incorporating viscoelasticity of the solid phase through a Prony series [7], one with both poroelasticity and viscoelasticity, and one with viscoelasticity only. The mean Cauchy stress in the direction of compression was compared between models.

Table 4-1. Parameter values for the three utilized permeability formulations.

Permeability Model	**k_0 (m^4/N-s) E-11**		**M (-)**		**α (-)**	
	Long	**Trans**	**Long**	**Trans**	**Long**	**Trans**
Isotropic Constant	7.41		N/A	N/A	N/A	N/A
Fit I	11	4.2	0.63	0.16	0.1	0.97
Fit II	50	5	10	1	2	1.5

4.3 Results

The mean permeability value for all samples was 7.41×10^{-11} m^4/N-s with a standard error of 2.2×10^{-11} m^4/N-s. There was no statistical effect of either strain level ($p=0.398$) or orientation ($p=0.158$) on skeletal muscle permeability (Figure 4-2A-B).

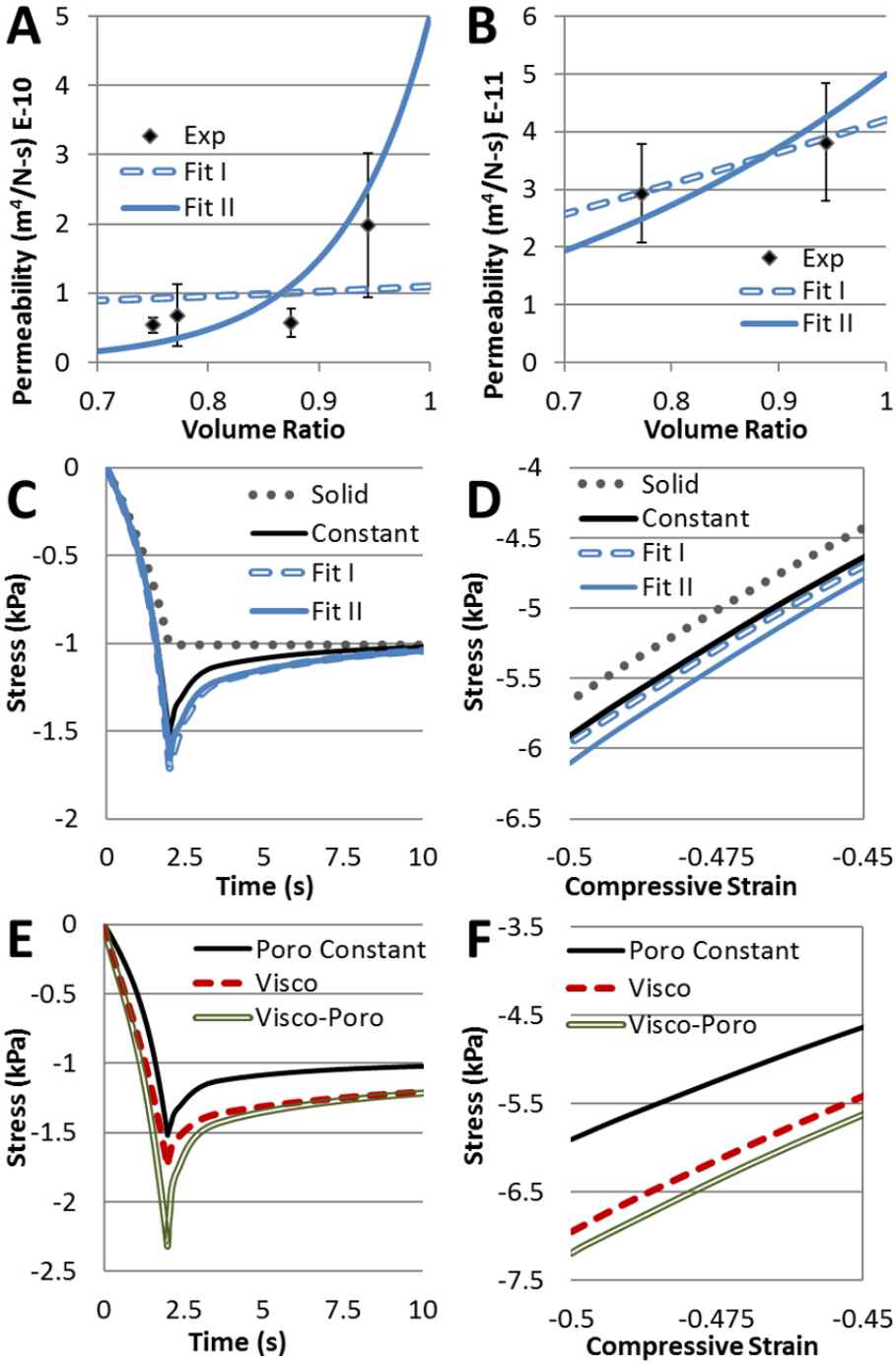

Figure 4-2. Experimental permeability raw data (± standard error of the mean), Fit I, and Fit II curves for A) longitudinal samples and B) transverse samples. Cauchy stress outputs for the various biphasic analyses for C) initial 20% compression ramp and relaxation and D) 45-50% compression and for the viscoelastic comparisons for E) initial 20% compression ramp and relaxation and F) 45-50% compression.

Table 4-2. Mean Cauchy stress values for all analyses at compressive strains of 20% (peak response) and 50%.

Mean Cauchy Stress in kPa	Solid	Constant	Fit I	Fit II	Visco Only	Visco-Poro
20% Strain Peak	-1.01	-1.52	-1.71	-1.66	-1.74	-2.32
50% Strain	-5.66	-5.91	-5.96	-6.10	-6.95	-7.19

Utilizing a biphasic approach affected tissue behavior particularly under transient conditions (Figure 4-2C-D and Table 4-2), while variations in strain dependence and anisotropy played less of a role than poroelasticity itself. A combined visco-poroelastic model differed drastically from all other analyses, including the viscoelastic only model (Figure 4-2E-F and Table 4-2).

4.4 Discussion

This work provides, to the authors' best knowledge, the first direct measurement of skeletal muscle permeability. The observed values from this work show an increase of 4-5 orders of magnitude over other biological tissues such as cartilage or ligament [2,10]. This is not surprising since low muscle permeability would greatly resist muscle deformation, thus reducing contractile capabilities.

Model calculated stresses had good agreement with previously published experimental work under compression [5,8] which gives greater confidence in these results. Statistical results showed no dependence of permeability on strain level or orientation, while modeling results indicated strain and orientation dependence played less of a role than even a simple poroelastic model versus a solid model. Additionally, the viscoelastic comparison data suggest viscoelasticity alone may not always be appropriate for skeletal muscle modeling in

compression. Thus, a simple biphasic analysis (isotropic, constant permeability) combined with viscoelasticity could be appropriately utilized for skeletal muscle models involving highly transient compressive conditions such as impact.

REFERENCES

[1] Sjøgaard, G., and Saltin, B., 1982, "Extra- and intracellular water spaces in muscles of man at rest and with dynamic exercise.," Am. J. Physiol., **243**(3), pp. R271-80.

[2] Mansour, J. M., and Mow, V. C., 1976, "The permeability of articular cartilage under compressive strain and at high pressures.," J. Bone Joint Surg. Am., **58**(4), pp. 509–16.

[3] LeRoux, M. A., and Setton, L. A., 2002, "Experimental and biphasic FEM determinations of the material properties and hydraulic permeability of the meniscus in tension.," J. Biomech. Eng., **124**(3), pp. 315–21.

[4] Yang, M., and Taber, L. A., 1991, "The possible role of poroelasticity in the apparent viscoelastic behavior of passive cardiac muscle.," J. Biomech., **24**(7), pp. 587–97.

[5] Van Loocke, M., Lyons, C. G., and Simms, C. K., 2006, "A validated model of passive muscle in compression," J. Biomech., **39**(16), pp. 2999–3009.

[6] Van Loocke, M., Lyons, C. G., and Simms, C. K., 2008, "Viscoelastic properties of passive skeletal muscle in compression: Stress-relaxation behaviour and constitutive modelling," J. Biomech., **41**(7), pp. 1555–1566.

[7] Wheatley, B. B., Pietsch, R. B., Haut Donahue, T. L., and Williams, L. N., 2016, "Fully non-linear hyper-viscoelastic modeling of skeletal muscle in compression.," Comput. Methods Biomech. Biomed. Engin., **19**(11), pp. 1181–9.

[8] Pietsch, R., Wheatley, B. B., Haut Donahue, T. L., Gilbrech, R., Prabhu, R., Liao, J., and Williams, L. N., 2014, "Anisotropic compressive properties of passive porcine muscle tissue.," J. Biomech. Eng., **136**(11), p. 111003.

[9] Takaza, M., Moerman, K. M., Gindre, J., Lyons, G., and Simms, C. K., 2012, "The anisotropic mechanical behaviour of passive skeletal muscle tissue subjected to large tensile strain," J. Mech. Behav. Biomed. Mater., **17**, pp. 209–220.

[10] Weiss, J. a, and Maakestad, B. J., 2006, "Permeability of human medial collateral ligament in compression transverse to the collagen fiber direction.," J. Biomech., **39**(2), pp. 276–83.

CHAPTER 5:

A VALIDATED MODEL OF PASSIVE SKELETAL MUSCLE TO PREDICT FORCE AND INTRAMUSCULAR PRESSURE

5.1 Introduction

Skeletal muscle, which composes roughly one third of the human body by mass [1], provides locomotion and maintains posture. The well-known force-length relationship of skeletal muscle dictates *in vivo* muscle function under a wide range of conditions [2]. Maintaining appropriate muscle resting length is a concern for surgeries involving detachment and reattachment such as a tendon transfer procedure [3,4]. Understanding the passive behavior of skeletal muscle is essential to properly employing these surgical procedures. Additionally, the passive properties of muscle play a key role in force transmission throughout the tissue [5]. Intramuscular pressure (IMP) has shown good correlation to muscle force under both active and passive conditions [6–8] and can be directly measured with a pressure microsensor [9]. This link between IMP and muscle force could provide a direct and minimally invasive clinical measurement of individual muscle force, which is currently not possible. Thus, the development of a strong relationship between passive muscle force and IMP is of significant clinical concern.

Muscle, like other biological soft tissues, is a fibrous material saturated with a high fluid content (roughly 80% fluid by volume [10]) that exhibits both tensile and compressive highly nonlinear

This chapter has been published as an Original Paper in Biomechanics and Modeling in Mechanobiology (2016). All content has been adapted with permission from Springer.

[11–16], transversely isotropic [11,14–17], and time dependent [12,16,18–23] behavior. While these mechanical properties have been implemented using finite element analysis amongst a wide range of studies [24–30], the role of fluid content is often ignored despite it's possible role in mechanical behavior [31]. Furthermore, as intramuscular pressure is typically identified as a measurement of fluid pressure [32–35], including interstitial fluid contributions in skeletal muscle finite element models could provide a valuable link between muscle force and IMP. Many of these works have chosen the New Zealand White Rabbit tibialis anterior for study based on the ease of access and low pennation angle [36].

Previous finite element analysis of skeletal muscle force and IMP was successfully utilized using a simplified geometry [37]. However, this approach did not incorporate any time dependency or fluid content and failed to capture whole muscle behavior. These omissions should be reconsidered as they are likely more important than previously thought during tendon transfer surgeries, as whole muscle is passively elongated and held at a constant length, where relaxation typically occurs. Thus, there is a need to develop a muscle finite element model which accurately incorporates whole tissue behavior and time dependency. This work outlines the development and validation of a whole muscle continuum mechanics model which will for the first time use the roles of fluid content and time dependence to accurately predict both intramuscular pressure (IMP) and muscle force under passive stretch conditions.

5.2 Methods

5.2.1 In Situ Testing

The first experimental data set utilized in this study was conducted at the University of California San Diego with Institutional Animal Care and Use Committee approval. In short, the distal tendon of one tibialis anterior (TA) of eight (n=8) New Zealand White rabbits (average rabbit mass and standard error of mean of 3.6 ± 0.04 kg) was transected and attached to a load cell and servomotor similar to previous studies (Figure 5-1A) [6,8]. Animals were anesthetized during testing and euthanized post completion. Each muscle was passively stretched across a range of physiological lengths in 0.05 muscle fiber strain increments at ~0.05 s^{-1} followed by 180 seconds of relaxation. Eleven strain increments which recorded greater than zero reaction force were used for this modeling study, where 0.2 strain was observed as the length at which maximum isometric force was generated. Intramuscular pressure was recorded using a fiber optic pressure transducer [38] (Model FOP-M260-20, Fiso Technologies Inc, Ville de Québec, Canada) within the muscle midbelly (Figure 5-1A). Each transducer was inserted through a 22-gauge catheter and anchored in the tissue with barbs built into a nitinol housing. Muscle stress was calculated as $S = \frac{F}{PCSA}$ where F is force measured at the load cell and PCSA is the physiological cross-sectional area calculated from Equation 1, where V is muscle volume calculated based on measured muscle mass and density, θ_p is pennation angle of 2.5° [36], L_m is measured muscle length with calipers, and L_{fn} is muscle to fiber length ratio [36].

$$PCSA = \frac{V*\cos(\theta_p)}{L_m*L_{fn}} \quad (1)$$

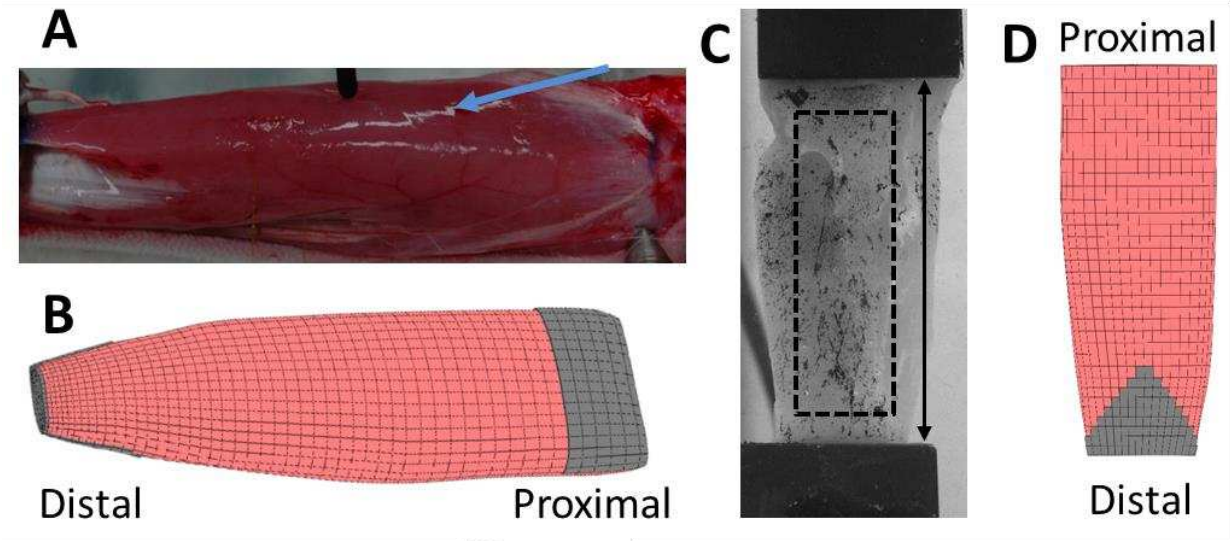

Figure 5-1. Muscle specimens for experimental protocols and the corresponding finite element models. A) *In situ* experimental testing with microsensor insertion (arrow). B) Finite element model for *in situ* comparison, with muscle tissue (red) and aponeurosis (gray). C) Stress relaxation *in vitro* testing, with digital image correlation graphite powder coating and region of interest (dotted box) as well as specimen gauge length (black arrow). D) Finite element model for stress relaxation comparison with muscle tissue (red) and aponeurosis (gray).

5.2.2 Stress Relaxation Testing

Four (n=4) New Zealand White rabbits were euthanized with Colorado State University Institutional Animal Care and Use Committee approval. The tibialis anterior muscles from both hind limbs were dissected out and stored in phosphate buffered saline soaked gauze and refrigerated for tensile stress relaxation testing (total of 8 muscles). All testing was completed within four hours to reduce the effects of rigor mortis [17,39]. Each whole muscle was subject to tensile stress relaxation in a hydraulic material testing system (MTS Bionix 370, Eden Prairie, MN) with a 2 lb load cell (Futek LSB200, Irvine, CA) by clamping the proximal and distal ends of the muscle in thin film grips, leaving a specimen with no distal aponeurosis in the gauge length and only a portion of the proximal aponeurosis in the gauge length (Figure 5-1C). Prior to testing, optical measurements of muscle width and depth were performed using a 1.4 MP monochrome camera (Point Grey Research, Inc., BC, Canada). Image analysis software

(ImageJ, NIH, Bethesda, MD) was used to calculate cross sectional area as is common in tensile testing studies of skeletal muscle [23,15,14,40] based on the assumption of an elliptical cross-sectional shape [18]. All muscles were pre-loaded with a steady-state force of 0.01 N for each test, which is below 0.05% of the failure stress of muscle in the longitudinal direction [14].

Similar to width and depth, the specimen gauge length was measured optically for displacement and rate calculations and each muscle was coated with graphite powder for digital image correlation analysis of tensile strain [18] (Figure 5-1C). One muscle from each animal (either the right or left) was subject to two consecutive ramp-relax steps of 0.05 strain at 0.05 s^{-1}, while the contralateral muscle was subject to two separate single ramp-relax steps of 0.1 strain at strain rates of 0.2 s^{-1} or 0.005 s^{-1} with fifteen minutes between tests (Figure 5-2). The fast rate falls within the range of physiological rates observed during some phases of gait, while the slow rate accounts for possible prolonged stretching either *in vivo* or during surgical intervention [41]. All testing was conducted in a 10% phosphate buffered saline bath in room temperature conditions to ensure hydration of the tissue. The engineering stress was calculated as $S = \frac{F}{A}$ where F is reaction force and A is measured cross sectional area.

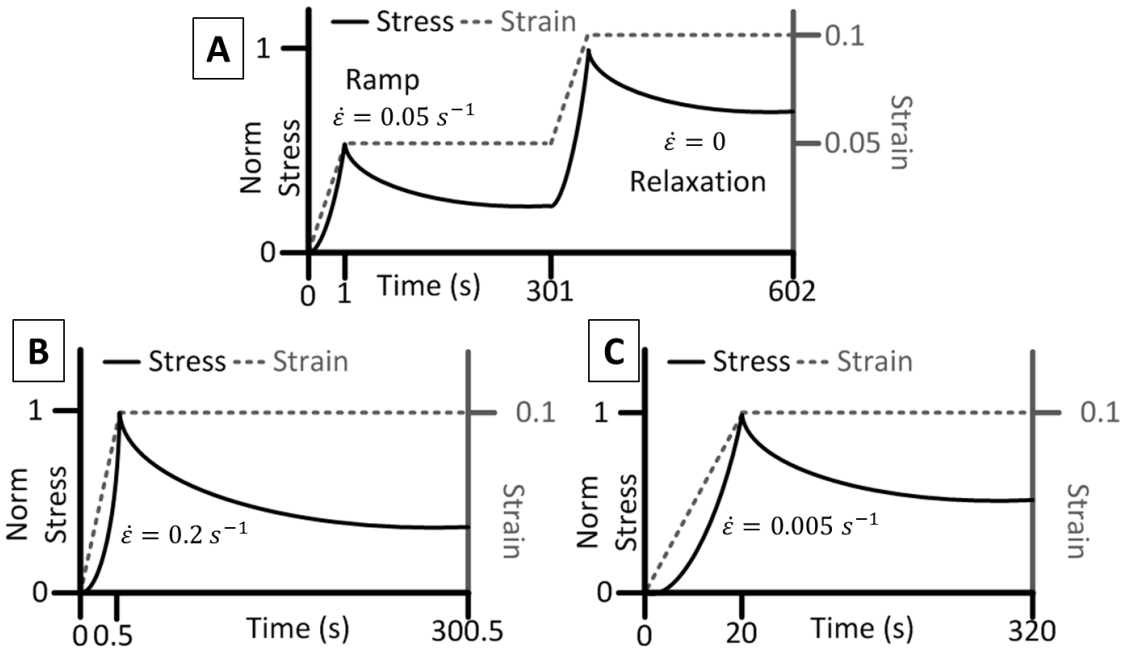

Figure 5-2. Experimental protocol schematics for stress relaxation testing. A) One muscle from each rabbit was subject to two consecutive stress relaxation steps of 0.05 strain at 0.05 s^{-1}. B and C) The contralateral muscle was subject to two separate stress relaxation steps of 0.1 strain at 0.2 s^{-1} and 0.005 s^{-1} with fifteen minutes between each test. The order of tests in B and C was randomized.

5.2.3 Constitutive Model

5.2.3.1 Skeletal Muscle

To properly characterize the complex passive behavior of skeletal muscle, a hyper-poro-viscoelastic constitutive model was implemented. The total stress within this material can be decoupled into contributions from the solid and fluid phase as follows (Equation 2), where $\boldsymbol{\sigma}$ is the total Cauchy stress tensor, $\boldsymbol{\sigma}^s$ is the Cauchy stress tensor of the solid phase only, p is the scalar fluid pressure, and $\boldsymbol{I}$ is the identity tensor. This fluid pressure is driven by Darcy's Law (Equation 3, where Δ is the Grad operator) through a porous medium, where $\boldsymbol{q}$ is fluid flow rate vector, $\boldsymbol{k}$ is material permeability tensor, and μ is the fluid viscosity.

$$\boldsymbol{\sigma} = \boldsymbol{\sigma}^s - p\boldsymbol{I} \tag{2}$$

$$\boldsymbol{q} = -\frac{\boldsymbol{k}}{\mu}\Delta p \tag{3}$$

The stress within a strained elastic solid can be characterized using hyperelasticity, which incorporates a strain energy density function Ψ (Equation 4, where J is the volume ratio, $\boldsymbol{F}$ is the deformation gradient tensor between the reference and spatial configurations and $\boldsymbol{C} = \boldsymbol{F}^T\boldsymbol{F}$ is the right Cauchy Green deformation tensor). For this study, a coupled (compressible) transversely isotropic hyperelastic strain energy density (SED) formulation was utilized (Equation 5, where Ψ is the total strain energy density of the solid, Ψ^{iso} is the isotropic component, and Ψ^{fibers} is the anisotropic component modeled with reinforcing fibers). Here I_1 and I_2 are the first and second invariants of $\boldsymbol{C}$ and I_n are pseudo invariants defined as the square of the stretch $\lambda = \boldsymbol{N}\cdot\boldsymbol{C}\cdot\boldsymbol{N}$ in any direction $\boldsymbol{N}$ in the reference configuration (or $\boldsymbol{n}$ in the spatial configuration) within the material.

$$\boldsymbol{\sigma}^s = 2J^{-1}\boldsymbol{F}\frac{\partial\Psi}{\partial\boldsymbol{C}}\boldsymbol{F}^T \tag{4}$$

$$\Psi(I_1, I_2, J, \boldsymbol{n}, I_n) = \Psi^{iso}(I_1, I_2, J) + \Psi^{fibers}(\boldsymbol{n}, I_n) \tag{5}$$

Unlike other fibrous materials such as tendon [42], ligament [43], meniscus [44], and meniscal attachments [45], muscle is less stiff in the longitudinal direction than in the transverse plane (Mohammadkhah et al., 2016; Takaza et al., 2012; Wheatley et al., 2016b). A typical transversely isotropic model, which consists of an isotropic matrix and a single set of reinforcing fibers [46–49], would not be appropriate for skeletal muscle as it would have a higher stiffness in the longitudinal direction. Thus, a formulation was utilized which included an isotropic ground matrix reinforced with fibers oriented in an ellipsoidal distribution, which allows for modulation of the fiber stiffness based on direction, resulting in transverse isotropy of the tissue [50,51]. Specifically, an isotropic Mooney-Rivlin formulation was used for the ground matrix (Equation 6, where c_1^m, c_2^m, and k^m are parameters which can be interpreted loosely as the isotropic tensile/compressive modulus, isotropic shear modulus, and isotropic bulk modulus of skeletal

muscle). To allow for fluid movement throughout the tissue, Equation 6 is a coupled formulation, which models the volumetric response of this isotropic matrix as compressible. While nearly-incompressible material models are common amongst skeletal muscle studies [25,27,46,52,53], they are not appropriate when utilizing a poroelastic approach as an incompressible assumption results in zero fluid flow after a deformation.

$$\Psi^{iso}(I_1, I_2, J) = {c_1}^m(I_1 - 3) + {c_2}^m(I_2 - 3) - 2({c_1}^m + 2{c_2}^m)\ln J + \frac{k^m}{2}(\ln J)^2 \quad (6)$$

The strain energy contribution from the ellipsoidal fibers includes two parametric functions $\xi(\boldsymbol{n})$ and $\beta(\boldsymbol{n})$ which are implemented to form a continuous three-dimensional power function (Equation 7, where $\xi(\boldsymbol{n})$ and $\beta(\boldsymbol{n})$ are fiber material constants). With the assignment of n_1 in the muscle fiber direction and n_2 and n_3 in the transverse plane, this decomposes the formulation such that the constants $\xi_1 = \xi_{long}$ and $\beta_1 = \beta_{long}$ characterize the tensile behavior in the longitudinal direction, while $\xi_2 = \xi_3 = \xi_{trans}$ and $\beta_2 = \beta_3 = \beta_{trans}$ characterize the tensile behavior in the transverse plane. Both $\xi(\boldsymbol{n})$ and $\beta(\boldsymbol{n})$ are described by the same function (Equation 8, where θ is the angle between the first and second primary directions of the local coordinate system, φ is the angle between the third primary direction and its perpendicular plane, and all ξ can be replaced with β for the equation to describe $\beta(\boldsymbol{n})$), which results in a continuous transition of elastic behavior between three orthogonal unit vectors (in this case the fiber direction unit vector and two perpendicular unit vectors in the transverse plane).

$$\Psi^{fibers}(\boldsymbol{n}, I_n) = \xi(\boldsymbol{n})(I_n - 1)^{\beta(\boldsymbol{n})} \quad (7)$$

$$\xi(\boldsymbol{n}) = \left(\frac{\cos^2\theta\sin^2\varphi}{\xi_1^2} + \frac{\sin^2\theta\sin^2\varphi}{\xi_2^2} + \frac{\cos^2\varphi}{\xi_3^2}\right) \quad (8)$$

The final component of the utilized constitutive model was viscoelasticity of the solid phase. Skeletal muscle exhibits a time dependent passive response (Van Loocke et al., 2008; Wheatley

et al., 2016a, 2016b), and while fluid content in a biphasic model can account for much of the time dependence under compressive conditions [54–56], tensile time dependence is generally the result of inherent viscoelasticity of collagen [57]. This time dependent response was applied using a relaxation function $G(t)$ (Equation 9, where t is time and ζ is an integration variable). This relaxation function was defined through a Prony series shown in Equation 10, where N is the number of terms in the series, g_i are the viscoelastic relaxation parameters, and τ_i are time constants.

$$\boldsymbol{\sigma}(t) = \int_{-\infty}^{t} G(t-\zeta)\frac{d\boldsymbol{\sigma}}{d\zeta}d\zeta \tag{9}$$

$$G(t) = 1 + \sum_{i=1}^{N} g_i e^{\left(-\frac{t}{\tau_i}\right)} \tag{10}$$

5.2.3.2 Aponeurosis and Tendon

Similar to the solid phase of muscle, the aponeurosis and tendon elements were modeled using a transversely isotropic strain energy density function and viscoelastic Prony series [58,59]. As the longitudinal direction of aponeurosis and tendon is stiffer than the transverse [42], an uncoupled transversely isotropic Mooney-Rivlin strain energy density function was implemented (Equation 11, where $\bar{I}_1$ and $\bar{I}_2$ are invariants from the deviatoric right Cauchy Green deformation tensor, and ${c_1}^a$, ${c_2}^a$, and k^a are similar parameters from Equation 6 but for aponeurosis and tendon). The fiber contribution in this model utilized the deviatoric stretch $\bar{\lambda}$ and the stress can be described by Equation 12, where ${c_3}^a$ and ${c_4}^a$ describe the nonlinear tensile stiffness of these fibers in the toe region, ${c_5}^a$ is the modulus once fibers have exited the toe region, ${c_6}^a$ maintains continuity between the linear and toe region, and λ_m is the stretch at the end of the toe region. This decoupling of the invariants and fiber stretch from the volumetric response allows the aponeurosis and tendon to be easily modeled as nearly incompressible [48].

$$\Psi(\bar{I}_1, \bar{I}_2, J, \bar{\lambda}) = {c_1}^a(\bar{I}_1 - 3) + {c_2}^a(\bar{I}_2 - 3) + \frac{k^a}{2}(\ln J)^2 + \Psi^{fibers}(\bar{\lambda}) \quad (11)$$

$$\bar{\lambda}\frac{\partial \Psi^{fibers}}{\partial \bar{\lambda}} = \begin{cases} 0, & \bar{\lambda} \leq 1 \\ {c_3}^a\left(e^{{c_4}^a(\bar{\lambda}-1)} - 1\right), & 1 < \bar{\lambda} < \lambda_m \\ {c_5}^a\bar{\lambda} + {c_6}^a, & \bar{\lambda} \geq \lambda_m \end{cases} \quad (12)$$

5.2.4 Finite Element Model Development

An isolated New Zealand White Rabbit tibialis anterior muscle was scanned using micro computed tomography (Scanco μCT 80, Scanco Medical AG, Brüttisellen, Switzerland) with a 25 μm voxel size. The resulting images were imported into image segmentation software (3DSlicer, www.slicer.org) to generate a three dimensional muscle surface. This surface was meshed with manual hexahedral meshing software (TrueGrid, XYZ Scientific Applications, Inc., Pleasant Hill, CA) to create a tibialis anterior muscle mesh. The physiological area of aponeurosis tissue was visually measured and applied to the mesh in the form of an additional layer of three dimensional hexahedral elements (thickness = 0.2 mm to approximate the behavior of shell elements) which share nodes with the muscle geometry. The elements on the proximal and distal faces were identified as tendon and were considered to have the same material properties as the aponeurosis elements. The final three-dimensional mesh thus included two materials (muscle and aponeurosis/tendon) for the isolated rabbit tibialis anterior (Figure 5-1B) and was implemented in the nonlinear finite element analysis software FEBio [60]. For all analyses, the nodes of the proximal face were pinned (displacement in x=y=z=0), the distal face nodes were displaced in the z-direction (along the length of the tissue from proximal to distal), and the tissue boundary was modeled as impermeable.

A mesh convergence study was completed on the muscle model in the form of five meshes, each with increasing mesh density with the above constitutive model. Each mesh was displaced to 0.4 engineering strain along the muscle length at a constant rate of 0.01 sec^{-1}. The total reaction force at the distal nodes, mean fluid pressure for the midbelly elements, and the computation time were evaluated to determine the appropriate mesh to be utilized. Specifically, these values for each of the first four meshes were compared to the densest mesh at four points: 0.1, 0.2, 0.3, and 0.4 strain and the average percent difference was calculated. The third mesh from the convergence study was selected as it demonstrated less than 0.15% difference from the densest mesh while maintaining a low computation time relative to the other meshes (Table 5-1).

Table 5-1. Mesh convergence for five various mesh densities. Each mesh was compared against the densest mesh. Mesh 3 (bold) had very low differences (<0.15%) in both total reaction force and fluid pressure from mesh 5, while considerably reducing computation time. Mesh 3 has a mean element size of 0.59 mm^3.

Mesh	Elements	Computation Time (min)	Computation Time % Diff	Reaction Force % Diff	Fluid Pressure % Diff
1	572	1.6	97%	1.85%	0.60%
2	1596	8.6	83%	1.06%	0.46%
3	**5408**	**12.4**	**76%**	**0.15%**	**0.13%**
4	19152	16.9	67%	-0.02%	0.08%
5	46400	50.5	-	-	-

To simulate experimental conditions, the distal end of the model was displaced over a short ramp phase (1 second in this case) to generate 0.05 fiber strain increments and allowed to relax over 180 seconds. This was completed a total of eleven times for a total of 0.55 maximum fiber strain. The reaction force at each of the distal nodes (142 in total) was summed to generate a total reaction force for the entire muscle. This force was then used to calculate the muscle fiber stress for *in situ* experimental comparison. Passive muscle stress was calculated by dividing reaction

force by the PCSA (Equation 1), which was calculated based on the volume of the model V (3363 mm^3 measured computationally), the length of the model L_m (56.1 mm measured computationally), and the pennation angle θ_p (2.5°) and fiber length to muscle length ratio L_{fn} (0.67) from literature similar to the experimental protocol [36]. Intramuscular pressure was interpreted as the mean fluid pressure for six midbelly elements, which were located around the center of the mesh similar to pressure microsensor location in the experimental protocol.

For simulation of stress relaxation testing, the proximal and distal ends of the model were removed to simulate how the experimental setup gripped the muscle (~40 mm gauge length, Figure 5-1C), leaving 3522 hexahedral elements (Figure 5-1D). Stress relaxation conditions were applied by pinning the proximal end of the tissue (x=y=z=0 displacement) and after applying a pre-load of 0.01 N identical to the experiment, displacing the distal end according to the measured digital image correlation strain of each specimen. This resulted in multiple stress relaxation outputs for each loading protocol, with slight variability in applied strain as a result of the measured experimental strain. The cross section of the muscle was measured using the same procedure as the experimental protocol and the total reaction force on the distal face was used to calculate the engineering stress in the same manner as the experiment.

5.2.5 Optimization and Validation Procedures

The first step in model implementation was to determine material parameters (Table 5-2) which were not optimized. These included the c_1, c_2, and k hyperelastic parameters for both muscle and aponeurosis (Equations 6 and 11), the viscoelastic parameters for both muscle and aponeurosis (Equation 10), and the fiber parameters for aponeurosis (Equation 12). The viscoelastic g_i

parameters for skeletal muscle were determined by fitting the relaxation curve of specimens from the single fast ramp stress relaxation test (Figure 5-2B), using decade time constant values of $\tau_i = 0.1, 1, 10, 100$ seconds (Troyer et al., 2012; Wheatley et al., 2016a, 2016d). The hydraulic permeability of muscle was assumed to be a constant value of 7.41×10^{-11} m^4/N-s, based on previous experimental and modeling research suggesting the assumption of a constant, isotropic permeability is appropriate for skeletal muscle (Wheatley et al., 2016c). As skeletal muscle is stiffer in the transverse direction (Mohammadkhah et al., 2016; Takaza et al., 2012; Wheatley et al., 2016a), the transverse stiffness was fixed relative to the longitudinal stiffness as follows: $\xi_{trans} = 10 * \xi_{long}$ (Wheatley et al., 2016a). Finally, as the transverse tensile behavior of skeletal muscle exhibits nearly linear behavior (Mohammadkhah et al., 2016; Takaza et al., 2012; Wheatley et al., 2016b), the β_{trans} parameter was fixed at $\beta_{trans} = 3$. The muscle c_1 parameter was determined based on the low modulus of muscle in compression [17], the c_2 parameter was utilized from previously published literature [27], and the k parameter was chosen to maintain compressibility of the solid matrix in a poroelastic material [49]. With the exception of λ_m [27], all aponeurosis parameters were implemented to ensure model behavior was in agreement with experimental studies from literature [58,63–65]. Finally, it is important to note that c_6 from Equation 12 is calculated based on the other parameters to satisfy continuity [27].

Table 5-2. Constitutive material parameters for skeletal muscle and aponeurosis which were utilized within the finite element model, excluding the reinforcing fibers from skeletal muscle. These parameters were fixed during the optimization process.

	c_1 (kPa)	c_2 (kPa)	k (kPa)	τ_i (seconds)	g_i (-)	c_3 (kPa)	c_4 (-)	c_5 (kPa)	λ_m (-)
Muscle	0.05	0.5	5	0.1, 1, 10, 100	1.3, 0.48, 0.29, 0.17	-	-	-	-
Aponeurosis	1E4	500	5E5	0.33, 47.5, 2500	0.20, 0.13, 0.19	50	40	1E5	1.03

The whole muscle finite element model was fit to experimental *in situ* stress data using the nonlinear least squares algorithm *lsqnonlin* in Matlab (The Mathworks, Inc., Natick, MA). This solver was utilized as it allows bounds to be applied to constitutive parameters while fitting nonlinear data. Model stress was calculated as reaction force at the distal face divided by PCSA in the same manner as the experiment. The residual between muscle fiber stress from the model and experimental data at the eleven strain increments (0.05-0.55) was optimized per Equation 13, where ${S^e}_n$ are the experimental stress values and ${S^m}_n$ are the model stress values at the n^{th} time point.

$$residual = \sum_{i=1}^{11} \left[\frac{{S^e}_i - {S^m}_i}{{S^e}_i}\right]^2 \tag{13}$$

This method of fitting only muscle stress directly allowed for simple validation of intramuscular pressure data. Similar to stress, intramuscular pressure at each strain increment (0.05-0.55) was compared against model midbelly fluid pressure. Specifically, the fits of stress and pressure were evaluated using the *GoodnessOfFit* function in Matlab (Equation 14, where ${y^e}_i$ and ${y^m}_i$ correspond to the experimental stress/pressure and model stress/pressure, respectively). Here a perfect fit yields a value of one, where experiment and model data are identical, and the worst possible fit yields a value of negative infinity. For validation of muscle stress, the model was compared against experimental stress relaxation data using Equation 13. The mean experimental stress relaxation curves and mean model stress relaxation curves were compared with a single fit using Equation 14.

$$fit = 1 - \sum_{i=1}^{11} \left[\frac{{y^e}_i - {y^m}_i}{{y^m}_i - mean(y^e)}\right]^2 \tag{14}$$

5.3 Results

The optimization procedure, which fit model stress to *in situ* experimental stress, was highly successful both through visual inspection (Figure 5-3A), and through statistical analysis (NMSE fit value of 0.993). Similarly, the validation of model fluid pressure to *in situ* experimental intramuscular pressure showed a very good fit both visually (Figure 5-3B) and statistically (NMSE fit value of 0.955). Final optimized parameters (Table 5-3) show the well-observed nonlinear passive tensile behavior of muscle in the longitudinal direction (Takaza et al., 2012; Wheatley et al., 2016a; Wheatley et al., 2016b).

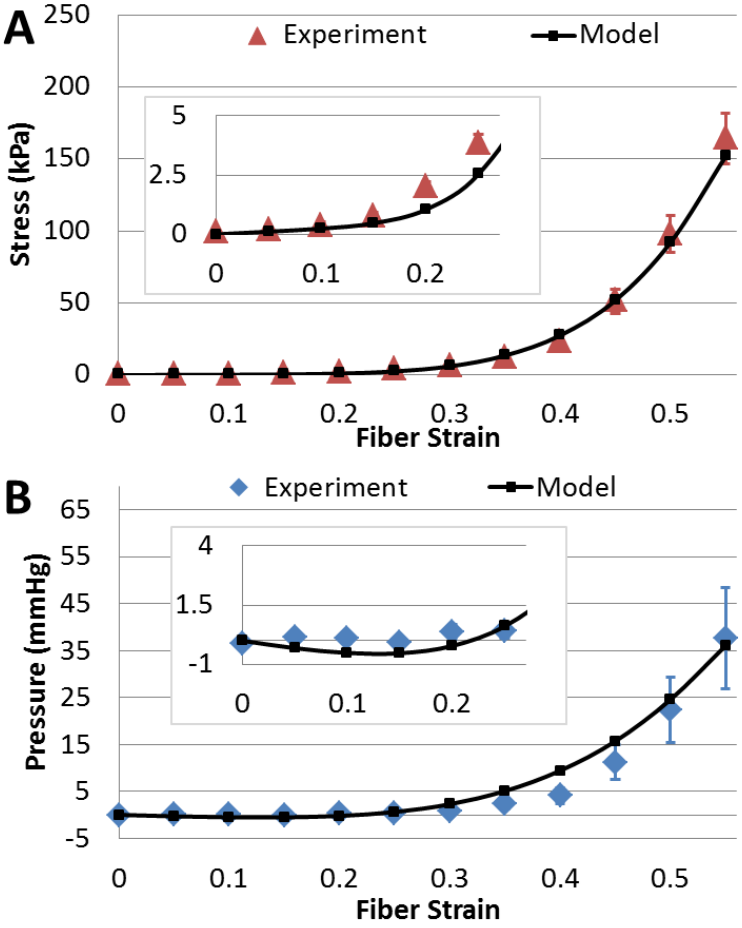

Figure 5-3. A) Model fit to *in situ* experimental stress (standard error bars) data using nonlinear optimization. The inset image shows a highlight of the same data at lower strain levels. The NMSE fit value for these data is 0.993. B) Model validation to *in situ* experimental intramuscular pressure data with similar inset image of lower strain levels. The NMSE fit value for these data is 0.955.

Table 5-3. Muscle ellipsoidal reinforcing fiber parameter values. The longitudinal parameters were optimized using the nonlinear algorithm (denoted with *), while the transverse parameters were fixed as follows: $\xi_{trans} = 10 * \xi_{long}$ and $\beta_{trans} = 3$.

Ellipsoidal Fibers	$\boldsymbol{\xi_{long}}$ **(kPa)**	$\boldsymbol{\xi_{trans}}$ **(kPa)**	$\boldsymbol{\beta_{long}}$ **(-)**	$\boldsymbol{\beta_{trans}}$ **(-)**
Muscle	3.299*	32.99	7.34*	3

The measured digital image correlation strain values from the *in vitro* stress relaxation tests were 0.102 ± 0.30 (mean ± standard error of the mean). All samples showed the typical stress relaxation behavior previously observed for skeletal muscle under tensile conditions (Wheatley et al., 2016a). Validation of muscle stress for the three stress relaxation curves was also successful, as visual inspection shows a high level of overlap of model and experimental standard error (Figure 5-4). The NMSE fit value of 0.860 for these three curves further supports these findings. Note that the variability in model output shown with standard error bars is the result of matching finite element model boundary conditions to variation in experimental specimen strain as tracked with digital image correlation.

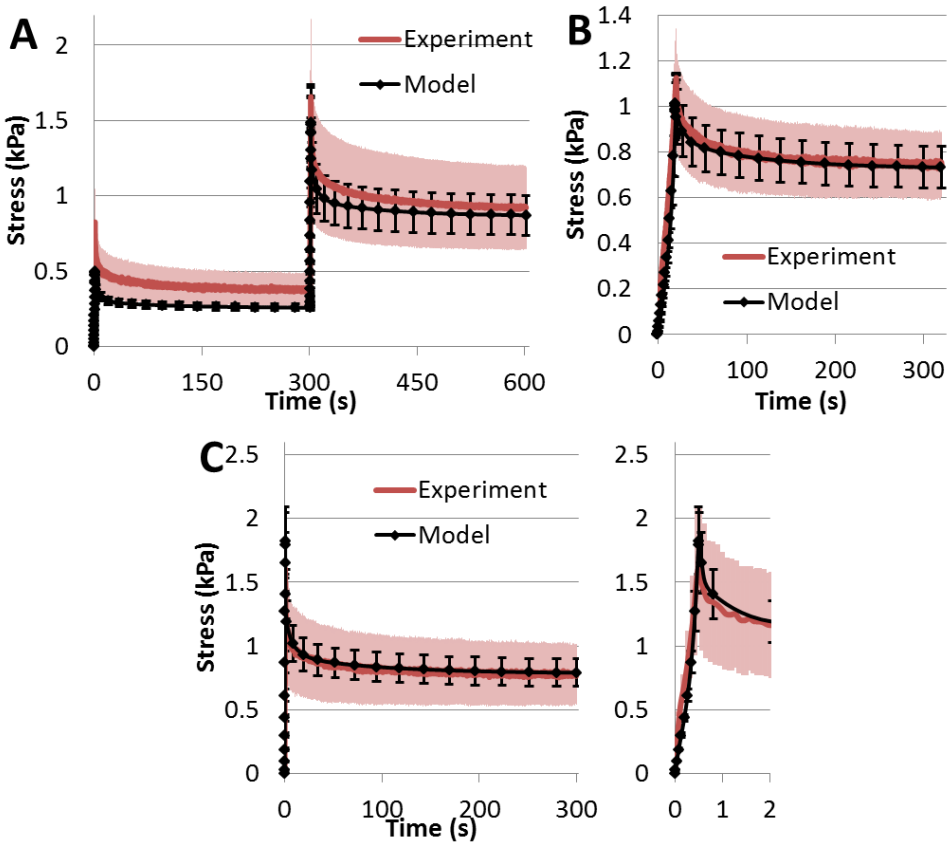

Figure 5-4. Model validation for *in vitro* experimental stress relaxation data for A) two step stress relaxation, B) single slow step stress relaxation, and C) single fast step stress relaxation with initial ramp and relaxation highlighted on right for clarity. The NMSE fit value for this validation is 0.860 with standard error bars shown.

5.4 Discussion

To the best of the authors' knowledge, this work presents the first study which utilized a hyper-poro-viscoelastic approach to model skeletal muscle. While previous studies have employed hyperelasticity [17,24,27,37,46,52,66–68] or hyper-viscoelasticity (Gras et al., 2013; Khodaei et al., 2013; Lu et al., 2010; Van Loocke et al., 2009, 2008, Wheatley et al., 2016a, 2016d) to model skeletal muscle under a wide range of conditions, poroelasticity is not typically incorporated. These models utilize viscoelasticity alone to describe the time dependent relaxation of the tissue. However, poro-viscoelastic theory has been applied in studies of other tissues such as meniscus [49], bone [71], and cartilage [57,72]. Furthermore, evidence suggests fluid content

in skeletal muscle plays a role in the time dependent behavior of the tissue [31]. The permeability value used in this study was determined experimentally through direct measurement, with subsequent finite element analysis suggesting anisotropy and strain dependence playing a minor role in passive muscle mechanics (Wheatley et al., 2016c). While the contribution of fluid pressure to relaxation in tension is most likely minimal [57], we chose to implement it for two reasons: 1) poroelastic theory allows for the interpretation of fluid pressure as intramuscular pressure, and 2) this formulation could be utilized in an *in vivo* model of skeletal muscle, which may be subject to compressive conditions where fluid content plays a key role in biological tissue behavior [57,73,74].

The utilized optimization approach required the varying of only two parameters out of a total of nineteen used: the stiffness and nonlinearity of the longitudinal reinforcing fibers (Equation 7). This greatly simplified the approach by eliminating parameter optimization which could result in a non-unique set of final parameters [49]. Additionally, this makes translation from rabbit to human muscle more streamlined, as it would require minimum changes to only these parameters, not the whole constitutive model. Future modeling analysis should be completed to evaluate the accuracy of the parameters utilized in this study in predicting human muscle mechanics and how this model behaves under compressive conditions.

The model presented here also provides the only whole muscle analysis to predict both passive muscle stress and intramuscular pressure. Previous work correctly identified muscle stress and intramuscular pressure of muscle in an idealized geometry [37]. While our work utilizes fluid pressure as an interpretation of intramuscular pressure, Jenkyn et al used solid pressure, which is

calculated from the Cauchy stress tensor of the solid constituent. While it remains unclear exactly what the physiological mechanism for intramuscular pressure is, it is clear the sensors measure fluid pressure and have been designed to reduce contact between the sensor diaphragm and any solid constituents within the tissue [38]. Thus, it is unlikely the utilized sensors are capable of accurately measuring solid pressure. Additionally, the model presented here incorporates time dependency of the tissue which Jenkyn et al did not model. Stress relaxation or creep is an important physiological mechanism in soft tissue behavior and could greatly affect the identification of muscle resting length during procedures such as tendon transfer surgery.

The constitutive model implemented for aponeurosis from this study is based on the anisotropic behavior observed experimentally [64] and is consistent with previous finite element approaches [52,53]. Specifically, this formulation provides an isotropic nearly-incompressible ground matrix with a single set of reinforcing fibers which support tension only. With the exception of λ_m, the specific parameters were modified from previously utilized values for tendon and aponeurosis [27] to ensure agreement with experimental data. Previously published works suggest aponeurosis strain values of ~0.08 at maximum contraction [29,63–65], which is similar to the maximum stress from this study [6]. Thus, the observed ~0.08 maximum Lagrange strain found in this work (Figure 5-5), suggests the constitutive model utilized here was accurate.

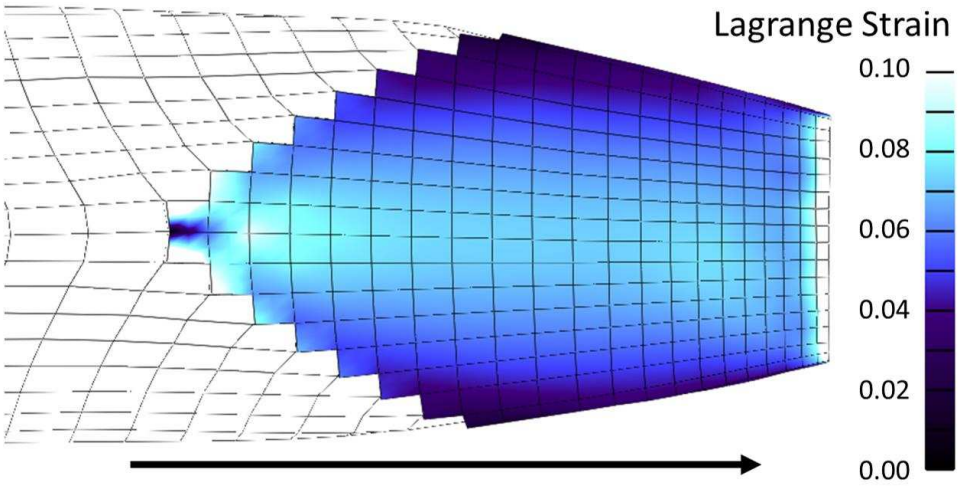

Figure 5-5. Aponeurosis Lagrange strain in the direction of stretch at (denoted with black arrow). The maximum observed value of roughly 0.08 corresponds well to experimental studies of aponeurosis strain[29,63–65].

One potential limitation of this work was the difficulty of developing of a constitutive model in which the transverse direction is stiffer than the longitudinal direction in tension, which is consistent with previously published literature (Mohammadkhah et al., 2016; Takaza et al., 2012; Wheatley et al., 2016b). Further complicating the scenario is that the longitudinal direction exhibits a high degree of tensile nonlinearity, while the transverse direction alternatively has a more linear tensile response (Takaza et al., 2012; Wheatley et al., 2016b). Thus typical orthotropic models such as a Fung Orthotropic material [75–77] or an orthotropic linear elastic material [78] would not accurately characterize the tissue transverse isotropy, as they do not account for variations in spatial linearity. In this scenario – a transversely isotropic material where the plane of isotropy is stiffer and more linear than the first primary direction – an implementation of true transverse isotropy would require a unique set of invariants [79]. Specifically, there would be no "isotropic" invariants, as each would have some directional dependence. As this type of a response is not common in biological tissues, these constitutive models are typically not common in finite element analysis. Thus, to closely simulate muscle

transverse isotropy, an isotropic coupled Mooney-Rivlin strain energy density (SED) function was utilized with three-dimensional ellipsoidal reinforcing fibers. This formulation allowed for the muscle fiber direction to exhibit a high level of tensile nonlinearity, while keeping the transverse direction relatively linear and with a higher stiffness. The drawback from this method is the isotropic tensile/compressive response of the SED equation (c_1 from Equation 6) was simply given a low parameter value of 0.05 kPa.

While the validation method from this work shows excellent agreement to experimental data under uniaxial tension, this represents only one loading condition. The transversely isotropic optimized muscle constitutive model can thus be compared against previously published experimental data on skeletal muscle under tensile conditions for further validation. In short, an idealized geometry was implemented into two finite element models to determine the model Cauchy stress in the direction of deformation under quasi-static (strain rate of 0.05% s^{-1}) longitudinal and transverse tension. This simulated tensile testing of excised samples similar to experimental studies. When comparing against the data summarized by Mohammadkhah et al. 2016, there is good agreement for both orientations, though our model predicts a larger toe region than observed experimentally. Specifically, our model predicts 100 kPa of Cauchy stress at approximately 0.41 strain compared to the observed values of roughly 0.3-0.4 strain under longitudinal tension [14,46,80]. For transverse tension, our predicted strain level at 50 kPa is roughly 0.26 strain compared against experimental values of roughly 0.07-0.2 [14,40,80]. These small differences could be the result of differences in testing protocol versus simulation or anatomical and species variations.

One important distinction to make is the definition of zero strain from this work compared to the *in situ* data. In some cases, muscle resting length was identified by locating the length at which isometric force was greatest. For this study, which focused on passive stretch only, zero strain was identified by determining the point at which passive tension was recruited. This resulted in a difference of 0.2 strain between what was identified here as zero strain (passive tension was first measured) and as optimal length (maximum isometric force). This toe region of 0.2 strain showed relatively low stress values (<1 kPa), yet increased in nonlinear fashion with strain and as such was identified as an important region to accurately model.

Future work will incorporate muscle activation, as active muscle force is also correlated with intramuscular pressure (IMP) [6–8]. Additionally, *in vivo* geometry, including contact between muscle and surrounding tissue should be studied. These additions would significantly strengthen the physiological relevance of this model by expanding to clinical conditions where active and passive muscle force could be measured. As there exists no current clinical technique to measure muscle force *in vivo*, the use of a pressure microsensor to evaluate IMP and thus estimate muscle force could provide an impactful and novel clinical tool. A validated finite element model which predicts both muscle force and IMP could provide important insight into the force-IMP relationship *in vivo*.

5.5 Conclusions

This work presented a novel finite element model of skeletal muscle, which was the first to implement fluid behavior through poroelastic theory and the first whole muscle model to accurately predict intramuscular pressure (IMP). It was independently validated against both

IMP and passive muscle force, exhibited aponeurosis behavior consistent with physiological observations from literature, and used a novel constitutive approach to accurately characterize the tensile transverse isotropy of the tissue. This model could be utilized to guide surgeries such as a tendon transfer procedure, where skeletal muscle is passively stretched to a new tendon insertion location. Future work should include muscle activation and an *in vivo* environment to increase clinical relevance.

REFERENCES

[1] Baumgartner, R. N., Koehler, K. M., Gallagher, D., Romero, L., Heymsfield, S. B., Ross, R. R., Garry, P. J., and Lindeman, R. D., 1998, "Epidemiology of Sarcopenia among the Elderly in New Mexico," Am. J. Epidemiol., **147**(8), pp. 755–763.

[2] Lieber, R. L., 2010, Skeletal Muscle Structure, Function, and Plasticity, Lippincott Williams and Wilkins, Philadelphia, PA.

[3] Fridén, J., and Lieber, R. L., 1998, "Evidence for muscle attachment at relatively long lengths in tendon transfer surgery.," J. Hand Surg. Am., **23**(1), pp. 105–110.

[4] Fridén, J., and Lieber, R. L., 2002, "Tendon transfer surgery: clinical implications of experimental studies.," Clin. Orthop. Relat. Res., (403 Suppl), pp. S163-70.

[5] Huijing, P. A., 1999, "Muscle as a collagen fiber reinforced composite: A review of force transmission in muscle and whole limb," J. Biomech., **32**(4), pp. 329–345.

[6] Davis, J., Kaufman, K. R., and Lieber, R. L., 2003, "Correlation between active and passive isometric force and intramuscular pressure in the isolated rabbit tibialis anterior muscle," J. Biomech., **36**(4), pp. 505–512.

[7] Winters, T. M., Sepulveda, G. S., Cottler, P. S., Kaufman, K. R., Lieber, R. L., and Ward, S. R., 2009, "Correlation between isometric force and intramuscular pressure in rabbit tibialis anterior muscle with an intact anterior compartment," Muscle and Nerve, **40**(1), pp. 79–85.

[8] Ward, S. R., Davis, J., Kaufman, K. R., and Lieber, R. L., 2007, "Relationship between muscle stress and intramuscular pressure during dynamic muscle contractions," Muscle and Nerve, **36**(3), pp. 313–319.

[9] Kaufman, K. R., Wavering, T., Morrow, D., Davis, J., and Lieber, R. L., 2003, "Performance characteristics of a pressure microsensor," J. Biomech., **36**(2), pp. 283–287.

[10] Sjøgaard, G., and Saltin, B., 1982, "Extra- and intracellular water spaces in muscles of man at rest and with dynamic exercise.," Am. J. Physiol., **243**(3), pp. R271-80.

[11] Pietsch, R., Wheatley, B. B., Haut Donahue, T. L., Gilbrech, R., Prabhu, R., Liao, J., and Williams, L. N., 2014, "Anisotropic compressive properties of passive porcine muscle tissue.," J. Biomech. Eng., **136**(11), p. 111003.

[12] Rehorn, M. R., Schroer, A. K., and Blemker, S. S., 2014, "The passive properties of muscle fibers are velocity dependent," J. Biomech., **47**(3), pp. 687–693.

[13] Simms, C. K., Van Loocke, M., and Lyons, C. G., 2012, "Skeletal muscle in compression: modeling approaches for the passive muscle bulk.," Multiscale Comput. Eng., **10**(2), pp. 143–154.

[14] Takaza, M., Moerman, K. M., Gindre, J., Lyons, G., and Simms, C. K., 2012, "The anisotropic mechanical behaviour of passive skeletal muscle tissue subjected to large tensile strain," J. Mech. Behav. Biomed. Mater., **17**, pp. 209–220.

[15] Wheatley, B. B., Odegard, G. M., Kaufman, K. R., and Donahue, T. L. H., 2016, "How does tissue preparation affect skeletal muscle transverse isotropy?," J. Biomech., **49**(13), pp. 3056–3060.

[16] Wheatley, B. B., Pietsch, R. B., Haut Donahue, T. L., and Williams, L. N., 2016, "Fully

non-linear hyper-viscoelastic modeling of skeletal muscle in compression.," Comput. Methods Biomech. Biomed. Engin., **19**(11), pp. 1181–9.
[17] Van Loocke, M., Lyons, C. G., and Simms, C. K., 2006, "A validated model of passive muscle in compression," J. Biomech., **39**(16), pp. 2999–3009.
[18] Abraham, A. C., Kaufman, K. R., and Haut Donahue, T. L., 2012, "Phenomenological consequences of sectioning and bathing on passive muscle mechanics of the New Zealand white rabbit tibialis anterior," J. Mech. Behav. Biomed. Mater., **17**, pp. 290–295.
[19] Gras, L. L., Mitton, D., Viot, P., and Laporte, S., 2013, "Viscoelastic properties of the human sternocleidomastoideus muscle of aged women in relaxation," J. Mech. Behav. Biomed. Mater., **27**, pp. 77–83.
[20] Meyer, G. A., McCulloch, A. D., and Lieber, R. L., 2011, "A Nonlinear Model of Passive Muscle Viscosity," J. Biomech. Eng., **133**(9), p. 91007.
[21] Van Loocke, M., Lyons, C. G., and Simms, C. K., 2008, "Viscoelastic properties of passive skeletal muscle in compression: Stress-relaxation behaviour and constitutive modelling," J. Biomech., **41**(7), pp. 1555–1566.
[22] Van Loocke, M., Simms, C. K., and Lyons, C. G., 2009, "Viscoelastic properties of passive skeletal muscle in compression-Cyclic behaviour," J. Biomech., **42**(8), pp. 1038–1048.
[23] Wheatley, B. B., Morrow, D. A., Odegard, G. M., Kaufman, K. R., and Haut Donahue, T. L., 2016, "Skeletal muscle tensile strain dependence: Hyperviscoelastic nonlinearity.," J. Mech. Behav. Biomed. Mater., **53**, pp. 445–54.
[24] Johansson, T., Meier, P., and Blickhan, R., 2000, "A finite-element model for the mechanical analysis of skeletal muscles.," J. Theor. Biol., **206**(1), pp. 131–49.
[25] Hernández-Gascón, B., Grasa, J., Calvo, B., and Rodríguez, J. F., 2013, "A 3D electro-mechanical continuum model for simulating skeletal muscle contraction.," J. Theor. Biol., **335**, pp. 108–18.
[26] Tang, C. Y., Zhang, G., and Tsui, C. P., 2009, "A 3D skeletal muscle model coupled with active contraction of muscle fibres and hyperelastic behaviour.," J. Biomech., **42**(7), pp. 865–72.
[27] Blemker, S. S., Pinsky, P. M., and Delp, S. L., 2005, "A 3D model of muscle reveals the causes of nonuniform strains in the biceps brachii.," J. Biomech., **38**(4), pp. 657–65.
[28] Hodgson, J. a, Chi, S.-W., Yang, J. P., Chen, J.-S., Edgerton, V. R., and Sinha, S., 2012, "Finite element modeling of passive material influence on the deformation and force output of skeletal muscle.," J. Mech. Behav. Biomed. Mater., **9**, pp. 163–83.
[29] Chi, S., Hodgson, J., Chen, J., Reggie Edgerton, V., Shin, D. D., Roiz, R. A., and Sinha, S., 2010, "Finite element modeling reveals complex strain mechanics in the aponeuroses of contracting skeletal muscle.," J. Biomech., **43**(7), pp. 1243–50.
[30] Yucesoy, C. A., Koopman, B. H. F. J. M., Huijing, P. A., and Grootenboer, H. J., 2002, "Three-dimensional finite element modeling of skeletal muscle using a two-domain approach: linked fiber-matrix mesh model," J. Biomech., **35**(9), pp. 1253–1262.
[31] Yang, M., and Taber, L. A., 1991, "The possible role of poroelasticity in the apparent viscoelastic behavior of passive cardiac muscle.," J. Biomech., **24**(7), pp. 587–97.
[32] Sejersted, O. M., Hargens, A. R., Kardel, K. R., Blom, P., Jensen, O., and Hermansen, L., 1984, "Intramuscular fluid pressure during isometric contraction of human skeletal muscle.," J. Appl. Physiol., **56**(2), pp. 287–95.
[33] Sejersted, O. M., and Hargens, A. R., 1995, "Intramuscular pressures for monitoring

different tasks and muscle conditions.," Adv. Exp. Med. Biol., **384**, pp. 339–350.
[34] Aratow, M., Ballard, R. E., Crenshaw, A. G., Styf, J., Watenpaugh, D. E., Kahan, N. J., and Hargens, A. R., 1993, "Intramuscular pressure and electromyography as indexes of force during isokinetic exercise," J Appl Physiol, **74**(6), pp. 2634–2640.
[35] Körner, L., Parker, P., Almström, C., Andersson, G. B., Herberts, P., Kadefors, R., Palmerud, G., and Zetterberg, C., 1984, "Relation of intramuscular pressure to the force output and myoelectric signal of skeletal muscle.," J. Orthop. Res., **2**(3), pp. 289–96.
[36] Lieber, R. L., and Blevins, F. T., 1989, "Skeletal muscle architecture of the rabbit hindlimb: functional implications of muscle design.," J. Morphol., **199**(1), pp. 93–101.
[37] Jenkyn, T., Koopman, B., Huijing, P. a, Lieber, R. L., and Kaufman, K. R., 2002, "Finite element model of intramuscular pressure during isometric contraction of skeletal muscle.," Phys. Med. Biol., **47**, pp. 4043–4061.
[38] Go, S. A., Jensen, E. R., O'Connor, S. M., Evertz, L. Q., Morrow, D. A., Ward, S. R., Lieber, R. L., and Kaufman, K. R., 2017, "Design Considerations of a Fiber Optic Pressure Sensor Protective Housing for Intramuscular Pressure Measurements," Ann. Biomed. Eng., **45**(3), pp. 739–746.
[39] Van Ee, C. A., Chasse, A. L., and Myers, B. S., 2000, "Quantifying skeletal muscle properties in cadaveric test specimens: effects of mechanical loading, postmortem time, and freezer storage.," J. Biomech. Eng., **122**(1), pp. 9–14.
[40] Mohammadkhah, M., Murphy, P., and Simms, C. K., 2016, "The in vitro passive elastic response of chicken pectoralis muscle to applied tensile and compressive deformation," J. Mech. Behav. Biomed. Mater., **62**, pp. 468–480.
[41] Hoyt, D. F., 2005, "In vivo muscle function vs speed I. Muscle strain in relation to length change of the muscle-tendon unit," J. Exp. Biol., **208**(6), pp. 1175–1190.
[42] Lynch, H. A., Johannessen, W., Wu, J. P., Jawa, A., and Elliott, D. M., 2003, "Effect of fiber orientation and strain rate on the nonlinear uniaxial tensile material properties of tendon.," J. Biomech. Eng., **125**(5), pp. 726–31.
[43] Quapp, K. M., and Weiss, J. A., 1998, "Material Characterization of Human Medial Collateral Ligament," J. Biomech. Eng., **120**(6), p. 757.
[44] Proctor, C. S., Schmidt, M. B., Whipple, R. R., Kelly, M. A., and Mow, V. C., 1989, "Material properties of the normal medial bovine meniscus.," J. Orthop. Res., **7**(6), pp. 771–782.
[45] Abraham, A. C., Moyer, J. T., Villegas, D. F., Odegard, G. M., and Haut Donahue, T. L., 2011, "Hyperelastic properties of human meniscal attachments.," J. Biomech., **44**(3), pp. 413–8.
[46] Calvo, B., Ramírez, A., Alonso, A., Grasa, J., Soteras, F., Osta, R., and Muñoz, M. J., 2010, "Passive nonlinear elastic behaviour of skeletal muscle: Experimental results and model formulation," J. Biomech., **43**(2), pp. 318–325.
[47] Peña, E., Calvo, B., Martínez, M. A., and Doblaré, M., 2006, "A three-dimensional finite element analysis of the combined behavior of ligaments and menisci in the healthy human knee joint.," J. Biomech., **39**(9), pp. 1686–701.
[48] Weiss, J. A., Maker, B. N., and Govindjee, S., 1996, "Finite element implementation of incompressible, transversely isotropic hyperelasticity," Comput. Methods Appl. Mech. Eng., **135**(1–2), pp. 107–128.
[49] Wheatley, B. B., Fischenich, K. M., Button, K. D., Haut, R. C., and Haut Donahue, T. L., 2015, "An optimized transversely isotropic, hyper-poro-viscoelastic finite element model

of the meniscus to evaluate mechanical degradation following traumatic loading.," J. Biomech., **48**(8), pp. 1454–60.
[50] Ateshian, G. A., Rajan, V., Chahine, N. O., Canal, C. E., and Hung, C. T., 2009, "Modeling the matrix of articular cartilage using a continuous fiber angular distribution predicts many observed phenomena.," J. Biomech. Eng., **131**(6), p. 61003.
[51] Olsen, S., and Oloyede, A., 2002, "A Finite Element Analysis Methodology for Representing the Articular Cartilage Functional Structure," Comput. Methods Biomech. Biomed. Engin., **5**(6), pp. 377–386.
[52] Grasa, J., Ramírez, a, Osta, R., Muñoz, M. J., Soteras, F., and Calvo, B., 2011, "A 3D active-passive numerical skeletal muscle model incorporating initial tissue strains. Validation with experimental results on rat tibialis anterior muscle.," Biomech. Model. Mechanobiol., **10**(5), pp. 779–87.
[53] Oomens, C. W. J., Maenhout, M., van Oijen, C. H., Drost, M. R., and Baaijens, F. P., 2003, "Finite element modelling of contracting skeletal muscle.," Philos. Trans. R. Soc. Lond. B. Biol. Sci., **358**(1437), pp. 1453–60.
[54] Mow, V., Gibbs, M., and Lai, W., 1989, "Biphasic indentation of articular cartilage—II. A numerical algorithm and an experimental study," J. Biomech., **22**(8/9), pp. 853–861.
[55] Mow, V., Holmes, M., and Lai, W. M., 1984, "Fluid transport and mechanical properties of articular cartilage: a review.," J. Biomech., **17**(5), pp. 377–94.
[56] Warner, M. D., Taylor, W. R., and Clift, S. E., 2001, "Finite element biphasic indentation of cartilage: A comparison of experimental indenter and physiological contact geometries," Proc. Inst. Mech. Eng. Part H J. Eng. Med., **215**(5), pp. 487–496.
[57] Li, L. P., Herzog, W., Korhonen, R. K., and Jurvelin, J. S., 2005, "The role of viscoelasticity of collagen fibers in articular cartilage: Axial tension versus compression," Med. Eng. Phys., **27**(1), pp. 51–57.
[58] Einat, R., and Yoram, L., 2009, "Recruitment viscoelasticity of the tendon.," J. Biomech. Eng., **131**(11), p. 111008.
[59] Yin, L., and Elliott, D. M., 2004, "A biphasic and transversely isotropic mechanical model for tendon:," J. Biomech., **37**(6), pp. 907–916.
[60] Maas, S. A., Ellis, B. J., Ateshian, G. A., and Weiss, J. A., 2012, "FEBio: finite elements for biomechanics.," J. Biomech. Eng., **134**(1), p. 11005.
[61] Troyer, K. L., Estep, D. J., and Puttlitz, C. M., 2012, "Viscoelastic effects during loading play an integral role in soft tissue mechanics.," Acta Biomater., **8**(1), pp. 234–43.
[62] Wheatley, B. B., Odegard, G. M., Kaufman, K. R., and Haut Donahue, T. L., 2016, "Skeletal muscle permeability: direct experimental evaluation and modeling implications," Summer Biomechanics, Bioengineering, and Biotransport Conference, National Harbor, pp. 232–233.
[63] Lieber, R. L., Leonard, M. E., Brown, C. G., and Trestik, C. L., 1991, "Frog semitendinosis tendon load-strain and stress-strain properties during passive loading.," Am. J. Physiol., **261**(1 Pt 1), pp. C86-92.
[64] Azizi, E., and Roberts, T. J., 2009, "Biaxial strain and variable stiffness in aponeuroses.," J. Physiol., **587**(Pt 17), pp. 4309–18.
[65] Monti, R. J., 2003, "Mechanical properties of rat soleus aponeurosis and tendon during variable recruitment in situ," J. Exp. Biol., **206**(19), pp. 3437–3445.
[66] Gras, L. L., Mitton, D., Viot, P., and Laporte, S., 2012, "Hyper-elastic properties of the human sternocleidomastoideus muscle in tension," J. Mech. Behav. Biomed. Mater., **15**,

pp. 131–140.
[67] Spyrou, L. a., and Aravas, N., 2011, “Muscle and Tendon Tissues: Constitutive Modeling and Computational Issues,” J. Appl. Mech., **78**(4), p. 41015.
[68] Yucesoy, C. A., Koopman, B. H. F. J. M., Huijing, P. A., and Grootenboer, H. J., 2002, “Three-dimensional finite element modeling of skeletal muscle using a two-domain approach: linked fiber-matrix mesh model.,” J. Biomech., **35**(9), pp. 1253–62.
[69] Lu, Y. T., Zhu, H. X., Richmond, S., and Middleton, J., 2010, “A visco-hyperelastic model for skeletal muscle tissue under high strain rates,” J. Biomech., **43**(13), pp. 2629–2632.
[70] Khodaei, H., Mostofizadeh, S., Brolin, K., Johansson, H., and Osth, J., 2013, “Simulation of active skeletal muscle tissue with a transversely isotropic viscohyperelastic continuum material model.,” Proc. Inst. Mech. Eng. H., **227**(5), pp. 571–80.
[71] Sandino, C., McErlain, D. D., Schipilow, J., and Boyd, S. K., 2015, “The poro-viscoelastic properties of trabecular bone: a micro computed tomography-based finite element study.,” J. Mech. Behav. Biomed. Mater., **44**, pp. 1–9.
[72] Setton, L. A., Zhu, W., and Mow, V. C., 1993, “The biphasic poroviscoelastic behavior of articular cartilage: Role of the surface zone in governing the compressive behavior,” J. Biomech., **26**(4–5), pp. 581–592.
[73] Mansour, J. M., and Mow, V. C., 1976, “The permeability of articular cartilage under compressive strain and at high pressures.,” J. Bone Joint Surg. Am., **58**(4), pp. 509–16.
[74] LeRoux, M. A., and Setton, L. A., 2002, “Experimental and biphasic FEM determinations of the material properties and hydraulic permeability of the meniscus in tension.,” J. Biomech. Eng., **124**(3), pp. 315–21.
[75] Ateshian, G. A., and Costa, K. D., 2009, “A frame-invariant formulation of Fung elasticity,” J. Biomech., **42**(6), pp. 781–785.
[76] Fung, Y. C. (Yuan-cheng), 1993, Biomechanics : mechanical properties of living tissues, Springer-Verlag.
[77] Fung, Y. C., Fronek, K., and Patitucci, P., 1979, “Pseudoelasticity of arteries and the choice of its mathematical expression.,” Am. J. Physiol., **237**(5), pp. H620-31.
[78] Haut Donahue, T. L., Hull, M. L., Rashid, M. M., and Jacobs, C. R., 2002, “A finite element model of the human knee joint for the study of tibio-femoral contact.,” J. Biomech. Eng., **124**(3), p. 273.
[79] Spencer, A. J. M., 1971, “Part III - Theory of Invariants,” Continuum Physics, Academic Press, London, pp. 239–353.
[80] Nie, X., Cheng, J.-I., Chen, W. W., and Weerasooriya, T., 2011, “Dynamic Tensile Response of Porcine Muscle,” J. Appl. Mech., **78**(2), p. 21009.

CHAPTER 6:

MODELING SKELETAL MUSCLE STRESS AND INTRAMUSCULAR PRESSURE: A WHOLE MUSCLE ACTIVE-PASSIVE APPROACH

6.1 Introduction

Healthy skeletal muscle provides stabilization and locomotion for the human body. The robust contractile function and complex mechanical behavior are driven by the active and passive properties and structure of skeletal muscle [1,2]. Skeletal muscle structure facilitates force transmission from contractile muscle fibers to the skeletal system [3]. Thus, understanding the physiological role of skeletal muscle requires studying muscle function as both a contractile tissue and a passive structure.

In the case of skeletal muscle, a validated finite element model could provide the necessary correlation between muscle force and intramuscular pressure (IMP), thus enabling pressure microsensors to estimate muscle force. Previously, a finite element model of skeletal muscle was developed which accurately predicted both muscle force as well as intramuscular pressure under passive stretch [4]. This model characterized the complex passive response of the tissue by incorporating hyperelasticity, viscoelasticity, poroelasticity, and anisotropy. This work presents further development of this muscle model to incorporate muscle activation through inhomogeneity and validation of IMP under active conditions. The goals of this work were to identify how fluid pressurization is distributed within active skeletal muscle to potentially

identify ideal microsensor insertion location and to gain further insight into what conditions dictate this pressurization.

6.2 Methods

6.2.1 Experiment

Experiments and detailed analyses are currently under peer review [5]. Briefly, eight New Zealand White Rabbit muscles (n=8) were passively stretched and stimulated under isometric conditions at a total of fifteen different muscle lengths. Experiments were conducted on anesthetized animals with the approval of the University of California San Diego Institutional Animal Use and Care Committee by isolating and attaching the distal tibialis anterior tendon to an actuator and load cell. Active isometric contraction involved maximal stimulation of the peroneal nerve. Muscle stress was calculated as force measured by the load cell from stretch or activation divided by the physiological cross sectional area [6]. Intramuscular pressure was measured with pressure microsensors [7] inserted into the muscle midbelly in two orientations: in the longitudinal direction (parallel to muscle fibers) and in the transverse direction (perpendicular to muscle fibers).

6.2.2 Constitutive Model

6.2.2.1 Skeletal Muscle

Two similar constitutive models were simultaneously utilized for skeletal muscle in this study, representing the components of the tissue which are “excitable” but still support passive loads and those that are only able to support passive loads (“passive”). As the tissue-level passive properties of skeletal muscle are attributed to both the active actin-myosin complex [8–10], and

the extracellular matrix [11,12], it is difficult to elucidate exactly how to assign properties to these constituents. Thus, for both previous modelling efforts [4] and the current model, the passive responses from the extracellular matrix and contractile elements are coupled. Previously, passive skeletal muscle was modeled as a hyper-visco-poroelastic material with an anisotropic compressible solid phase [4]. For the current model, the assumption was made that the excitable constituent did not contain a fluid component. Thus, the constitutive approach for the excitable and the passive constituents is very similar, with the only exception being that the excitable constituent did not include poroelasticity. Thus, it is assumed that the contractile tissue is comprised of solid material only, and the excitable constituent was a compressible hyper-viscoelastic material [13–16], while passive was modeled as compressible hyper-visco-poroelastic material [17].

While the full constitutive approach has been previously outlined [4], in brief, an isotropic, compressible (or coupled) Mooney-Rivlin strain energy density function was utilized for the ground matrix [18] and viscoelastic effects were modeled using a three-term Prony series [19]. Tensile anisotropic and nonlinear properties of passive muscle were largely dictated by three-dimensional tension-only reinforcing fibers with an ellipsoidal fiber distribution (EFD) [20]. Previously, the longitudinal EFD properties were optimized to experimental data and the transverse EFD parameters were fixed based on the assumption of an increase in modulus of one order of magnitude over longitudinal properties [21]. While this formulation yielded excellent model validation to both muscle stress and intramuscular pressure under passive conditions [4], they were altered in this study for improved agreement with experimental data under both

passive and active conditions. A constant, isotropic hydraulic permeability was assumed based on prior experimental and finite element analysis of skeletal muscle [17].

Table 6-1. Constitutive model parameter values for skeletal muscle. Note that the excitable and passive constituent have the same constitutive model and parameters with the exception of poroelasticity, which was only utilized for the passive constituent.

Mooney-Rivlin SED			**Prony Series Viscoelasticity**		**Ellipsoidal Fiber Distribution**				**Permeability (mm^4/N-s) (passive)**
c_1 **(kPa)**	c_2 **(kPa)**	k **(kPa)**	g_i **(-)**	τ_i **(s)**	ξ_{long} **(kPa)**	β_{long} **(-)**	ξ_{trans} **(kPa)**	β_{trans} **(-)**	
0.05	0.5	5	1.33, 0.476, 0.295, 0.167	0.1, 1, 10, 100	Optim	Optim	15	3	0.074

The total stress within a biphasic finite element model which includes an active component can be decomposed into active stress $\boldsymbol{\sigma}^{active}$, passive stress within the porous solid $\boldsymbol{\sigma}^{solid}$, and fluid pressure p (Equation 1, where $\boldsymbol{I}$ is the identity matrix). Muscle activation was modeled using prescribed uniaxial contraction (Equation 2) [22]. Here J is the Jacobian or volume ratio, T_0 is the maximum activation stress, $c(t)$ is a load curve which defines the stress as a function of time, and $\boldsymbol{n}$ is the unit vector which dictates the direction of active contraction, which is the physiological pennation angle. The load curve $c(t)$ was chosen to replicate the increase of force of fully fused isometric skeletal muscle [2].

$$\boldsymbol{\sigma}^{total} = \boldsymbol{\sigma}^{active} + \boldsymbol{\sigma}^{solid} - p\boldsymbol{I} \tag{1}$$

$$\boldsymbol{\sigma}^{active} = J^{-1}T_0 c(t)\boldsymbol{n} \otimes \boldsymbol{n} \tag{2}$$

6.2.2.2 Aponeurosis and Tendon

Aponeurosis and tendon were modeled as nearly incompressible hyper-viscoelastic with a transversely isotropic Mooney-Rivlin strain energy function [23] and a Prony series viscoelastic formulation [24] (Table 6-2). This formulation is outlined in greater detail in [4].

Table 6-2. Constitutive model parameter values for tendon/aponeurosis. These parameters are identical to previously utilized values [4].

Mooney-Rivlin SED							**Prony Series Viscoelasticity**	
c_1 **(kPa)**	c_2 **(kPa)**	k **(kPa)**	c_4 **(-)**	c_5 **(kPa)**	λ_{max} **(-)**	k **(kPa)**	g_i **(-)**	τ_i **(s)**
10000	500	50	40	100000	1.03	500000	0.203, 0.133, 0.191	0.33, 47.5, 2500

6.2.3 Finite Element Model

To represent the longitudinal contractile structure of skeletal muscle, inhomogeneous geometry of the New Zealand White Rabbit tibialis anterior and the human tibialis anterior were developed. The excitable and passive components of the tissue were connected directly through mesh structure, along with aponeurosis and tendon tissue. Thus, no boundary contact conditions were necessary between these three constituents. As skeletal muscle is comprised of roughly 80% fluid [25], the excitable constituent was assumed to be approximately 20% of the total volume of the tissue. As the mesh is comprised of solely hexahedral elements, this was achieved by denoting one of out every five longitudinal string of elements as excitable (Figure 6-1).

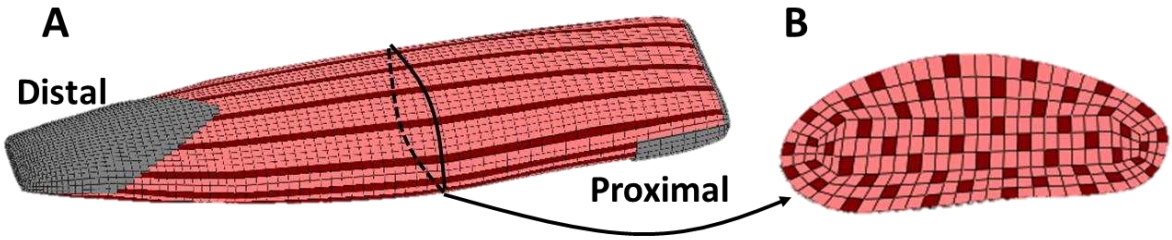

Figure 6-1. Inhomogeneous finite element geometry of skeletal muscle, showing excitable (dark red), passive (light red), and aponeurosis/tendon (gray). A) Whole New Zealand White Rabbit tibialis anterior muscle model and B) cross sectional view of the rabbit tibialis anterior model.

The finite element geometry for the rabbit tibialis anterior is outlined elsewhere [4], but in short it was developed by segmentation and hexahedral meshing of μCT images of an *in vitro* New Zealand White Rabbit tibialis anterior. The pennation angle of 2.5° [6] was applied globally by specifying the orientation of the constitutive model. Stress was calculated by summing the total reaction force at the distal nodes and dividing by physiological cross sectional area of the model. This approach was the same for both active isometric and passive conditions. Model pressure was calculated as fluid pressure from 90 midbelly elements of the passive constituent. Again, this output did not change between active and passive simulations. The muscle mesh utilized in this study (18646 elements) was compared against a denser mesh (46400 elements) under active isometric conditions to ensure mesh density convergence. Isometric activation was simulated using an active stress of 500 kPa (T_0 from Equation 2, determined based on applied active stress from the results) for the denser mesh and for the same reaction force using the less dense mesh, only a 0.80% difference of mean fluid pressure between the two models was observed at $t = 0.5$ seconds.

6.2.4 Verification of Transverse Stiffness Parameters

To investigate the role of transverse fiber stiffness in model behavior, with an emphasis on fluid pressure, variations in transverse ellipsoidal fiber distribution (EFD) parameters were applied. The model stiffness is largely dictated by these tension-only EFD parameters by design, as skeletal muscle tensile stiffness is roughly two orders higher in tension versus compression [21,26–29]. While the longitudinal fiber parameters were determined through nonlinear optimization, the transverse parameters were not specifically fit to experimental data. Previous finite element modeling of passively stretched muscle utilized a value of ~33kPa for ξ_{trans} based on the assumption of the transverse orientation being one order of stiffness higher than the longitudinal [4]. However, the reported values for transverse tensile linear modulus of skeletal muscle from literature range from roughly 20 kPa to nearly 800 kPa [21,30]. Additionally, there remains uncertainty to the role of transverse stiffness in model fluid pressurization. To study this, a direct comparison of model behavior was made between two ξ_{trans} parameter values: 33 kPa from the previous study and 15 kPa utilized in this study.

A simplified finite element geometry of 2560 cubic hexahedral elements using the same inhomogeneous nature as presented in Figure 6-1 was developed to compare model behavior to experimentally analyzed excised muscle samples [21]. The mean Cauchy stress in the direction of elongation (transverse) was compared to the experimentally calculated Cauchy stress. Experimental samples underwent 0.1 tensile strain at a rate of 0.1 s^{-1} followed by a 300 second relaxation period, and finally a constant rate pull step to 0.25 tensile strain at 0.01 s^{-1}. While this highlighted differences in parameter agreement to specific experimental data, the goal of this work was to identify how these values affect fluid pressurization within the model. The above

whole muscle finite element model was thus employed with each of these two parameters under active contraction at three muscle lengths to investigate the role of transverse stiffness in model fluid pressure. The three lengths include one on the ascending limb (-0.2 fiber strain from optimal length), optimal length, and one on the descending limb (0.2 fiber strain from optimal length). The specified contractile internal stress (Equation 2) will remain the same for both conditions, although changes to the constitutive approach may result in differences in reaction force at the model boundary.

6.2.5 Optimization and Validation

To ensure that passive model behavior was still consistent with passive experimental data following changes to the constitutive model and geometry, the same optimization approach [4] was used to generate ξ_{long} and β_{long} parameters. In short, the model stress was fit to the passive experimental stress at increments of 5% fiber strain over a total of eleven points and the model pressure was compared against experimental data.

Active isometric stress from the FE model was optimized to experimental data by varying the T_0 parameter from Equation 2. This was done for each of the fifteen experimental data points under active isometric contraction. For each fit, the muscle was passively stretched to the corresponding experimental length followed by 300 seconds of relaxation to reach steady-state [19,31] before activation was applied per the activation curve. Active model stress and fluid pressure were calculated by subtracting the steady-state stress and fluid pressure values from the maximum stress and pressure during contraction. Experimental and model pressures were compared for an independent validation. Statistical analysis of agreement between model outputs

and experimental data were completed by calculating the root mean square error (RMSE, Equation 3, where y^e are experimental data and y^m are model data) and normalized root mean square error (NRMSE, Equation 4).

$$RMSE = \sqrt{\frac{\sum_{i=1}^{15}(y_i^e - y_i^m)^2}{15}} \quad (3)$$

$$NRMSE = \frac{RMSE}{max(y^e) - min(y^e)} \quad (4)$$

6.3 Results

The optimized passive parameters for longitudinal EFD properties showed a highly nonlinear longitudinal stiffness, which is consistent with previous investigations of skeletal muscle longitudinal tensile behavior [19,21,28,32,33] (Table 6-3). Optimized applied stress (T_0 from Equation 2) in the excitable constituent for isometric activation varied for each data point and ranged from 229 to 604 kPa. These values were expected to be higher than the whole muscle specific tension as the excitable constituent comprises only a fraction of the total muscle volume.

Table 6-3. Optimized longitudinal ellipsoidal fiber distribution (EFD) parameters.

Ellipsoidal Fiber Distribution	
ξ_{long} **(kPa)**	β_{long} **(-)**
2.76	10.9

Model optimization to experimental stress data under both active and passive conditions was confirmed visually (Figure 6-2A and 2D) and resulted in small statistical error values (NRMSE values less than 1%, Table 6-4). The model was able to match experimental intramuscular pressure readings under passive tension for both the longitudinal and transverse sensor insertion directions by visual analysis (Figure 6-2B, 3C) and through statistical measures (~5-10%

NRMSE, Table 6-4). Under isometric active conditions, the model produced superior statistical agreement with experimental intramuscular pressure data with the longitudinal sensor insertion (NRMSE of 48%) in comparison to transverse orientation (NRMSE of 115%). Visually, model pressures decreased with increasing stretch similar to transverse sensor insertion, while longitudinal sensor insertion did not exhibit this trend (Figure 6-2E and 2F). The model agreement with transverse data was stronger at muscle lengths which occur *in vivo* (Figure 6-2E inset, NRMSE of 37%) in comparison to longitudinal data (Figure 6-2F, NRMSE of 111%) [34,35].

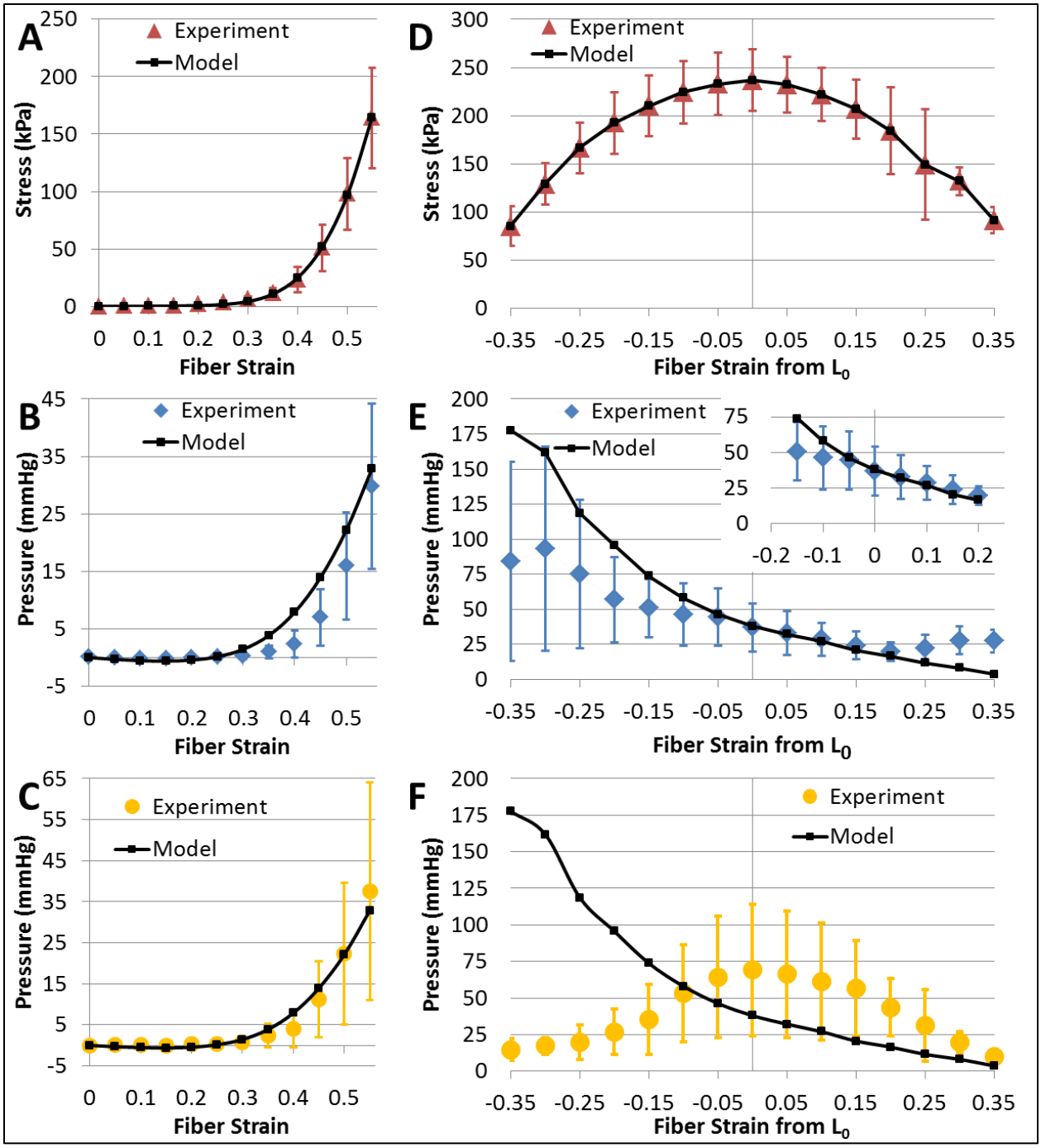

Figure 6-2. A) Model fit to experimental stress under passive stretch conditions. The corresponding passive experimental and model predictions for intramuscular pressure are shown for B) longitudinal sensor insertion and C) transverse sensor insertion. D) Model fit to experimental stress under active isometric conditions. The corresponding active experimental and model prediction for intramuscular pressure are shown for E) longitudinal sensor insertion and F) transverse sensor insertion. Physiological *in vivo* muscle lengths are highlighted in the top right inset of E, showing model predictive capabilities. All experimental data presented as mean and standard deviation.

Table 6-4. Statistical analysis of model agreement to experimental data of sensor insertion in the longitudinal or transverse orientations. Root mean square error (RMSE, Equation 3) and normalized root mean square error (NRMSE, Equation 4). Note that for passive and active stress the model was fit to experimental data (hence the smaller errors) and that all pressure comparisons are independent validation.

Statistic	Insertion	Passive Stress (kPa)	Passive Pressure (mmHg)	Active Stress (kPa)	Active Pressure (mmHg)
RMSE	**Longitudinal**	1.26	3.53	0.119	35.3
	Transverse		2.12		68.2
NRMSE	**Longitudinal**	0.765%	11.7%	0.0786%	48.1%
	Transverse		5.64%		115%

Intramuscular pressure exhibited inhomogeneity within the model (Figure 6-3). Fluid pressure was highly transient in the distal region (which has a larger aponeurosis), which had pressure gradients of nearly 100 mmHg across less than 15 mm (Figure 6-3A). While the proximal region also exhibited pressure gradients, they was not as drastic (Figure 6-3B, ranging from 0 mmHg to ~30 mmHg). Fluid pressure gradients decreased with time as pressure equilibrated.

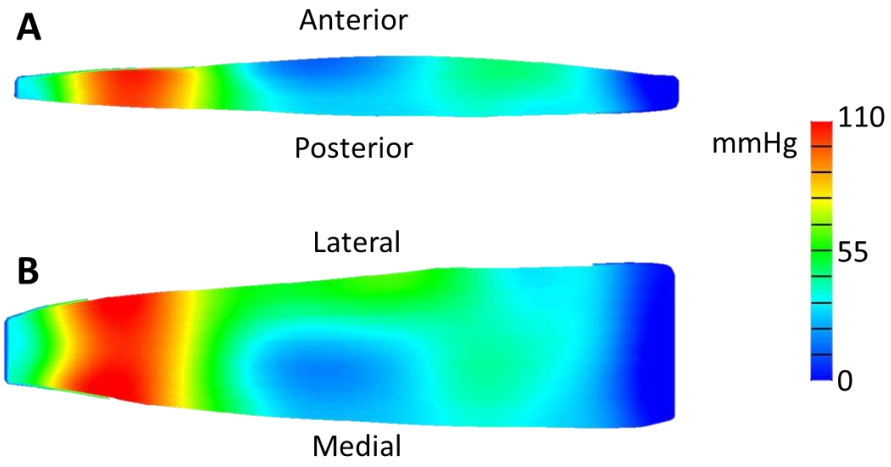

Figure 6-3. Color maps of fully activated finite element model at optimal length after one second of maximum contraction. A) Image of two dimensional sagittal midbelly slice of the model showing fluid pressure distribution. B) Image of two dimensional coronal midbelly slice showing fluid pressure distribution. The distal region exhibited the highest variability in fluid pressure.

The transverse stiffness parameter comparison showed that current modeling approaches (a value of 15 kPa for ξ_{trans}) had a stronger agreement to experimental tensile stress data than previous

approaches (33 kPa for ξ_{trans}) (Figure 6-4). This was observed both under stress relaxation (Figure 6-4A) (NRMSE of 3.8% for the current approach versus 22% for the previous approach) as well as constant rate pull (Figure 6-4B) (NRMSE of 8.3% for current versus 26% for previous). Additionally, transverse parameter stiffness affected fluid pressurization within the model under active contraction, particularly at short muscle lengths. Specifically, increases in transverse stiffness lead to increases in fluid pressure in excess of 20% on the ascending limb for the same active stress generation (Table 6-5).

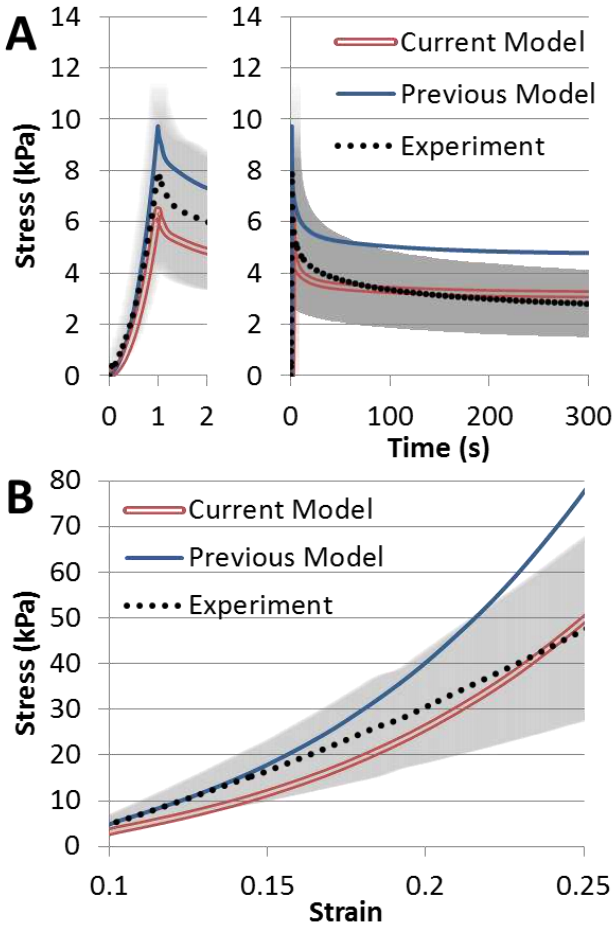

Figure 6-4. Comparison of two models to experimental data (mean with standard deviation in gray) of rabbit tibialis anterior muscle subject to transverse extension. The current model assumes a ξ_{trans} value of 15 kPa while previous modeling utilized 33 kPa. A) Stress relaxation step of 0.1 strain ramp (shown left) and 300 seconds of relaxation (shown right). B) Constant rate pull to 0.25 strain at a rate of 0.01 s^{-1}.

Table 6-5. Comparison between the previous modeling approach (ξ_{trans} of 33 kPa) and current approach (ξ_{trans} of 15 kPa) at three muscle lengths: the ascending limb (strain of -0.2), optimal length (zero strain), and the descending limb (strain of 0.2). Fluid pressure increased with increases in transverse stiffness, particularly on the ascending limb, yet measured whole model stress had only little dependence on transverse stiffness.

Strain from L_0	Stress (kPa)				Pressure (mmHg)			
	Exp	Current Model	Previous Model	Model % Difference	Exp	Current Model	Previous Model	Model % Difference
-0.2	192	192	190	1.1%	56.7	95.6	117	23%
0	237	237	236	0.19%	36.8	38.0	40.3	6.0%
0.2	184	184	184	0.17%	19.6	16.5	17.2	4.2%

6.4 Discussion

This work presents the first whole muscle finite element model to accurately predict both intramuscular pressure and muscle stress under active contraction conditions. Previous modeling efforts either did not include activation [4] or used an idealized 2D geometry and lacked time dependent effects [36]. This work has developed the foundation for future endeavors to evaluate intramuscular pressure distributions within skeletal muscle, study how disease and degradation affect muscle force and intramuscular pressure, and how variations in geometry or activation affect force and IMP. Based on the agreement with experimental data, this work suggests use of sensors inserted longitudinally in contrast to a transverse insertion. Although the NRMSE error value of 48% for longitudinal active data may seem quite high, experimental standard deviations are similarly ~50%. Additionally, the model showed excellent predictive capability for data from -0.15 to 0.2 strain (Figure 6-2E inset), which are muscle lengths likely experienced *in vivo* [34]. While it remains unclear exactly why the IMP data in this study differs based on sensor insertion technique, it is likely the result of anchoring within the tissue, which is critical to proper sensor utilization [7].

The inhomogeneous approach in this work was chosen based on the portion of tissue comprised of solid muscle fibers in contrast to extracellular matrix and fluid content [25,37]. Previous finite element modeling efforts of skeletal muscle have utilized similar three dimensional inhomogeneous assumptions about contractile constituents [38,39], homogeneous assumptions [13,16,23,36,40–45], and a combination of three dimensional and one dimensional elements [35,46,47]. While the approach used in this work clearly does not replicate the complete structure of skeletal muscle, it does provide further insight into the inhomogeneous behavior of the tissue, particularly for intramuscular pressure (Figure 6-3). While it remains to be seen exactly how other approaches, such as a passive three-dimensional mesh reinforced with one-dimensional contractile elements are able to model intramuscular pressure behavior, this current approach shows strong predictive capabilities, especially in the physiological range of strain. Future work to investigate the role of muscle weakness, fibrosis, fatigue, and isotonic contractions on fluid pressurization would benefit the IMP field.

Model fluid pressure exhibited a high level of spatial dependence during immediate contraction (Figure 6-3). While this variability decreased with time even during contraction, the combination of transience and inhomogeneity manifests in a highly dynamic pressure distribution. This could support previous experimental findings noting the difficulty with repeatability of intramuscular pressure measurements [48], particularly under dynamic conditions when sensor movement occurs [49]. Under steady-state conditions, fluid can equilibrate and thus the model pressure distribution is more uniform. However, it remains unclear if this modeling observation is physiologically accurate, as current experimental intramuscular pressure studies do not provide the necessary spatial measurements to correlate with a finite element model. Future work to

experimentally investigate regional IMP in muscle simultaneously would provide valuable insight into this spatial fluid distribution and provide strong validation data for this model. Additionally, dynamic muscle conditions are critical to proper *in vivo* function [2] and thus should not be neglected for the sake of simplicity.

The length-dependency of the model fluid pressure output suggests that variability of intramuscular pressure may *in vivo* may be dependent on more physiological conditions than muscle force alone. Additionally, the transverse stiffness of the model affects fluid pressurization under active conditions (Table 6-5). From a modeling perspective, it is not surprising that the fluid pressure behaves in such a manner. When muscle is passively stretched, the transverse direction compresses due to the Poisson effect, which results in fluid pressurization. When muscle actively contracts, the transverse direction expands, again due to the Poisson effect. In this case, the longitudinal compression causes fluid pressurization. Thus, these two conditions enact opposing deformations as a result of the Poisson effect, which when combined result in a small volumetric deformation (Figure 6-5). From a modeling perspective, as the muscle is lengthened, contraction must overcome larger and larger deformations to pressurize the fluid. Thus, the observed decrease in fluid pressure with muscle stretch is expected within a finite element model of continuum muscle. Further experimental work to identify exactly how muscle length and activation level contribute to intramuscular pressure readings would elucidate the accuracy of this modeling approach.

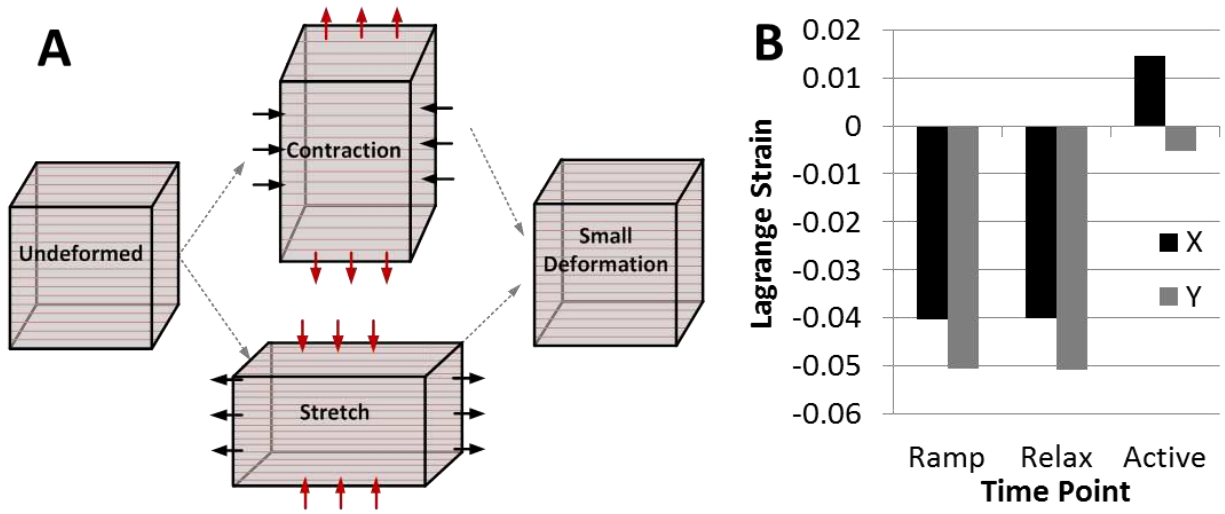

Figure 6-5. A) The deformations resulting from passive stretch and active contraction both enact the Poisson effect, where the longitudinal strain (black arrows) results in opposite strain in the transverse plane (red arrows). As these deformations oppose each other, the result is a smaller final volumetric deformation, which results in low fluid pressurization. B) Model transverse strains (x and y directions, as elongation occurs in the z direction) for three time points when stretched to optimal length, after initial ramp elongation, at the end of stress relaxation, and at maximum contraction. Passive elongation results in negative transverse strains, which is then counteracted by shortening due to active contraction.

While passive stretch of *in vitro* whole skeletal muscle is largely dictated by longitudinal mechanical properties, *in vivo* muscle fibers are connected through fascia to surrounding muscle fibers and other tissues. As a result, force generation is transmitted laterally throughout skeletal muscle [3]. Thus, while the transverse tensile properties play a limited role in *in vitro* passive muscle stiffness, they contribute to the mechanical function of skeletal muscle *in vivo*. From a modeling perspective, the transverse tensile stiffness also plays a key role in fluid pressurization (Table 6-5). This was particularly evident on the ascending limb when muscle is at short lengths, as there is no pre-stretch to overcome and thus transverse tensile strains are larger. Stiffer fibers would result in less expansion and thus more fluid pressurization. However, at longer muscle lengths the role of transverse stiffness seems to be less important to fluid pressurization (Table 6-5). This appears to be due to the fact that contraction must "overcome" stretch to pressurize fluid

(Figure 6-5), resulting in small transverse tensile strains and thus less of a contribution from the transverse fibers. The agreement between experiment and model data for transverse muscle stiffness (Figure 6-4) is thus critical for future applications of this work to *in vivo* modeling and to the use of this model for clinical recommendations.

6.5 Conclusions

This work presents the first whole muscle finite element model of skeletal muscle which predicts both intramuscular pressure and muscle force. This work also modeled active skeletal muscle with a hyper-poro-viscoelastic constitutive approach, utilized inhomogeneity, and confirmed physiological accuracy in regards to choosing parameter values. Muscle stress and intramuscular pressure data under passive and active conditions were modeled, and the use of a pressure microsensor inserted longitudinally into skeletal muscle was suggested. The transverse tensile stiffness was shown to play a key role in fluid pressurization at short muscle length. At longer lengths, passive stretch and muscle contraction enacted opposing Poisson effects, which led to low fluid pressurizations. Future use of this model to study spatial distribution of fluid pressure within skeletal muscle will guide the clinical use of the pressure microsensors for accurately measuring intramuscular pressure. Further model development to include more complex muscle activation as well as the effects of muscle weakness or disease would also be highly beneficial.

REFERENCES

[1] Hill, A. V., 1938, “The Heat of Shortening and the Dynamic Constants of Muscle,” Proc. R. Soc. B Biol. Sci., **126**(843), pp. 136–195.

[2] Lieber, R. L., 2010, Skeletal Muscle Structure, Function, and Plasticity, Lippincott Williams and Wilkins, Philadelphia, PA.

[3] Huijing, P. A., 1999, “Muscle as a collagen fiber reinforced composite: A review of force transmission in muscle and whole limb,” J. Biomech., **32**(4), pp. 329–345.

[4] Wheatley, B. B., Odegard, G. M., Kaufman, K. R., and Haut Donahue, T. L., 2016, “A validated model of passive skeletal muscle to predict force and intramuscular pressure,” Biomech. Model. Mechanobiol., pp. 1–12.

[5] O’Connor, S. M., Kaufman, K. R., Ward, S. R., and Lieber, R. L., “Intramuscular pressure correlates with muscle tension in rabbit tibialis anterior,” Rev.

[6] Lieber, R. L., and Blevins, F. T., 1989, “Skeletal muscle architecture of the rabbit hindlimb: functional implications of muscle design.,” J. Morphol., **199**(1), pp. 93–101.

[7] Go, S. A., Jensen, E. R., O’Connor, S. M., Evertz, L. Q., Morrow, D. A., Ward, S. R., Lieber, R. L., and Kaufman, K. R., 2017, “Design Considerations of a Fiber Optic Pressure Sensor Protective Housing for Intramuscular Pressure Measurements,” Ann. Biomed. Eng., **45**(3), pp. 739–746.

[8] Wang, K., McCarter, R., Wright, J., Beverly, J., and Ramirez-Mitchell, R., 1993, “Viscoelasticity of the sarcomere matrix of skeletal muscles. The titin-myosin composite filament is a dual-stage molecular spring.,” Biophys. J., **64**(4), pp. 1161–77.

[9] Meyer, G. A., McCulloch, A. D., and Lieber, R. L., 2011, “A Nonlinear Model of Passive Muscle Viscosity,” J. Biomech. Eng., **133**(9), p. 91007.

[10] Proske, U., and Morgan, D. L., 1999, “Do cross-bridges contribute to the tension during stretch of passive muscle?,” J. Muscle Res. Cell Motil., **20**(5–6), pp. 433–42.

[11] Gillies, A. R., and Lieber, R. L., 2011, “Structure and function of the skeletal muscle extracellular matrix.,” Muscle Nerve, **44**(3), pp. 318–31.

[12] Meyer, G. A., and Lieber, R. L., 2011, “Elucidation of extracellular matrix mechanics from muscle fibers and fiber bundles,” J. Biomech., **44**(4), pp. 771–773.

[13] Hodgson, J. a, Chi, S.-W., Yang, J. P., Chen, J.-S., Edgerton, V. R., and Sinha, S., 2012, “Finite element modeling of passive material influence on the deformation and force output of skeletal muscle.,” J. Mech. Behav. Biomed. Mater., **9**, pp. 163–83.

[14] Yucesoy, C. A., Koopman, B. H. F. J. M., Huijing, P. A., and Grootenboer, H. J., 2002, “Three-dimensional finite element modeling of skeletal muscle using a two-domain approach: linked fiber-matrix mesh model,” J. Biomech., **35**(9), pp. 1253–1262.

[15] Clemen, C. B., Benderoth, G. E. K., Schmidt, A., Hübner, F., Vogl, T. J., and Silber, G., 2017, “Human skeletal muscle behavior in vivo: Finite element implementation, experiment, and passive mechanical characterization,” J. Mech. Behav. Biomed. Mater., **65**, pp. 679–687.

[16] Oomens, C. W. J., Maenhout, M., van Oijen, C. H., Drost, M. R., and Baaijens, F. P., 2003, “Finite element modelling of contracting skeletal muscle.,” Philos. Trans. R. Soc.

Lond. B. Biol. Sci., **358**(1437), pp. 1453–60.
[17] Wheatley, B. B., Odegard, G. M., Kaufman, K. R., and Haut Donahue, T. L., 2016, "A case for poroelasticity in skeletal muscle finite element analysis: experiment and modeling.," Comput. Methods Biomech. Biomed. Engin., pp. 1–4.
[18] Johansson, T., Meier, P., and Blickhan, R., 2000, "A finite-element model for the mechanical analysis of skeletal muscles.," J. Theor. Biol., **206**(1), pp. 131–49.
[19] Wheatley, B. B., Morrow, D. A., Odegard, G. M., Kaufman, K. R., and Haut Donahue, T. L., 2016, "Skeletal muscle tensile strain dependence: Hyperviscoelastic nonlinearity.," J. Mech. Behav. Biomed. Mater., **53**, pp. 445–54.
[20] Ateshian, G. A., Rajan, V., Chahine, N. O., Canal, C. E., and Hung, C. T., 2009, "Modeling the matrix of articular cartilage using a continuous fiber angular distribution predicts many observed phenomena.," J. Biomech. Eng., **131**(6), p. 61003.
[21] Wheatley, B. B., Odegard, G. M., Kaufman, K. R., and Donahue, T. L. H., 2016, "How does tissue preparation affect skeletal muscle transverse isotropy?," J. Biomech., **49**(13), pp. 3056–3060.
[22] Maas, S. A., Ellis, B. J., Ateshian, G. A., and Weiss, J. A., 2012, "FEBio: finite elements for biomechanics.," J. Biomech. Eng., **134**(1), p. 11005.
[23] Blemker, S. S., Pinsky, P. M., and Delp, S. L., 2005, "A 3D model of muscle reveals the causes of nonuniform strains in the biceps brachii.," J. Biomech., **38**(4), pp. 657–65.
[24] Einat, R., and Yoram, L., 2009, "Recruitment viscoelasticity of the tendon.," J. Biomech. Eng., **131**(11), p. 111008.
[25] Sjøgaard, G., and Saltin, B., 1982, "Extra- and intracellular water spaces in muscles of man at rest and with dynamic exercise.," Am. J. Physiol., **243**(3), pp. R271-80.
[26] Wheatley, B. B., Pietsch, R. B., Haut Donahue, T. L., and Williams, L. N., 2016, "Fully non-linear hyper-viscoelastic modeling of skeletal muscle in compression.," Comput. Methods Biomech. Biomed. Engin., **19**(11), pp. 1181–9.
[27] Pietsch, R., Wheatley, B. B., Haut Donahue, T. L., Gilbrech, R., Prabhu, R., Liao, J., and Williams, L. N., 2014, "Anisotropic compressive properties of passive porcine muscle tissue.," J. Biomech. Eng., **136**(11), p. 111003.
[28] Takaza, M., Moerman, K. M., Gindre, J., Lyons, G., and Simms, C. K., 2012, "The anisotropic mechanical behaviour of passive skeletal muscle tissue subjected to large tensile strain," J. Mech. Behav. Biomed. Mater., **17**, pp. 209–220.
[29] Van Loocke, M., Lyons, C. G., and Simms, C. K., 2006, "A validated model of passive muscle in compression," J. Biomech., **39**(16), pp. 2999–3009.
[30] Mohammadkhah, M., Murphy, P., and Simms, C. K., 2016, "The in vitro passive elastic response of chicken pectoralis muscle to applied tensile and compressive deformation," J. Mech. Behav. Biomed. Mater., **62**, pp. 468–480.
[31] Abraham, A. C., Kaufman, K. R., and Haut Donahue, T. L., 2012, "Phenomenological consequences of sectioning and bathing on passive muscle mechanics of the New Zealand white rabbit tibialis anterior," J. Mech. Behav. Biomed. Mater., **17**, pp. 290–295.
[32] Davis, J., Kaufman, K. R., and Lieber, R. L., 2003, "Correlation between active and passive isometric force and intramuscular pressure in the isolated rabbit tibialis anterior muscle," J. Biomech., **36**(4), pp. 505–512.
[33] Van Ee, C. A., Chasse, A. L., and Myers, B. S., 2000, "Quantifying skeletal muscle properties in cadaveric test specimens: effects of mechanical loading, postmortem time, and freezer storage.," J. Biomech. Eng., **122**(1), pp. 9–14.

[34] Burkholder, T. J., and Lieber, R. L., 2001, “Sarcomere length operating range of vertebrate muscles during movement.,” J. Exp. Biol., **204**(Pt 9), pp. 1529–36.
[35] Grasa, J., Ramírez, a, Osta, R., Muñoz, M. J., Soteras, F., and Calvo, B., 2011, “A 3D active-passive numerical skeletal muscle model incorporating initial tissue strains. Validation with experimental results on rat tibialis anterior muscle.,” Biomech. Model. Mechanobiol., **10**(5), pp. 779–87.
[36] Jenkyn, T., Koopman, B., Huijing, P. a, Lieber, R. L., and Kaufman, K. R., 2002, “Finite element model of intramuscular pressure during isometric contraction of skeletal muscle.,” Phys. Med. Biol., **47**, pp. 4043–4061.
[37] Light, N., and Champion, A. E., 1984, “Characterization of muscle epimysium, perimysium and endomysium collagens.,” Biochem. J., **219**(3), pp. 1017–1026.
[38] Lemos, R. R., Epstein, M., Herzog, W., and Wyvill, B., 2004, “A framework for structured modeling of skeletal muscle.,” Comput. Methods Biomech. Biomed. Engin., **7**(6), pp. 305–17.
[39] Yucesoy, C. A., Koopman, B. H. F. J. M., Huijing, P. A., and Grootenboer, H. J., 2002, “Three-dimensional finite element modeling of skeletal muscle using a two-domain approach: linked fiber-matrix mesh model.,” J. Biomech., **35**(9), pp. 1253–62.
[40] Khodaei, H., Mostofizadeh, S., Brolin, K., Johansson, H., and Osth, J., 2013, “Simulation of active skeletal muscle tissue with a transversely isotropic viscohyperelastic continuum material model.,” Proc. Inst. Mech. Eng. H., **227**(5), pp. 571–80.
[41] Hernández-Gascón, B., Grasa, J., Calvo, B., and Rodríguez, J. F., 2013, “A 3D electro-mechanical continuum model for simulating skeletal muscle contraction.,” J. Theor. Biol., **335**, pp. 108–18.
[42] Rehorn, M. R., and Blemker, S. S., 2010, “The effects of aponeurosis geometry on strain injury susceptibility explored with a 3D muscle model.,” J. Biomech., **43**(13), pp. 2574–81.
[43] Lu, Y. T., Zhu, H. X., Richmond, S., and Middleton, J., 2010, “A visco-hyperelastic model for skeletal muscle tissue under high strain rates,” J. Biomech., **43**(13), pp. 2629–2632.
[44] Chi, S., Hodgson, J., Chen, J., Reggie Edgerton, V., Shin, D. D., Roiz, R. A., and Sinha, S., 2010, “Finite element modeling reveals complex strain mechanics in the aponeuroses of contracting skeletal muscle.,” J. Biomech., **43**(7), pp. 1243–50.
[45] Rahemi, H., Nigam, N., and Wakeling, J. M., 2015, “The effect of intramuscular fat on skeletal muscle mechanics: implications for the elderly and obese.,” J. R. Soc. Interface, **12**(109), p. 20150365-.
[46] Böl, M., and Reese, S., 2008, “Micromechanical modelling of skeletal muscles based on the finite element method.,” Comput. Methods Biomech. Biomed. Engin., **11**(5), pp. 489–504.
[47] Tang, C. Y., Zhang, G., and Tsui, C. P., 2009, “A 3D skeletal muscle model coupled with active contraction of muscle fibres and hyperelastic behaviour.,” J. Biomech., **42**(7), pp. 865–72.
[48] Sejersted, O. M., and Hargens, A. R., 1995, “Intramuscular pressures for monitoring different tasks and muscle conditions.,” Adv. Exp. Med. Biol., **384**, pp. 339–350.
[49] Ward, S. R., Davis, J., Kaufman, K. R., and Lieber, R. L., 2007, “Relationship between muscle stress and intramuscular pressure during dynamic muscle contractions,” Muscle and Nerve, **36**(3), pp. 313–319.

CHAPTER 7:

MODELING INTRAMUSCULAR PRESSURE IN THE HUMAN TIBIALIS ANTERIOR WITH FINITE ELEMENT ANALYSIS

7.1 Introduction

The correlation between muscle force and intramuscular pressure (IMP) [1–5] provides an opportunity to utilize IMP measurements as a clinical approach to interpret muscle force *in vivo*. However, regional variations in IMP [6] and difficulties with reproducibility from muscle to muscle and patient to patient [7] make this interpretation rather difficult. It remains unclear exactly why intramuscular pressure measurements are highly variable yet still correlate strongly with muscle force. Chapter 6 presents a finite element model of the rabbit tibialis anterior which suggests sensor location and muscle length may play a role in fluid pressurization within the tissue. However, it remains to be seen if this is observed experimentally and if variations in muscle architecture, boundary conditions, and measurement location manifest in pressure variations.

Previous finite element modeling of skeletal muscle characterized both muscle stress and intramuscular pressure under active and passive conditions (Chapter 6). That work provided insight into spatial distribution of fluid pressure within the model, suggested the use of longitudinal pressure microsensor insertion, identified the role transverse stiffness plays in fluid pressure in contracting muscle, and suggested that muscle length may influence IMP. However, there is some concern in utilizing an approach developed in an animal model (New Zealand

White Rabbit tibialis anterior or TA) for human application. Additionally, it remains unclear how the developed constitutive approach can translate to muscles with variations in architecture. The New Zealand White Rabbit TA is a unipennate muscle with a low pennation angle of roughly three degrees [8]. This simplifies the geometry and force transmission from a modeling standpoint as the muscle fibers are nearly aligned with the whole muscle. The human TA, a bipennate structure is thus architecturally different from the rabbit TA in that it has both external aponeuroses and an internal tendon/aponeurosis [9]. While the constitutive approach was developed and implemented at the tissue scale, use of that model in only one muscle limits the confidence in application to human studies without further validation.

Previous fluid pressure validation was also completed for singular time points in a highly transient system. Specifically, model outputs were compared against isometric muscle stress and intramuscular pressure data under maximum contraction only. For passive stretch data, steady-state pressure comparisons were made. While the agreement in Chapter 6 between model and experiment suggests an effective computational approach, there is concern in using this model to study dynamic muscle conditions, which are critical to *in vivo* muscle function [10]. The force-pressure relationship under sub-maximal conditions would be of interest as normal gait and daily function typically do not occur at maximum contraction [10]. Validation of model behavior under various contractile levels would greatly strengthen the applicability of this model.
Thus, there are three goals of the work presented here: 1) investigate variability in model fluid pressure and evaluate the efficacy of the previously utilized constitutive model in predicting intramuscular pressure behavior for 2) different muscle architecture (in this case a bipennate structure) and 3) variations in contractile level.

7.2 Methods

7.2.1 Experimental Data

Previous experimental analysis of isometric contractile behavior of the human tibialis anterior was completed [11]. Eight (n=8) healthy young adults were recruited for the study, which involved simultaneous measurement of dorsiflexion force and intramuscular pressure. For each subject, the ankle was placed at a neutral position (90° angle with the leg) with the knee between 45-60° of flexion and dorsiflexion force was measured with a force transducer. Intramuscular pressure was measured with a pressure microsensor [12] inserted longitudinally (along with the muscle fibers) into the muscle midbelly using a 22 gauge catheter. Each subject contracted to 50% maximum voluntary contraction (MVC) at three contraction rates: 5% per second, 10% per second, and 15% per second. Each contraction rate test was repeated for a total of fifteen trials per rate per subject, or 45 trials in total per subject. Dorsiflexion force was normalized for each run and intramuscular pressure was zeroed to produce IMP-%MVC data. To simplify and combine the results, IMP-%MVC data points were identified in intervals of 2.5% MVC from 0-50%. Intramuscular pressure was averaged over a 0.1 seconds at each interval to reduce noise.

7.2.2 Constitutive Model

The constitutive approach utilized in this study was previously developed and validated against experimental data of the New Zealand White Rabbit tibialis anterior (TA). The details of this material model can be found in [13] for detailed explanation of passive behavior and in Chapter 6 for detailed explanation of active behavior. In short, the passive constitutive approach utilized hyper-visco-poroelastic theories to characterize the complex passive function of the solid constituents of skeletal muscle. The tensile nonlinearity and anisotropy were modeled using an

isotropic hyperelastic Mooney-Rivlin strain energy density function [14] reinforced with exponential tension-only fibers [15]. This formulation allows the utilized approach to characterize the unique transversely isotropic behavior of skeletal muscle, where the longitudinal or fiber direction has a highly nonlinear tensile response, while the transverse or cross fiber direction has a more linear and stiffer response [16]. To model the time dependent relaxation of skeletal muscle in tension, a viscoelastic Prony series was employed [17] and fluid content was modeled with poroelasticity [18].

For active muscle, a formulation which dictates active stress as a function of time was incorporated, allowing for the ramp behavior of maximally contracting muscle to be appropriately simulated [10]. An inhomogeneous approach was developed which specified two different muscle constituents: passive only muscle and muscle which generated contractile stress and supported passive deformation. Due to the complexity of the structure-function relationship of passive muscle, including the fact that muscle passive behavior is a manifestation of both ECM and fiber stiffness [19,20], both constituents were given identical passive properties, with the exclusion of poroelasticity for the active-passive constituent. As seen in Chapter 6, this approach yielded good agreement between IMP and model pressure for maximally stimulated isometric contraction at various muscle lengths, particularly for the physiological operating range.

7.2.3 Finite Element Geometry

An idealized finite element geometry of the human tibialis anterior (TA) was developed (Figure 7-1). Based on literature data [21], the total muscle length was 260 mm, pennation angle was

9.98°, and muscle fibers were 68.5 mm. The bipennate structure of the human TA requires an internal aponeurosis or tendon in addition to external aponeuroses (Figure 7-1A). Similar to previous finite element modeling of skeletal muscle (Chapter 6), an inhomogeneous geometry was employed in which 20% of the total muscle volume was defined as contractile. Due to the structure of this inhomogeneous approach, the hexahedral mesh lines must follow the muscle fiber orientations. This makes modeling the full geometry of the human tibialis anterior a challenge, which is why this idealized approach was implemented. The model represents a slice of the human TA 1mm thick, midway between the lateral and medial sides of the tissue.

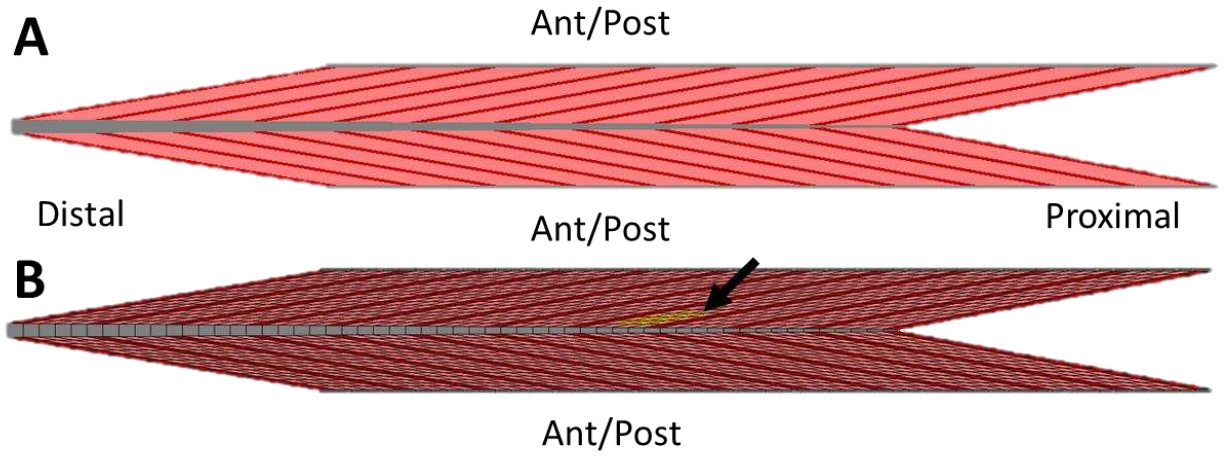

Figure 7-1. Idealized geometry of human tibialis anterior finite element model. A) Model without mesh lines to highlight various constituents, including active-passive (dark red), passive only (light red), and aponeurosis (gray). B) The same geometry with mesh lines and elements highlighted in yellow (black arrow) which were utilized for fluid pressure output.

To simulate isometric activation of the human TA at neutral flexion (the ankle joint at 90 degrees), the distal end of the muscle was displaced towards the proximal end and pinned prior to contraction, enacting muscle shortening. This is because the human TA is slack at neutral ankle flexion and does not support significant passive loads until nearly ten degrees of dorsiflexion [22]. After a 300 second relaxation phase [17,23], 50% maximum voluntary contraction (MVC) was applied through a ramp of active stress generation within the model with

a linear slope. This contraction was applied at three rates: 5% MVC per second, 10% MVC per second, and 15% MVC per second to match experimental trials [11]. With both the proximal and distal ends of the tissue pinned, the specific tension of the model was determined by summing the reaction force as the distal nodes and dividing by the physiological cross sectional area of 33.35 mm^2. Intramuscular pressure was interpreted as the mean fluid pressure of six elements within the model which were chosen to due to experimental location of pressure microsensors (Figure 7-1B) [11]. Model pressure was zeroed at the beginning of contraction, which occurred after stress relaxation as a result of passive deformation.

7.2.4 Variations in Boundary Conditions and Model Parameters

To study the effect of muscle length as well as contractile force on model fluid pressure, variations in pre-contraction displacement and specific tension were applied. For the pre-contraction displacement, previous experimental work has shown that the human TA is slack when the ankle is neutral, and that the difference in muscle length between this neutral position and ten degrees of plantarflexion when passive tension is recruited is roughly 3.5% [22,24]. However, the previously developed and validated constitutive model employs a wide toe region [13], thus there is some concern over the proper pre-contraction displacement, as the low stiffness within this toe region may be difficult to observe experimentally *in vivo* versus *in vitro*. To investigate the role of pre-contraction shortening on the model fluid pressure, four different displacement lengths were applied to the distal end of the tissue resulting in muscle shortening, 4.5 mm, 6 mm, 7.5 mm, and 9 mm (experimentally calculated value). These will be referred to as “Model 1” (4.5 mm), “Model 2” (6 mm), “Model 3” (7.5 mm), and “Model 4” (9 mm).

Specific tension of human muscle *in vivo* cannot be directly measured, as experimental analysis requires measurement of torque and back calculations using anatomical and muscle structural measurements [25]. Fukunaga et al. found that the human TA generates roughly 85 kPa at maximum voluntary contraction [24], while Maganaris et al. others determined a value of 155 kPa [26]. Thus, for 50% maximum voluntary contraction, two specific tension values were utilized in this study: 42.5 kPa and 77.5 kPa.

7.2.5 Statistics

Similar to Chapter 6, the root mean square error (RMSE, Equation 1, where y^e are experimental data and y^m are model data) and normalized root mean square error (NRMSE, Equation 2) were utilized to evaluate model fit to experimental data. Model fluid pressure output was compared against experimental intramuscular pressure data at 2.5% MVC increments up to 50% MVC. Total NRMSE for each model to all three contraction rates was calculated as the square root of the sum of the squared NRMSE values for each contraction rate.

$$RMSE = \sqrt{\frac{\sum_{i=1}^{15}\left(y_i^e - y_i^m\right)^2}{15}} \quad (1)$$

$$NRMSE = \frac{RMSE}{max(y^e) - min(y^e)} \quad (2)$$

7.3 Results

Model fluid pressure showed a nonlinear increase as a function of contraction level (Figure 7-2) similar to experimental data. Statistical agreement between models and experimental data ranged from less than 7% NRMSE to 95% NRMSE for individual pressure-contraction curves (Table 7-1). For Model 3 with an applied specific tension of 42.5 kPa, the best overall fit to experimental data was observed at 23% NRMSE (Table 7-1). Both muscle length (Model #) and specific

tension affected model fluid pressure visually (Figure 7-2) as well as statistically in terms of agreement to experimental data (Table 7-1). However, the differences in fluid pressure were larger because of the variations in boundary conditions versus variations in specific tension (Figure 7-2).

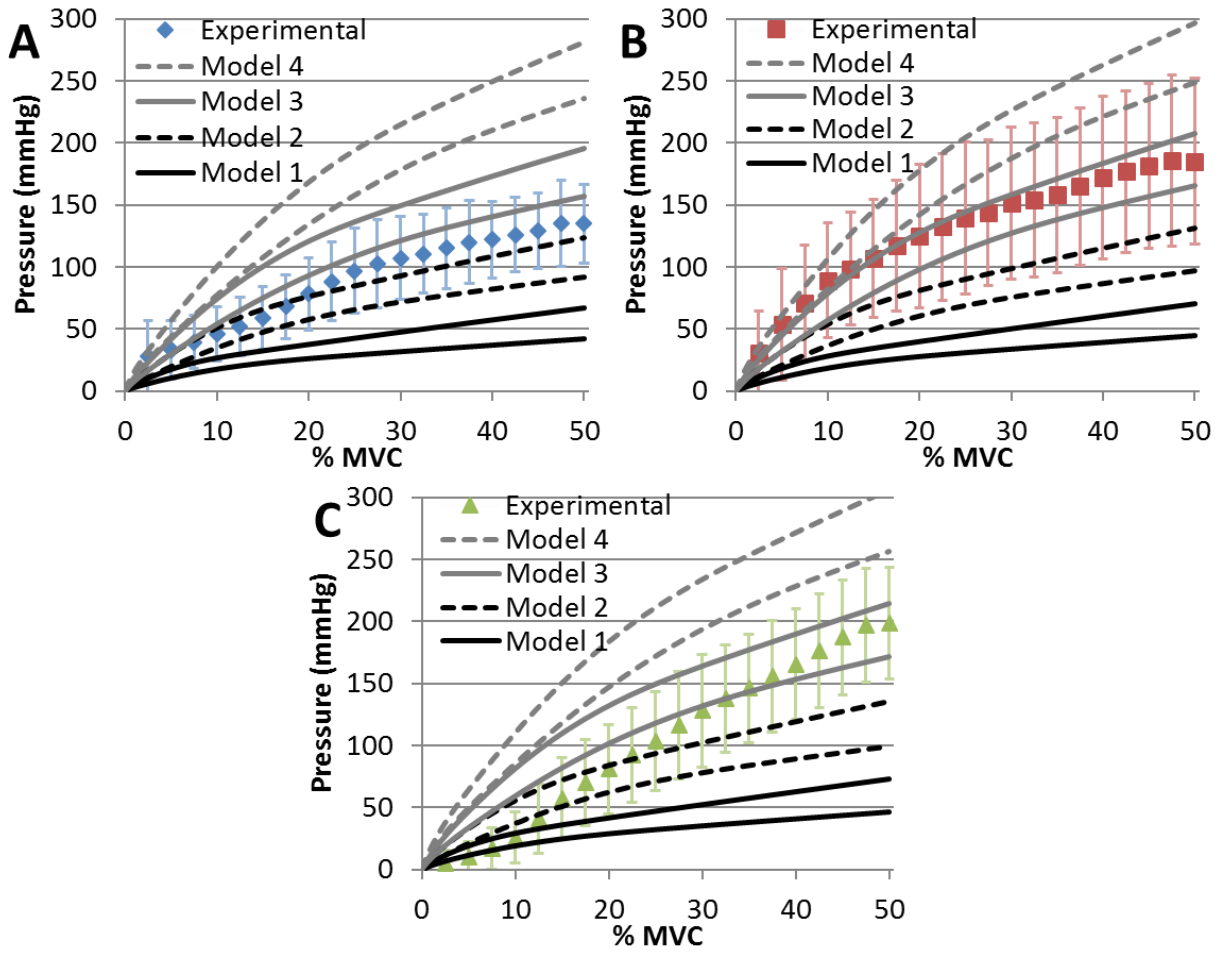

Figure 7-2. Comparison between experimental data (standard error bars) and modeling outputs. All model curves show specific tension values for both 77.5 kPa (top curves) and 42.5 kPa (bottom curves). A) Contraction rate of 5% per second. B) Contraction rate of 10% per second. C) Contraction rate of 15% per second.

Table 7-1. Statistical analysis of agreement between model outputs and experimental data. Fluid pressure behavior was dictated by both pre-contraction length as well as specific tension. Model 3 with a specific tension of 42.5 kPa was found to have the overall strongest agreement to experiment at NRMSE of 23%.

Model #	Specific Tension (kPa)	5%/s		10%/s		15%/s		Total NRMSE
		RMSE (kPa)	NRMSE	RMSE (kPa)	NRMSE	RMSE (kPa)	NRMSE	
Model 1	**42.5**	66	62%	107	69%	91	47%	104%
	77.5	51	48%	91	59%	75	39%	85%
Model 2	**42.5**	31	29%	70	45%	55	28%	60%
	77.5	11	10%	46	30%	35	18%	36%
Model 3	**42.5**	15	14%	24	16%	21	11%	23%
	77.5	43	40%	10	6.7%	39	20%	45%
Model 4	**42.5**	67	63%	36	23%	60	31%	74%
	77.5	101	95%	70	45%	97	50%	116%

The fluid pressure distribution within the model shows highly variable pressure values at the proximal and distal ends, with a more consistent distribution within the muscle midbelly (Figure 7-3A). This was confirmed both by plotting fluid pressure as a function of distal to proximal location (Figure 7-3B) and by evaluating the statistical distribution of fluid pressure in four regions (Table 7-2). Specifically, when the pressure-location data from the model in Figure 7-3B are divided into four equal sized element groups (distal, middle near distal, middle near proximal, and proximal), the lowest standard deviations (4.5 and 7.5 mmHg for the superficial and deep data, respectively) and ranges (similarly 13 and 26 mmHg) are observed in the middle-distal region and the highest (21-71 mmHg for standard deviation and 67-187 mmHg for range) are observed in the distal and proximal regions.

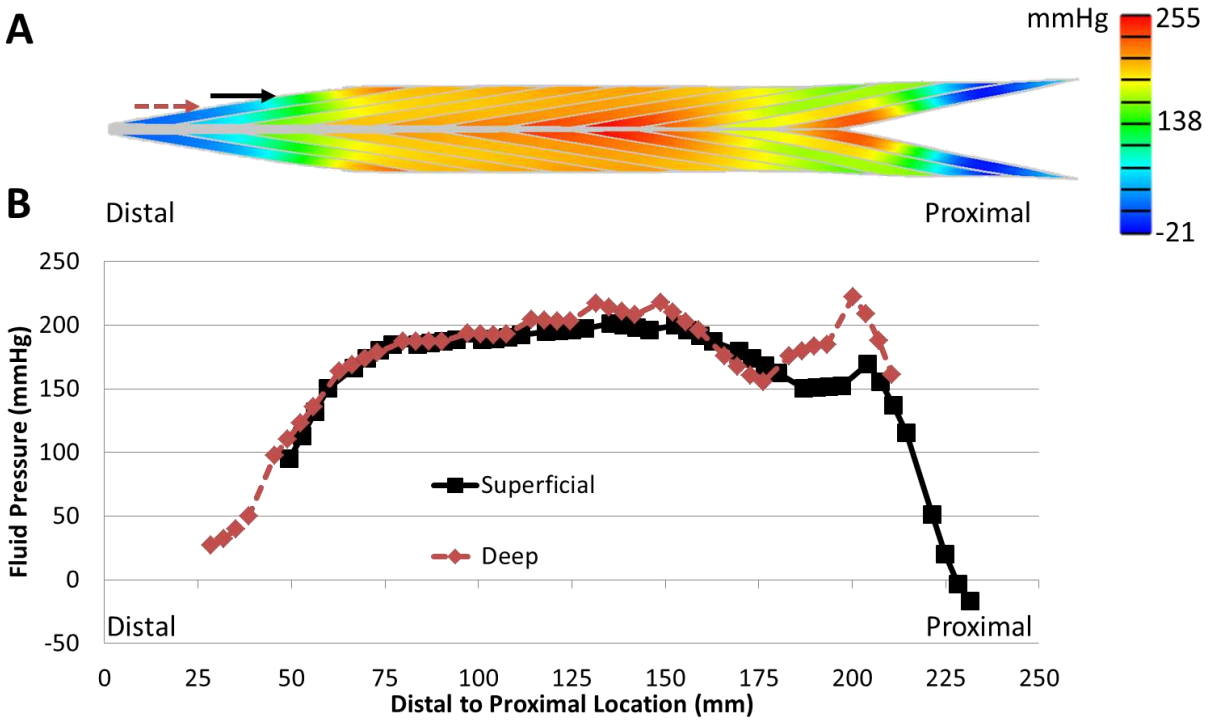

Figure 7-3. Fluid pressure distribution at 50% MVC for Model 3 after contracting at a rate of 10% per second. Figure shown for muscle model contracting at a specific tension value of 77.5 kPa (smallest NRMSE at 6.7% from Table 7-1). A) Pressure color map within finite element model. B) Plot of model pressures as a function of distal to proximal location. The two curves are shown for element rows located at the corresponding arrows from A. The model in A is aligned with the x-axis of the plot in B for comparison. The proximal (left) and distal (right) ends of the muscle showed highest spatial variability in fluid pressure.

Table 7-2. Statistical analysis of regional fluid pressure variation within the model. Data from Figure 7-3B grouped into four sets by distal to proximal location (distal, middle near distal, middle near distal, and proximal). The distal-proximal region exhibited the lowest standard deviations and ranges, while the distal and proximal regions exhibited the highest.

Region	Superficial Pressure (mmHg)			Deep Pressure (mmHg)		
	Average	StDev	Range	Average	StDev	Range
Distal	159	33	92	102	57	147
Middle-Distal	194	4.5	13	192	7.5	26
Middle-Proximal	182	17	49	205	12	41
Proximal	99	71	187	181	21	67

7.4 Discussion

The contractile stress values utilized in this study are below the 50% of the maximum voluntary isometric specific tension of skeletal muscle (~100 kPa) [10]. This is likely due to the fact that the human TA is on the ascending limb of the isometric force-length curve with the ankle in a neutral position [24]. While specific tension values played a role in the pressurization of fluid within the model (Figure 7-2 and Table 7-1), muscle length had a larger effect on model fluid pressure as presented here (Figure 7-2). However, this is certainly dependent on the exact boundary conditions and specific tension values utilized in this study. The variations in pre-contraction muscle length were identified by utilizing physiology studies to estimate approximate muscle length with the ankle at a neutral position [22,24]. Yet the long toe-region exhibited by the utilized constitutive model [13] suggests *in vivo* detections of muscle stiffness may be difficult at low strain levels and thus passive tension could occur closer to the neutral position than reported. Thus, it is not surprising that Model 3 exhibited the strongest correlation to experimental data (total NRMSE of 23%, Table 7-1), as it requires some muscle shortening, but not the full 9mm as calculated from literature.

As muscle length decreased (going from Model 1 to Model 4), pressure values increased (Figure 7-2). This agrees with findings from Chapter 6, which shows model pressures on the ascending limb were higher than at optimal length, which were higher than those on the descending curve. While it remains to be seen exactly how muscle length and intramuscular pressure are related in human *in vivo* studies, this work suggests that muscle length contributes to variability in intramuscular pressure. This could partially explain why experimentally measured intramuscular

pressure values are fairly consistent for the same muscle and patient, but less so for different muscles or patients where architecture and/or anatomy are variable [7,11].

Intramuscular pressure values from this study (~100-250 mmHg) are comparable to or higher than those from the Chapter 6 study (~25-150 mmHg), despite the fact that this work was conducted at 50% MVC while Chapter 6 was under 100% MVC. These differences in fluid pressure could be due to differences in muscle architecture, as the utilized constitutive models are the same and both studies simulated contraction at short muscle lengths. Specifically, the human TA is bipennate with a pennation angle of roughly 20° while the rabbit TA is unipennate and has a very low pennation angle of only 3° [8,21]. In fact, despite the massive differences in size, the fiber length of the human TA is less than twice that of the rabbit TA (68 mm vs 38 mm) [8,21]. Thus, the agreement between model and experimental data exhibited for both the rabbit TA in Chapter 6 and here for the human TA provides strong evidence that the utilized constitutive approach is a robust model for skeletal muscle at the tissue level.

This work also presents the first finite element simulation of both muscle force and intramuscular pressure for human muscle contracting across a range of voluntary levels, specifically from 0% to 50% MVC. Previous work from Chapter 6 compared model and experimental pressures at maximal stimulation only, similar to early finite element work of muscle force and IMP [27]. The nonlinear shape of model pressure-contraction outputs is similar to that of the experimentally gathered pressure-contraction data, particularly for Model 3 compared to 10% per second contraction rate data (Figure 7-2). This approach is also unique in the fact that the passive constitutive model incorporates viscoelastic and poroelastic theories, which means time dependent variations in fluid pressure are the result of solid constituent relaxation, fluid flow,

and contraction level. Thus, the agreement between model and experiment further supports the use of this constitutive approach as a robust method to simulate the behavior of skeletal muscle.

Regional variation of fluid pressurization within the model showed the least variable pressure readings in the muscle midbelly, but large spatial variations at the proximal and distal ends by inspection of both a color map and plotted pressure-location data (Figure 7-3). Statistical analysis of variability within the four model regions (distal to proximal) supported these findings (Table 7-2). From a modeling perspective, this suggests IMP readings from pressure microsensors would be most consistent if placed in the muscle midbelly, away from large IMP gradients. This also suggests variations in experimentally measured IMP could be the result of improper sensor insertion, as small changes in insertion location could manifest in large changes in pressure readings in the proximal and distal regions. However, this must be either confirmed or rejected experimentally, as clinical recommendations cannot be made in confidence before regional validation within the model is completed. Model behavior could also be validated against three dimensional strain calculations utilizing magnetic resonance imaging [28] to improve confidence in interpreting spatial results. Thus, this work proposes the use of Figure 7-3 and Table 7-2 data in implementing further modeling studies or experimental analyses of intramuscular pressure to either confirm or reject the hypothesis that the muscle midbelly is the ideal location for sensor insertion.

While this work presented novel insight into skeletal muscle function from a modeling perspective and strengthened the case for the use of a hyper-visco-poroelastic approach to modeling skeletal muscle, there are certainly some potential weaknesses along with future work

to be completed. First, the utilized finite element geometry from this study represents only an idealized version of the human tibialis anterior. A full geometry would require either alterations to the inhomogeneous approach for muscle activation or highly complex meshing, as the hexahedral mesh lines must follow the orientation of muscle fibers. While this would provide further insight into global IMP behavior, the *in vivo* environment of the human TA would require careful assumptions regarding boundary conditions. This is particularly evident given the current study, which highlights how boundary conditions can affect model fluid pressure. The effects of muscle weakness and disease such as fibrosis [29] could also be studied to evaluate how fluid pressure changes with impaired function. Finally, the constitutive approach for muscle activation should be improved to include the dependence of muscle force on velocity.

7.5 Conclusions

This work presented the first finite element model of human skeletal muscle which modeled various contraction levels and simulated both muscle force and intramuscular pressure. Simulating a bipennate muscle under variable contractile conditions provides further confidence in utilizing a constitutive model developed for a unipennate geometry under maximum voluntary contraction only. This model provides evidence that muscle length, specific tension, sensor insertion location, and architecture may account for variability of intramuscular pressure readings *in vivo*. Finally, while the model suggests that the midbelly of the tissue is ideal for sensor location, this must be either confirmed or rejected using further modeling or experimental analysis. Future work to study impaired muscle and more advanced contractile conditions would greatly increase the clinical application of this work.

REFERENCES

[1] Davis, J., Kaufman, K. R., and Lieber, R. L., 2003, "Correlation between active and passive isometric force and intramuscular pressure in the isolated rabbit tibialis anterior muscle," J. Biomech., **36**(4), pp. 505–512.

[2] Ward, S. R., Davis, J., Kaufman, K. R., and Lieber, R. L., 2007, "Relationship between muscle stress and intramuscular pressure during dynamic muscle contractions," Muscle and Nerve, **36**(3), pp. 313–319.

[3] Winters, T. M., Sepulveda, G. S., Cottler, P. S., Kaufman, K. R., Lieber, R. L., and Ward, S. R., 2009, "Correlation between isometric force and intramuscular pressure in rabbit tibialis anterior muscle with an intact anterior compartment," Muscle and Nerve, **40**(1), pp. 79–85.

[4] Sejersted, O. M., Hargens, A. R., Kardel, K. R., Blom, P., Jensen, O., and Hermansen, L., 1984, "Intramuscular fluid pressure during isometric contraction of human skeletal muscle.," J. Appl. Physiol., **56**(2), pp. 287–95.

[5] Järvholm, U., Palmerud, G., Karlsson, D., Herberts, P., and Kadefors, R., 1991, "Intramuscular pressure and electromyography in four shoulder muscles.," J. Orthop. Res., **9**(4), pp. 609–19.

[6] Nakhostine, M., Styf, J. R., van Leuven, S., Hargens, A. R., and Gershuni, D. H., 1993, "Intramuscular pressure varies with depth. The tibialis anterior muscle studied in 12 volunteers.," Acta Orthop. Scand., **64**(3), pp. 377–81.

[7] Sejersted, O. M., and Hargens, A. R., 1995, "Intramuscular pressures for monitoring different tasks and muscle conditions.," Adv. Exp. Med. Biol., **384**, pp. 339–350.

[8] Lieber, R. L., and Blevins, F. T., 1989, "Skeletal muscle architecture of the rabbit hindlimb: functional implications of muscle design.," J. Morphol., **199**(1), pp. 93–101.

[9] Wolf, S. L., and Kim, J. H., 1997, "Morphological Analysis of the Human Tibialis Anterior and Medial Gastrocnemius Muscles," Cells Tissues Organs, **158**(4), pp. 287–295.

[10] Lieber, R. L., 2010, Skeletal Muscle Structure, Function, and Plasticity, Lippincott Williams and Wilkins, Philadelphia, PA.

[11] Go, S. A., 2016, "Investigation of motor control through simultaneous measurement of force, electromyography, and intramuscular pressure," Mayo Clinic.

[12] Go, S. A., Jensen, E. R., O'Connor, S. M., Evertz, L. Q., Morrow, D. A., Ward, S. R., Lieber, R. L., and Kaufman, K. R., 2016, "Design Considerations of a Fiber Optic Pressure Sensor Protective Housing for Intramuscular Pressure Measurements," Ann. Biomed. Eng.

[13] Wheatley, B. B., Odegard, G. M., Kaufman, K. R., and Haut Donahue, T. L., 2016, "A validated model of passive skeletal muscle to predict force and intramuscular pressure," Biomech. Model. Mechanobiol., pp. 1–12.

[14] Johansson, T., Meier, P., and Blickhan, R., 2000, "A finite-element model for the mechanical analysis of skeletal muscles.," J. Theor. Biol., **206**(1), pp. 131–49.

[15] Ateshian, G. A., Rajan, V., Chahine, N. O., Canal, C. E., and Hung, C. T., 2009, "Modeling the matrix of articular cartilage using a continuous fiber angular distribution

predicts many observed phenomena.," J. Biomech. Eng., **131**(6), p. 61003.
[16] Wheatley, B. B., Odegard, G. M., Kaufman, K. R., and Donahue, T. L. H., 2016, "How does tissue preparation affect skeletal muscle transverse isotropy?," J. Biomech., **49**(13), pp. 3056–3060.
[17] Wheatley, B. B., Morrow, D. A., Odegard, G. M., Kaufman, K. R., and Haut Donahue, T. L., 2016, "Skeletal muscle tensile strain dependence: Hyperviscoelastic nonlinearity.," J. Mech. Behav. Biomed. Mater., **53**, pp. 445–54.
[18] Wheatley, B. B., Odegard, G. M., Kaufman, K. R., and Haut Donahue, T. L., 2016, "A case for poroelasticity in skeletal muscle finite element analysis: experiment and modeling.," Comput. Methods Biomech. Biomed. Engin., pp. 1–4.
[19] Meyer, G. A., and Lieber, R. L., 2011, "Elucidation of extracellular matrix mechanics from muscle fibers and fiber bundles," J. Biomech., **44**(4), pp. 771–773.
[20] Meyer, G. A., McCulloch, A. D., and Lieber, R. L., 2011, "A Nonlinear Model of Passive Muscle Viscosity," J. Biomech. Eng., **133**(9), p. 91007.
[21] Ward, S. R., Eng, C. M., Smallwood, L. H., and Lieber, R. L., 2009, "Are Current Measurements of Lower Extremity Muscle Architecture Accurate?," Clin. Orthop. Relat. Res., **467**(4), pp. 1074–1082.
[22] Koo, T. K., Guo, J.-Y., Cohen, J. H., and Parker, K. J., 2014, "Quantifying the passive stretching response of human tibialis anterior muscle using shear wave elastography," Clin. Biomech., **29**(1), pp. 33–39.
[23] Abraham, A. C., Kaufman, K. R., and Haut Donahue, T. L., 2012, "Phenomenological consequences of sectioning and bathing on passive muscle mechanics of the New Zealand white rabbit tibialis anterior," J. Mech. Behav. Biomed. Mater., **17**, pp. 290–295.
[24] Fukunaga, T., Roy, R. R., Shellock, F. G., Hodgson, J. A., and Edgerton, V. R., 1996, "Specific tension of human plantar flexors and dorsiflexors.," J. Appl. Physiol., **80**(1), pp. 158–65.
[25] O'Brien, T. D., Reeves, N. D., Baltzopoulos, V., Jones, D. A., and Maganaris, C. N., 2010, "In vivo measurements of muscle specific tension in adults and children.," Exp. Physiol., **95**(1), pp. 202–10.
[26] Maganaris, C. N., Baltzopoulos, V., Ball, D., and Sargeant, A. J., 2001, "In vivo specific tension of human skeletal muscle.," J. Appl. Physiol., **90**(3), pp. 865–72.
[27] Jenkyn, T., Koopman, B., Huijing, P. a, Lieber, R. L., and Kaufman, K. R., 2002, "Finite element model of intramuscular pressure during isometric contraction of skeletal muscle.," Phys. Med. Biol., **47**, pp. 4043–4061.
[28] Jensen, E. R., Morrow, D. A., Felmlee, J. P., Murthy, N. S., and Kaufman, K. R., 2016, "Characterization of Three Dimensional Volumetric Strain Distribution during Passive Tension of the Human Tibialis Anterior using Cine Phase Contrast MRI," J. Biomech.
[29] Sato, E. J., Killian, M. L., Choi, A. J., Lin, E., Esparza, M. C., Galatz, L. M., Thomopoulos, S., and Ward, S. R., 2014, "Skeletal muscle fibrosis and stiffness increase after rotator cuff tendon injury and neuromuscular compromise in a rat model.," J. Orthop. Res., **32**(9), pp. 1111–6.

CHAPTER 7:

CONCLUSIONS AND FUTURE WORK

In summary, this work presents the development and implementation of a finite element model of skeletal muscle to study intramuscular pressure. Constitutive model development was based on three experimental analyses of skeletal muscle which investigated 1) the viscoelastic response of muscle in tension, 2) the anisotropic and hyperelastic response of muscle in tension, and 3) the hydraulic permeability of the tissue. These data were utilized to create and implement a novel transversely isotropic, hyper-visco-poroelastic constitutive approach to model the passive behavior of skeletal muscle. Muscle activation was incorporated through an inhomogeneous approach. Model validation was completed against experimental data of muscle stress and intramuscular pressure, and simulations of both rabbit muscle and human muscle were completed.

Experimental studies identified critical phenomena at the tissue level for the development of a robust finite element model. The tensile viscoelastic behavior of skeletal muscle was studied to determine if muscle exhibited linear or nonlinear viscoelasticity. While statistical analysis suggested strain level dependence of stress relaxation, only marginal increases in modeling accuracy were observed in a fully nonlinear viscoelastic model versus a quasilinear viscoelastic model. Thus, the use of quasilinear viscoelasticity was chosen for this work. Future studies incorporating fully nonlinear viscoelasticity into a finite element model of skeletal muscle would shed light on how viscoelastic assumptions affect whole muscle behavior from a computational

standpoint. Transversely isotropic tensile testing of skeletal muscle under fresh and non-fresh (subject to a freeze-thaw cycle) conditions confirmed previous findings that the transverse orientation exhibited stiffer and more linear behavior than the longitudinal orientation, while conflicts in literature were likely the result of post-mortem stiffening. All future experimental studies of skeletal muscle should be completed under fresh conditions, before the effects of rigor mortis (~4-8 hours). Finally, muscle hydraulic permeability was directly measured and muscle compression was simulated with various strain dependent and anisotropic assumptions. While tissue relaxation in tension is generally attributed to inherent viscoelasticity of solid constituents, poroelasticity may play a role in stress relaxation under compressive conditions. Further work to identify how well poroelastic theory can explain stress relaxation of muscle in compression may result in modeling approaches with greater physiological accuracy.

The developed constitutive model was validated using a finite element approach for passive stretch, activate contraction, and in two muscle geometries. This robust approach supports the use of this model for variations in physiological architecture and both passive and active conditions. The model suggested that in addition to activation level, muscle length and architecture contribute to variability of intramuscular pressure. Additionally, the use of longitudinal sensor insertion yielded experimental data which more closely agreed to model output versus transverse insertion. Spatial variability was observed from a modeling perspective but must be confirmed experimentally before strong clinical recommendations about sensor insertion location can be made.

While this work has presented the development and implementation of a model of skeletal muscle to study the behavior of intramuscular pressure (IMP), future work should be completed to strengthen the use of IMP as a clinical measurement. Firstly, finite element analysis of human *in vivo* muscle geometry should be completed for greater clinical impact. While accurate whole muscle geometry was simulated for the rabbit tibialis anterior, the creation of a human mesh entails some difficulty due to architecture and orientation. The approach presented here should also be validated spatially using data gathered through experimental analysis. This could include both intramuscular pressure measurements at various spatial regions throughout the tissue as well as imaging modalities such as magnetic resonance imaging to evaluate regional strain of *in vivo* muscle.

Additionally, further developments of muscle activation from a constitutive standpoint would greatly expand the impact of this model. Specifically, this includes isotonic contractions, where muscle is actively shortening or lengthening, as is common in gait and locomotion. Modeling clinical conditions such as muscle weakness, increases in stiffness as a result of fibrosis, or decreases in muscle mass could also shed light onto the role of intramuscular pressure in impaired muscle. While this work has provided novel insight into muscle function through experimental and computational analyses, there remains an opportunity to build upon this work and make a greater clinical impact.